Dissertation

submitted to the
Combined Faculties for the Natural Sciences and for Mathematics
of the Ruperto-Carola University of Heidelberg, Germany
for the degree of
Doctor of Natural Sciences

Put forward by
Dipl.-Phys. Jérôme Soiné
born in Karlsruhe
Oral examination: 07.05.2014

Reconstruction and Simulation of Cellular Traction Forces

Referees: Prof. Dr. Ulrich Schwarz
Prof. Dr. Heinz Horner

Abstract

Biological cells are able to sense the stiffness, geometry and topography of their environment and sensitively respond to it. For this purpose, they actively apply contractile forces to the extracellular space, which can be determined by traction force microscopy. Thereby cells are cultured on elastically deformable substrates and cellular traction patterns are quantitatively reconstructed from measured substrate deformations, by solving the inverse elastic problem. In this thesis we investigate the influence of environmental topography to cellular force generation and the distribution of intracellular tension. For this purpose, we reconstruct traction forces on wavy elastic substrates, using a novel technique based on finite element methods. In order to relate forces to single cell-matrix contacts and different structures of the cytoskeleton, we then introduce another novel variant of traction force microscopy, which introduces cell contraction modeling into the process of cellular traction reconstruction. This approach is robust against experimental noise and does not need regularisation. We apply this method to experimental data to demonstrate that different types of actin fibers in the cell statistically show different contractilities. We complete our investigation by simulation studies considering cell colonies and single cells as thermoelastically contracting continuum coupled to an elastic substrate. In particular we examined the effect of geometry on cellular behavior in collective cell migration and tissue invasion during tumor metastasis.

Zusammenfassung

Biologische Zellen sind in der Lage, Steifigkeit, Geometrie und Topographie ihrer Umwelt wahrzunehmen und darauf sehr sensibel zu reagieren. Zu diesem Zweck üben sie aktiv Kräfte auf die Umgebung aus, die mit der sogenannten Zellkraftmikroskopie bestimmt werden können. Dabei werden Zellen im Experiment auf elastisch verformbaren Substraten kultiviert und anschließend aus der gemessenen Substratverformung, durch Lösen des inversen elastischen Problems, quantitative Zellkraftverteilungen bestimmt. Die vorliegende Arbeit beschäftigt sich mit dem Einfluss der Substrattopographie auf die Zellkraftentwicklung und die intrazelluläre Verteilung von mechanischer Spannung. Zu diesem Zweck werden Zellkräfte auf nicht-planaren Substraten mit einer neuartigen Methode bestimmt, die auf Finite Elemente Methoden aufbaut. Um Zell-Substrat Kräfte mit bestimmten Komponenten des Zytoskeletts in Verbindung zu bringen, haben wir eine weitere Variante der Zellkraftmikroskopie entwickelt, die Zellkontraktionsmodelle in die Kraftrekonstruktion einbezieht. Dieser Ansatz ist sehr robust gegenüber experimentellen Unsicherheiten und benötigt keine Regularisierung. Wir konnten mit dieser Methode unter anderem zeigen, dass unterschiedliche Fasertypen des Aktin-Zytoskeletts statistisch gesehen verschiedene Kontraktionskräfte aufweisen. Schließlich beschreiben wir Simulationsstudien, bei denen wir Zellkolonien und einzelne Zellen als thermoelasisch kontrahierendes Kontinuum beschreiben. Hier haben wir uns im speziellen mit der geometrieabhängigen Ausbildung von "Leader"-Zellen und dem Eindringen von Krebszellen in Geweben während des Prozesses der Metastasierung beschäftigt.

Contents

1

Introduction

1.1 Role of Forces

Cellular forces are indispensable for every multicellular organism. Their impact ranges from the length scale of individual cells up to the scale of an entire organism. In our daily life we experience cell generated forces all the time, for example when we lift a weight. Muscle fibers, which are assembled from muscle cells, contract in a collective fashion in order to shorten the entire muscle (assembly illustrated in fig. 1.1). Similar to this the heart contracts periodically due to synchronized force generation of heart muscle cells, in order to drive vital blood flow. Cellular forces are also very important in embryonic development. They influence cell growth and tissue flow, which give rise to tissue compartmentalization, followed by formation of individual organs. In homeostatic tissue, cell generated forces are responsible for maintaining a constant level of tension, which contributes to the mechanical integrity of the tissue. Finally, on the single cell level, self-generated and environmental forces feed back into cellular biochemistry. This is called mechanotransduction. Thereby, cells sense and respond to physical properties of their environment, which influences cell fate, proliferation, and differentiation. Again, on a larger scale microscopic cellular response eventually allows tissues, organs and entire organisms to actively adapt to changing demands like e.g. muscle enforcement by training. In the following we introduce the biological structures, which are involved in force generation and transmission on a single cell level.

1.2 Cellular Mechanics & Extracellular Matrix

Cellular and environmental mechanics are tightly connected to each other, since cells are able to sense and organize extracelluar space. The ability of the cell to generate

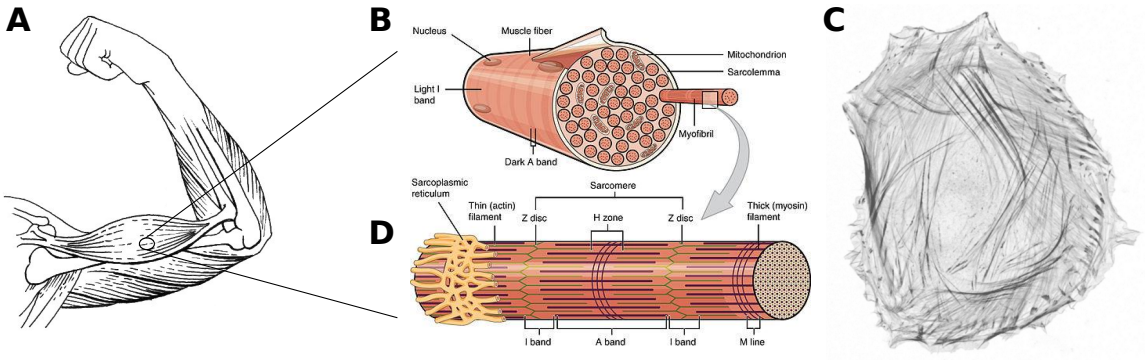

Figure 1.1: From muscles to single cells. Illustration of force generation in muscle tissue. The muscle (A) is assembled from highly ordered muscle fibers (B). They contain muscle cells (C), which consists in most parts of contractile myofibriles (D). These are again build of a serial arrangement of ordered protein assemblies, so-called sarcomers. As they are build from cytoskeletal actin filaments and smooth muscle myosin II motor proteins, they generate forces on the microscopic scale. Images taken from (1).

a certain level of tension is indispensable for this task. Diseases like for example arteriosclerosis and cancer are directly related to deficiency of tensional homeostasis in adult tissue (2, 3, 4). In the following, a brief biological introduction is given about the composition and structure of the extracellular matrix (ECM), which fills the space between cells in the tissue, and the cytoskeleton (CSK), which gives the cell its mechanical properties and provides a force generating machinery. Further, we will introduce focal adhesions (FA), which are the most important cell-matrix contacts regarding force transmission to the ECM.

Extracellular Matrix

Cells in tissue are surrounded by a complex network of macromolecules, called the extracellular matrix (ECM), see fig. 1.2 (5). It fills the largest part of the tissue volume and gives rise to its mechanical stability. In addition, it serves as a medium for cells. These adhere to specific molecules in the ECM and can also migrate through it. The ECM also provides the basis for cell-cell communication, either by diffusion of signaling molecules or by transmission of external and cell generated mechanical forces (6). Although the molecular composition of the ECM varies over different tissue types, two main classes of macromolecules dominate: large polysaccharide-protein complexes and fibrous proteins. The former are so-called proteoglycans, which are polysaccharide chains that can covalently bind to ECM molecules like collagen or hyoluronic acids. They are highly hydrated, which means that they bind high amount of water eventu-

ally giving the ECM its resistance against compressional forces. The class of fibrous proteins of the ECM consists mainly of collagen, fibronectin, elastin, and laminin (7). The assembling of the ECM takes place during tissue development. Nevertheless, due to natural degradation processes or tissue injuries, specialized cells like fibroblasts permanently guard, remodel and organize tissue homeostasis (5).

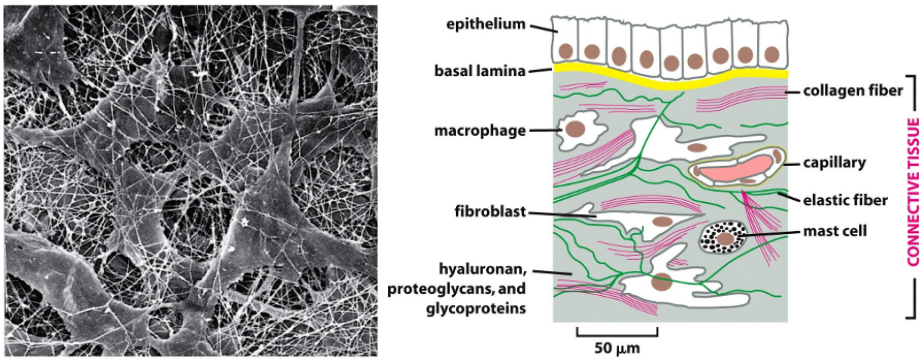

Figure 1.2: Extracellular Matrix. Scanning electron tissue micrograph from cornea of a rat (left). Cells are embedded in a matrix composed of fibrillar macromolecules, illustration as tissue cross-section (connective tissue) (right). Figures taken from (7).

Variable microscopic composition of the ECM allows organisms to develop tissues of different structure and mechanical properties. The microscopical structure can vary from strongly ordered like in the basal lamina with highly aligned collagen fibers, to randomly distributed collagen in e.g. connective tissue (7). Also the ECM stiffness is highly controlled in organisms and can vary from several hundred Pa (e.g. brain or fat) to MPa (e.g bone) in the elastic Young's modulus (8).
Studies during the last decade have shown that cells respond sensitively to structure, stiffness, and external forces. This is summarized under the topic mechanotransduction (9, 10). An important feature of the mechanosensitivity of cells is their ability to apply actively generated contractile forces to the ECM (4).

The Cytokeleton

The mechanical properties of eucaryotic cells are essentially determined by their cytoskelton (CSK), which is an intracellular mechanical scaffold composed of protein filaments. The CSK provides multiple functions: it gives cells its mechanical stability, enabling them to resist external stresses, serves as road system for intracellular transport, and as force generating machinery, which allows them to actively probe their

environment (7, 11). Three different filament types constitute the CSK (fig. 1.2): microtubles, intermediate filaments, and actin filaments. Microtubles are relatively stiff, and rod-like structures, composed of globular sub units (α- and β-tubulin) of $\sim 25nm$ in diameter, that can resist against relatively large compression forces (12). Intermediate filaments are made of sub units called coiled-coils, which are parallel arrangements of two α-helical proteins that form a dimer. These structures aggregate into large networks that span the whole cell providing resistance against shear stresses (13). Actin filaments are composed of globular actin monomers (G-actin), which have a size of $\sim 6nm$ (14). These monomers form μm-long, left-handed polar helical filaments by polymerization. Large families of actin associated proteins (15) are able to modify actin polymerization and cross-linking, and allow cells to form distinct actin structures either in terms of networks or bundles. Both structure types coexist on the scale of the entire actin-CSK. For example, a migrating cell usually forms a prominent network structure at the protruding part, while at the same time thick actin bundles are build at the rear part of the polarized cell (16, 17).

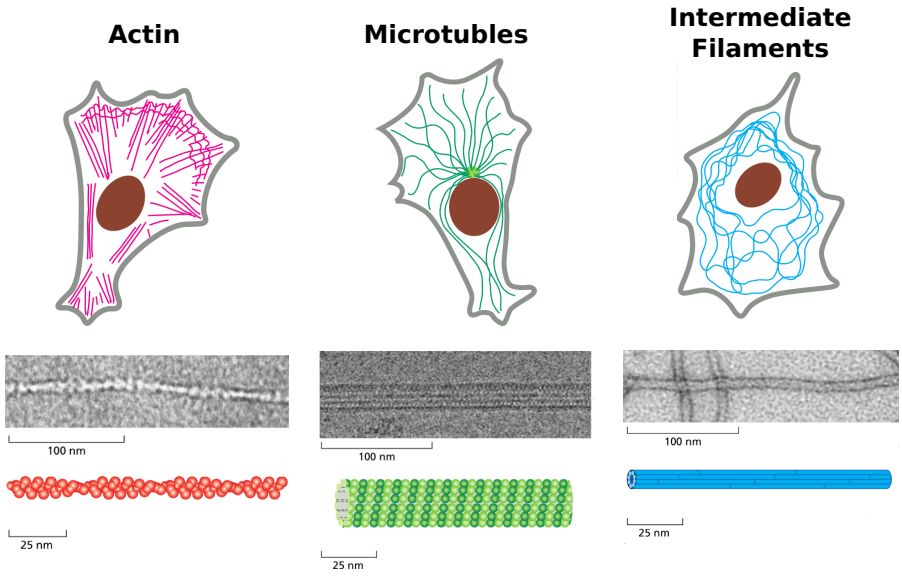

Figure 1.3: Components of the cytoskeleton. Actin filaments are assembled from polar double-stranded helical polymers made of globular actin proteins, which build up polymer networks or fibers. Microtubles are rigid hollow cylinders made of the protein tubulin. They from mostly a centered network spanning the whole cell. Intermediate Filaments are rope-like fibers, assembled from different fibrillar proteins. They form large providing mechanical stability, especially against shear forces. Figures taken from (7), with minor modifications.

A special class of actin binding proteins are myosin motor proteins (18). They are so-called mechanoenzymes, which are able to generate force while dephosphorylating ATP, a nucleotide that serves as energy source. Mainly smooth muscle myosin II proteins are

responsible for active contraction of the actin cytoskeleton. They are able to cross-link actin filaments with two active heads at both ends, causing sliding motion between the filaments. They can also form aggregates with other myosin II, proteins forming myofilaments. Eventually, complexes of myosin II and actin filaments (called actomyosin) form the elementary units of cellular contractility. These actomyosin complexes can be found in two structural forms, network and bundles. Here, especially thick contractile bundle structures, called actin stress fibers (SF), show high concentrations of myosin II and α-actinin corss-linking proteins often regularly ordered in periodic structures. The actin-cytoskeleton represents dynamic part of the CSK and generates the main part of cellular forces. Therefore, the actin CSK is for our study the most relevant part of the CSK, and will be considered in detail by this thesis. In order to transmit forces to the ECM, cells have to from a connection between the actin-CSK and the ligand proteins of the ECM. This is established by so-called focal adhesions (FA) introduced in the following.

Focal Adhesions

Cells bind to the ECM either specifically mediated by transmembrane proteins or unspecifically through the sugar coating of the cell membrane (glycocalyx). The actin-CSK is eventually coupled to molecules of the ECM like, for example, fibronectin or collagen by establishing a specific binding of intregrin proteins (19). These integrin-ligand contacts form clusters, known under the term focal complexes. During maturation of the adhesion, more and more proteins are recruited, forming complexes of up to $\sim$ 150 different proteins (20), who eventually connect intregrins to the actin CSK. Most of the force applied to the ECM is mediated by these FAs. Although there is a body of literature, e.g. (21, 22, 23, 24), that considers correlation of forces on the level of single FAs, it is still an issue of ongoing research. The large number of proteins incorporated in the FA and the knowledge about a central role in signaling of some of these proteins, suggest a sensory function and hence a central role in mechanotransduction (25, 26, 27). FAs are highly dynamic assemblies, which undergo force dependent maturation and degradation (28). This allows cells to quickly change their shape in order to adapt to changing properties of the environment or to persistently migrate through the tissue (29).

We now have introduced the most important cellular feature regarding mechanical cell-matrix interaction. The mechanics of substrate and cells are determined by their microscopic composition of nm molecules and sometimes several μm-large polymer

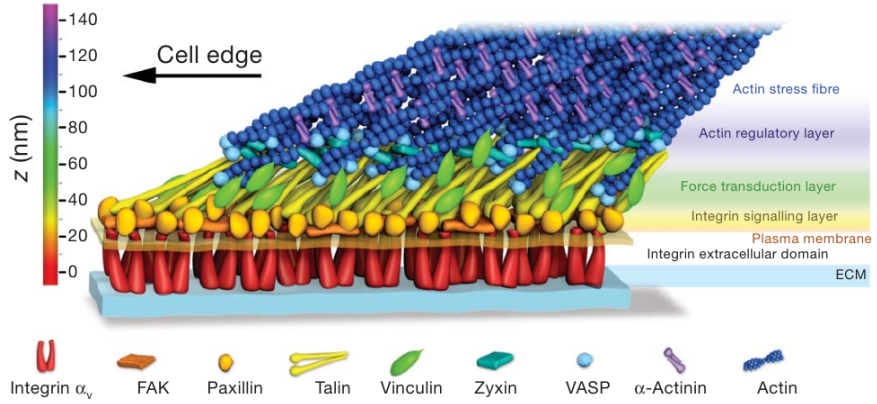

Figure 1.4: Focal Adhesion. Illustration of the hierarchical assembly and protein composition of the focal adhesion . Figure taken from (30).

structures. However, on a larger scale of several hundred μm, one can motivate a coarse grained description considering a mechanical continuum. In this thesis continuum approaches are used for both, to describe deformations of soft substrates in response to cellular traction stress, and to simulate cellular traction forces by whole cell contraction simulations. In the following we describe basic concepts of continuum elasticity theory, which shall give the reader a brief introduction into this topic.

1.3 Continuum Elasticity Theory

Solid materials usually consist of billions of atoms or molecules, which form macroscopic structures. In order to study whole material behavior on macroscopic scales it is not feasible to consider the physics of each single molecule. Continuum elasticity theory was developed based on sets of field quantities that describe mechanics of macroscopic systems. Thereby, the physics of microscopic material constituents is considered by averaging on much smaller scales than the size of a material sample. This implies that the application of continuum theory is limited to situations where structural components of the material appear on much smaller scales than the considered macroscopic scale. The following introduction is based on common literature (31, 32, 33, 34).

Elasticity theory describes the deformation response of a deformable body to applied forces either to the entire body or to its surface. Continuum elasticity theory is a tensor theory. The basic field quantities strain and stress, which will be introduced in the following, are second rank tensors. The material deformation response due to applied force is guided by a constitutive law that relates stress and strain. Like for any classical mechanical problem, the dynamics of the system is determined by the balance

of momentum.

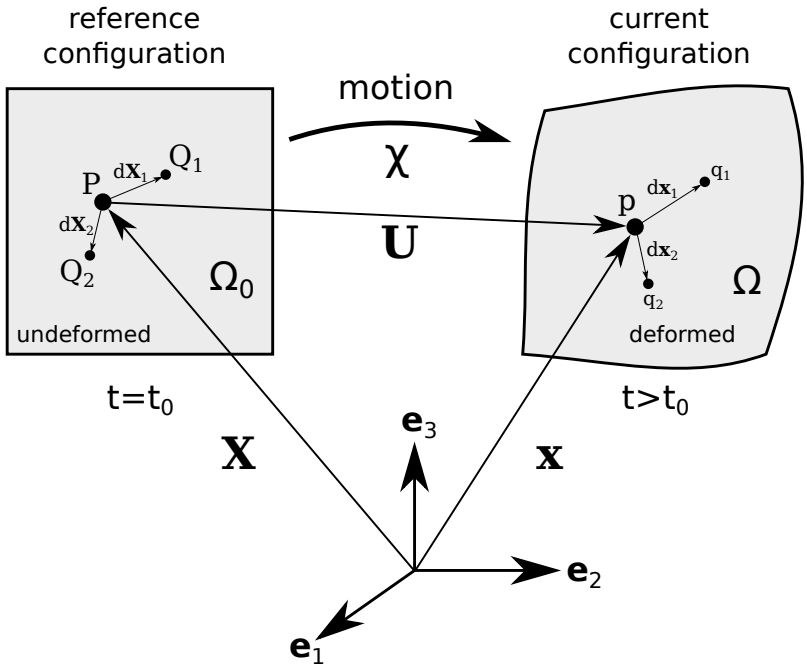

Figure 1.5: Deformation of a continuum body. At $t = t_0$ the body occupies the geometric region Ω_0. The position of a particle $P \in \Omega_0$ is given the vector $\mathbf{X}$. Due to a motion, at a later time $t > t_0$ the body occupies the new region Ω. The new position of particle $p \in \Omega$ is given by the vector $\mathbf{x}$. The motion is defined as $\boldsymbol{\chi} : (\mathbf{X}, t) \mapsto \mathbf{x}$. The displacement of the P from t_0 to t is given vector $\mathbf{U}(\mathbf{X}, t) = \mathbf{x}(\mathbf{X}, t) - \mathbf{X}$.

Strain

We first introduce the concept of strain or strain tensors. These are second rank tensor field quantities that kinematically describe deformations of an elastic solid. Now, we will give a brief derivation of the most important strain tensors which we are going to use in the following chapters.

Consider a motion like illustrated in fig 1.5. The reference frame for defining the position vectors is given by a orthonormal base $\{\mathbf{e_i}\}$ with $i = 1, 2, 3$. The region Ω_0 occupied by the undeformed solid at initial time $t = t_0$ is called the reference configuration, which is the relaxed state of the solid when no external forces are applied. The region Ω occupied by the deformed solid at a later time $t > t_0$ is called current configuration. Now consider the illustrative picture of a typical particle P at position $\mathbf{X}$ within Ω_0. After deformation, P can be related to a particle p at position $\mathbf{x}$ within Ω. The operation that relates the position in the reference configuration $\mathbf{X}$ with the

position in the current configuration $\mathbf{x}$ is called motion $\boldsymbol{\chi}(\mathbf{X}, t)$. In the same way the inverse motion $\boldsymbol{\chi}^{-1}(\mathbf{X}, t)$ maps back $\mathbf{x}$ to $\mathbf{X}$.

In general, all quantities derived in continuum mechanics can be formulated either with regard to the reference configuration, which is called material description or Lagrange form, or with respect to the current configuration, which is called spatial description or Eulerian form. Both descriptions are used in solid mechanics. This is different to continuum fluid dynamics since the reference state here has no meaning. In the finite elasticity theory, constitutive relations are most often stated in material description, while formulations in spatial description are often more convenient for efficient numeric implementation with finite element methods.

An important quantity in solid mechanics is the displacement field $\mathbf{U}$. Many classical linear elastic problems are formulated with respect to the displacement. The displacement in material and spatial description is defined as:

$$\mathbf{U}(\mathbf{X}, \mathbf{t}) = \mathbf{x}(\mathbf{X}, t) - \mathbf{X} \qquad (Lagrange\ frame) \tag{1.1}$$

$$\mathbf{u}(\mathbf{x}, \mathbf{t}) = \mathbf{x} - \mathbf{X}(\mathbf{x}, t) \qquad (Euler\ frame) \tag{1.2}$$

Note that the displacement in both descriptions is the same, however, the associated position and direction is different.

Although displacement fields seem to be intuitively a natural quantity for describing deformations, they have conceptual disadvantages. If, for example, we consider a rigid body motion in terms of body translation or rotation, the displacement field changes, although no body deformation takes place. Therefore, strains are more appropriate in elastic theories. The most essential strain quantity is the deformation gradient tensor $\mathbb{F}$ Consider two particle Q_1 and Q_2 next to P in the reference configuration (illustrated in fig 1.5). P is connected to Q_1 and Q_2 by the vectors $d\mathbf{X}_1 = \mathbf{X}_{Q_1} - \mathbf{X}_P$ and $d\mathbf{X}_2 = \mathbf{X}_{Q_2} - \mathbf{X}_P$. Due to the deformation the distances change due to body motion:

$$d\mathbf{x}_{1,2} = \mathbf{x}_{q_{1,2}} - \mathbf{x}_p = \boldsymbol{\chi}(\mathbf{X}_P + d\mathbf{X}_{Q_{1,2}}, t) - \boldsymbol{\chi}(\mathbf{X}_P, t) \tag{1.3}$$

If we now define the deformation gradient as

$$\mathbb{F} = \frac{\partial \boldsymbol{\chi}}{\partial \mathbf{X}} = \nabla \boldsymbol{\chi} = \frac{\partial \mathbf{x}}{\partial \mathbf{X}} \tag{1.4}$$

the mapping between $d\mathbf{X}$ and $d\mathbf{x}$ can be written as linear tranformation:

$$d\mathbf{x}_{1,2} = \mathbb{F} d\mathbf{X}_{1,2} \tag{1.5}$$

$\mathbb{F}$ is by definition invertible and positive definite. Thus, the mapping is invertible

$$d\mathbf{X}_{1,2} = \mathbb{F}^{-1} d\mathbf{x}_{1,2} \tag{1.6}$$

while $\mathbb{F}^{-1}$ is the inverse of $\mathbb{F}$. From the definition in eq. 1.4 it becomes clear that the deformation gradient can be considered as the Jacobi matrix that transforms coordinates from the reference to current configuration. Thus, a volume element can be transformed from the reference configuration to the current configuration by utilizing the Jacobian $J = \det \mathbf{F}$:

$$dv = JdV = \det \mathbb{F} dV. \tag{1.7}$$

We can further relate $\mathbb{F}$ to the displacement via:

$$\mathbb{F} = \frac{\partial \mathbf{U}(\mathbf{X}, t)}{\partial \mathbf{X}} + \mathbb{I} \tag{1.8}$$

where $\mathbb{I}$ is the unit matrix. $\mathbb{F}$ considers only length and orientation changes of a single line, which is not sufficient to characterize all modes of deformation properly. Further $\mathbb{F}$ is not symmetric and thus contains in 3d 9 independent components that must be determined to define a deformation. Therefore another measure is introduce defined through the scalar product of two vector element:

$$d\mathbf{x}_1 \cdot d\mathbf{x}_2 = d\mathbf{X}_1 \cdot \mathbb{C} d\mathbf{X}_2 \tag{1.9}$$

Recalling eq. 1.5 we define the conceptually most central strain quantity in material description, the right Cauchy-Green strain tensor:

$$\mathbb{C} = \mathbb{F}^T \mathbb{F} \tag{1.10}$$

The corresponding spatial equivalent is called left Cauchy-Green or Finger tensor $\mathbb{b}$:

$$\mathbb{b} = \mathbb{F}\mathbb{F}^T \tag{1.11}$$

which satisfies the following equation:

$$d\mathbf{X}_1 \cdot d\mathbf{X}_2 = \left(\mathbb{F}^{-1} d\mathbf{x}_1\right) \cdot \mathbb{F}^{-1} d\mathbf{x}_2 = d\mathbf{x}_1 \cdot (\mathbb{F}\mathbb{F}^T)^{-1} d\mathbf{x}_2 = d\mathbf{x}_1 \cdot \mathbb{b}^{-1} d\mathbf{x}_2 \tag{1.12}$$

Left and right Cauchy-Green strain are symmetric. However, they are abstract quantities since relation with intuitive modes of deformation like shear or stretch models are hard to associate from the components. If we think about strain we think more about how length and relative orientation of the line elements $d\mathbf{X}_1$ and $d\mathbf{X}_2$ change due to deformation, which can be expressed by:

$$\frac{1}{2}\left(d\mathbf{x}_1 \cdot d\mathbf{x}_2 - d\mathbf{X}_1 \cdot d\mathbf{X}_2\right) = d\mathbf{X}_1 \cdot \mathbb{E} d\mathbf{X}_2 \tag{1.13}$$

where $\mathbb{E}$ defines the well-known Green-Lagrange strain tensor. It is connected with $\mathbb{C}$ via $\mathbb{E} = \frac{1}{2}\left(\mathbb{C} - \mathbb{I}\right)$. This is again a strain tensor defined in material description, while the corresponding strain in spatial description is the so-called Almansi strain tensor given by $\mathbb{e} = \frac{1}{2}\left(\mathbb{I} - \mathbb{b}^{-1}\right)$.

At first glance multiple definitions of strain, both in material and spatial description, are confusing. However, as a rough orientation: the two defined strains in material descriptions are used to formulate constitutive laws, while $\mathbb{C}$ is a mathematically convenient strain and $\mathbb{E}$ is easier for physical interpretation.

The derivation of strain described above is the most general formulation, including the case large strains (finite strains). However, in many practical cases considering, the limit of deformations much smaller than the body size, the strain tensor can be linearized:

$$D\mathbb{E}[\mathbf{U}] = \frac{1}{2}\left(\nabla\mathbf{U} + (\nabla\mathbf{U})^T\right) \approx \epsilon \tag{1.14}$$

while D represents the Gateaux derivative with respect to $\mathbf{U}$ and ϵ symbolizes up to now the linearized strain.

Traction & Stress

External forces that act on all particles in the body volume are called body forces $\mathbf{f}$, with units of a force volume density $[N/m^3]$. Gravitation is a typical example for such a force. Apart from this, force can also be applied to the boundary of a deformable body. These are, for instances, compression forces or shear forces. Obviously they have the units of force area densities $[N/m^2]$. Like illustrated in fig. 1.6, consider a cutout surface of a body in current configuration (deformed state). A force $d\mathbf{f}$ acts on a unit surface element ds from which we can define a surface traction $\mathbf{t}$:

$$d\mathbf{f} = \mathbf{t} dS \tag{1.15}$$

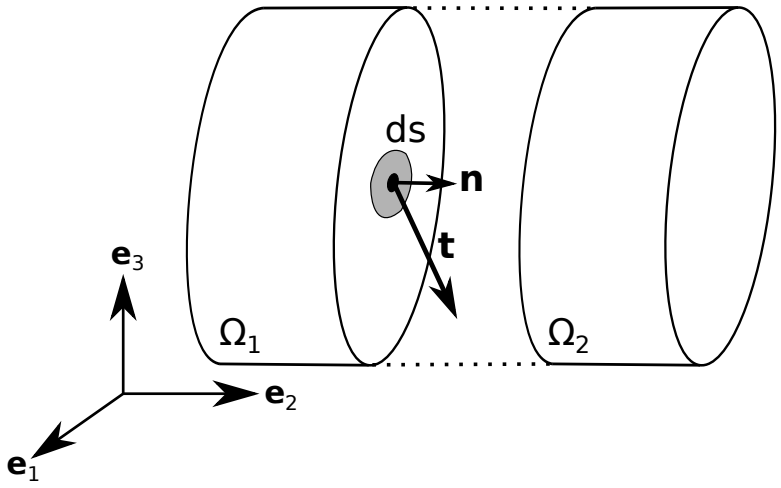

Figure 1.6: Cut through the cross-section of a continuous body divides the volume into to domains Ω_1 and Ω_2. The force a applied to a unite area element dS with surface normal vector $\mathbf{n}$ is determined by the traction vector $\mathbf{t}$.

is valid. Due to Cauchy's stress theorem, the traction vector can be uniquely mapped with respect to the normal vector of the corresponding unit surface element. The corresponding mapping tensor is called Cauchy stress tensor σ:

$$\mathbf{t} = \sigma \mathbf{n} \tag{1.16}$$

σ is a symmetric tensor with six independent components, which can be categorized in three possible normal stresses (parallel to $\mathbf{n}$) and three shear stresses (orthogonal to $\mathbf{n}$). E.g. if $\mathbf{n} = (1, 0, 0)$, due to eq. 1.16 the traction can be written as $\mathbf{t} = (\sigma_{11}, \sigma_{12}, \sigma_{13})$, while σ_{11} is the normal stress component and σ_{12} and σ_{13} are the shear stress components of the traction.

Different from strains, stresses are naturally described in spatial description, for in equilibrium situations force balance between external forces and internal elastic material stress is achieved. However, in order to formulate constitutive laws where stresses and strains meet, there is a need to define stresses in material descriptions. Analog to eq. 1.15 and 1.16, we write:

$$d\mathbf{f} = \mathbf{t} ds = \mathbf{T} dS \tag{1.17}$$

$$\mathbf{T} = \mathbb{P}\mathbf{N} \tag{1.18}$$

where $\mathbf{T}$ is the traction in material description, $\mathbf{N}$ the normal vector of unit area dS in material description, and $\mathbb{P}$ is the so-called first Piola-Kirchhoff stress tensor.

Combining both equations, we find

$$\sigma d\mathbf{s} = \mathbb{P} d\mathbf{S} \tag{1.19}$$

and by transforming the surface element in spatial description using Nanson's formula, $d\mathbf{s} = J\mathbb{F}^{-T} d\mathbf{S}$, the first Piola-Kirchhoff stress can be related to the Cauchy stress via:

$$\mathbb{P} = J\sigma\mathbf{F}^{-T} \tag{1.20}$$

$\mathbb{P}$ is non-symmetric, since eq. 1.20 contains the product of the symmetric Cauchy stress and the non-symmetric inverse and transposed deformation gradient. Correspondingly, $\mathbb{P}$ has nine independent components. The transformation described by eq. 1.20 is called Piola-Transformation. For reasons, which will become more clear in the context of hyperelasticity and the principle of virtual work, a symmetric stress tensor is defined in material description called Second Piola-Kirchhoff stress $\mathbb{S}$:

$$\mathbb{S} = \mathbb{F}^{-1}\mathbb{P} = J\mathbb{F}^{-1}\sigma\mathbb{F}^{-T} \tag{1.21}$$

Compared to $\mathbb{P}$, which is directly related to traction in material description there is no direct physical meaning related to $\mathbb{S}$. Recalling the introduction of strain, there are obvious similarities. Here, also the Green-Lagrange strain $\mathbb{E}$ has a direct physical meaning while the Cauchy-Green strain $\mathbb{C}$ is a conceptually more abstract quantity.

Equilibrium & Principle of Virtual Work

In static equilibrium, all forces acting on the body have to be balanced. Here, inertia forces vanish and Cauchy's momentum equation is given by:

$$\int_{\partial\Omega} \mathbf{t} ds + \int_{\Omega} \mathbf{f} dv = 0 \tag{1.22}$$

Using eq. 1.16 and applying Gauss's theorem, we can enclose both terms in eq. 1.22 with a single volume integral:

$$\int_{\Omega} (\nabla\sigma + \mathbf{f})\, dv = 0 \tag{1.23}$$

where, $\nabla\sigma$ denotes the divergence $\frac{\partial}{\partial x_j}\sigma_{ij}$. For arbitrary Ω eq. 1.23 implies the differential form:

$$\nabla\sigma + \mathbf{f} = 0 \tag{1.24}$$

Usually, eq. 1.24 is the main starting point for analytic analysis of elastic problems (31, 34, 35). E.g. we will see later that isotropic linear elastic problems eq. 1.24 can be expressed with respect to displacements by the Navier-Lameé equation.
Different from this, the numeric finite element method uses eq. 1.24 in weak form. The weak formulation is derived by multiplying eq. 1.24 an arbitrary test vector field, lets say $\delta\mathbf{u}$, and afterwards integrating the product:

$$\underbrace{\int_\Omega (\nabla\sigma + \mathbf{f}) \cdot \delta\mathbf{u} \; dv}_{\delta W} = 0 \tag{1.25}$$

while considering $\delta\mathbf{u}$ as arbitrary virtual displacement, the integral can be identified as variation of the work δW, which coincides with the principle of virtual work known from classical mechanics. If 1.24 is satisfied, also eq. 1.25 is satisfied.
We now apply the product rule for differentiation, $\nabla\sigma \cdot \delta\mathbf{u} = \nabla(\sigma\delta\mathbf{u}) - \sigma : \nabla\delta\mathbf{u}$, where the ":" operator denotes the tensor contraction ($\mathbb{A} : \mathbb{B} = A_{ij}B_{ij}$). After application of Gauss' theorem and identification of eq. 1.16, we derive:

$$\int_\Omega \sigma : \nabla\delta\mathbf{u} \; dv = \int_\Omega \mathbf{f} \cdot \delta\mathbf{u} \; dv + \int_{\partial\Omega} \mathbf{t}\delta\mathbf{u} \; ds \tag{1.26}$$

Recalling the symmetry of σ, we are able to replace $\nabla\delta\mathbf{u}$ by its symmetric part $sym(\nabla\delta\mathbf{u}) = \frac{1}{2}\left(\nabla\delta\mathbf{u} + \nabla\delta\mathbf{u}^T\right)$, which can be identified as the linearized Almansi strain δ :

$$\underbrace{\int_\Omega \sigma : \delta \; dv}_{\delta W_{int}} = \underbrace{\int_\Omega \mathbf{f} \cdot \delta\mathbf{u} \; dv + \int_{\partial\Omega} \mathbf{t}\delta\mathbf{u} \; ds}_{\delta W_{ext}} \tag{1.27}$$

This equation allows to separate the internal work δW_{int} done by elastic deformation associated with a change in strain δ due to material stress σ, and the external work δW_{ext} associated with changes in displacement due to applied traction $\mathbf{t}$ and body forces $\mathbf{f}$. Hence, eq. 1.27 requires that the external and internal work must be balanced. Depending on the specific application, the internal work might be expressed with respect to different stress and strain formulations. The corresponding pairs of stress and strain are called work conjugates. E.g. in spatial description σ and are work conjugates, in material description, $\mathbb{P}$ and $\nabla\mathbf{u}$ or $\mathbb{S}$ and $\mathbb{E}$ are work conjugates.
The derived quantities hold for small as well as for large deformations, while up to now no assumption was used (apart from e.q. 1.14). Thus the described theory holds for arbitrary large strains. To simplify the equation, which are in general non-linear, under the assumption in the limit of small strain a linear theory can be formulated.

Linear Elasticity

In order to reduce the theory to simpler linear equations essential two assumptions are made. Firstly, the strain-stress relation (constitutive law) is linear. Secondly we assume small strains, where we can use the linearized strain ϵ (eq. 1.14). Here, it is further assumed that the reference and current configuration coincides in first approximation, $\mathbf{x} = \mathbf{X}$. A general linear constitutive relation is given by

$$\sigma = \mathrm{C}\epsilon. \tag{1.28}$$

This linear mapping is determined by a constant fourth rank tensor C, called stiffness matrix, which consists of 81 independent response coefficients. In this work we only consider isotropic linear materials, for which eq. 1.28 can be simplified to

$$\begin{aligned} \mathrm{C}_{ijkl} &= \lambda\delta_{ij}\delta_{kl} + \mu(\delta_{ik}\delta_{jl} + \delta_{il}\delta_{jk}) && (1.29)\\ \Rightarrow \sigma &= \lambda tr\,(\epsilon)\,\mathbb{I} + 2\mu\epsilon && (1.30) \end{aligned}$$

where the strength of material response is determined by the Lamé coefficients λ and μ . If we consider static mechanic equilibrium and replace σ by eq. 1.30 in eq. 1.24, we derive the central linear elastic formulation with respect to the displacement $\mathbf{u}$ in terms of the Navier-Lamé equation:

$$\lambda\Delta\mathbf{u} + (\lambda + \mu)\,\nabla\nabla\cdot\mathbf{u} = \mathbf{f} \tag{1.31}$$

In many cases the description of material deformation by linear elasticity theory is sufficient. However, one has to keep the limitation to small strains in mind. In finite elasticity theory the concept of hyperelasticity is used to formulate constitutive laws in a convenient way. In the following a brief introduction is given to this concept, since it is also widely used for finite element formulations.

Hyperelasticity

Formulation of diverse constitutive relations can be established in a convenient way using the principle of hyperelasticity. This concept is essentially based on the idea to derive stresses from a scalar function associated with the stored elastic energy density $\Psi(\mathbb{F}, \mathbf{X})$, which is usually called strain energy density. A requirement for this approach is that the work done by changing the state of deformation to another is path-independent. Hence, the work can be written as energy difference,

$\Delta W(\mathbb{F}_1 \rightarrow \mathbb{F}_2) = \Psi(\mathbb{F}_2) - \Psi(\mathbb{F}_1)$. If this requirement is satisfied, a material is called hyperelastic. In order to associate material stress with the strain energy density, we consider the work done between time point t_0 and t associated with a deformation rate $\dot{\mathbb{F}}$:

$$\Psi = \int_{t_0}^{t} P(\mathbb{F}, \mathbf{X}) : \dot{\mathbb{F}} \; dt. \tag{1.32}$$

The integrand can be identified as strain energy density rate $\dot{\Psi} = \frac{\partial \Psi}{\partial \mathbb{F}} : \dot{\mathbb{F}}$ and we obtain by comparison the first Piola-Kirchhoff stress P as derivative of the strain energy density with respect to the deformation gradient $\mathbb{F}$:

$$\mathbb{P}(\mathbb{F}, \mathbf{X}) = \frac{\partial \Psi(\mathbb{F}, \mathbf{X})}{\partial \mathbb{F}} \quad \Leftrightarrow \quad \mathbb{P}_{ij} = \frac{\partial \Psi}{\partial \mathbb{F}_{ij}} \tag{1.33}$$

Due to objectivity (translation and rotation invariance) the strain energy density can be written with respect to other strain quantities:

$$\Psi(\mathbb{F}, \mathbf{X}) = \Psi(\mathbb{C}, \mathbf{X}) = \Psi(\mathbb{E}, \mathbf{X}) \tag{1.34}$$

while the second Piola-Kirchhoff stress is the corresponding work conjugate:

$$\mathbb{S} = 2\frac{\partial \Psi(\mathbb{C}, \mathbf{X})}{\partial \mathbb{C}} = \frac{\partial \Psi(\mathbb{E}, \mathbf{X})}{\partial \mathbb{E}} \tag{1.35}$$

The simple material model that characterizes a linear constitutive law in finite strain elasticity is given by the Staint-Vernant model, which is defined by

$$\Psi(\mathbb{E}) = \frac{1}{2}\lambda tr(\mathbb{E})^2 + \mu \mathbb{E} : \mathbb{E} \tag{1.36}$$

$$\Rightarrow \mathbb{S} = \frac{\partial \Psi(\mathbb{E})}{\partial \mathbb{E}} = \lambda tr(\mathbb{E})\mathbb{I} + 2\mu \mathbb{E} \tag{1.37}$$

Comparing 1.37 and 1.30 reveals the only difference between finite strain and linear elasticity is that $\mathbb{E}$ is replaced by the linearized strain ϵ. Thus, the material law is linear, nevertheless the constitutive law is nonlinear in $\mathbf{u}$. Here, the literature of continuum elasticity theory distinguishes between the two types material nonlinearity and geometric nonlinearity. The first term indicates a nonlinear material law, the second the consideration of finite deformations.

This thesis deals exclusively with isotropic material models. Isotropy here implies a identical constitutive relation in all directions. Therefore the functional dependence of Ψ on $\mathbb{C}$ must be independent from chosen material axes, hence, it can only depend on

three invariant quantities, known as strain invariants:

$$I_1^C = \mathbb{C} : \mathbb{I} = tr\,(\mathbf{C}) \tag{1.38}$$

$$I_2^C = \mathbb{C} : \mathbb{C} = tr\,(\mathbf{CC}) \tag{1.39}$$

$$I_3^C = J^2 = \det(\mathbb{C}) \tag{1.40}$$

In general all possible isotropic strain energy densities can be written as functions dependent on these invariants, $\Psi = \Psi(I_1^C, I_2^C, I_3^C)$. Applying the chain rule to eq. 1.35 results a general form for constitutive laws in material description (here we use $\frac{\partial \Psi}{\partial I_3^C} = \mathbb{C}^{-1}$, for which we refer to the corresponding literature (32, 33)):

$$\mathbb{S} = 2\frac{\partial \Psi}{\partial I_1^C}\mathbb{I} + 4\frac{\partial \Psi}{\partial I_2^C}\mathbb{C} + 2J^2\frac{\partial \Psi}{\partial I_3^C}\mathbb{C}^{-1} \tag{1.41}$$

Here, the calculation of stresses is reduced to the execution of scalar derivatives of the strain energy density with respect to the three strain invariants, and calculation of the right Cauchy-Green strain and inverse right Cauchy-Green strain. The same formulation in spatial description is written in terms of the left Cauchy-Green strain $\mathbb{b}$:

$$\sigma = 2J^{-1}\frac{\partial \Psi}{\partial I_1^b}\mathbb{b} + 4J^{-1}\frac{\partial \Psi}{\partial I_2^b}\mathbb{b}^2 + 2J\frac{\partial \Psi}{\partial I_3^b}\mathbb{I} \tag{1.42}$$

Compared to material description the third term is simpler, while the dependence on the inverse is replaced by dependence on the unit matrix. Since the third term can be directly associated with volume changing deformations, the spatial formulation is especially helpful for modeling incompressible or nearly compressible materials (36).

Now we have introduced the necessary quantities of elasticity theory for application to the biological problem. This thesis focuses on reconstruction and simulation of cellular forces. Considering the first, cellular force reconstruction means to determine cellular traction fields from measured substrate deformations, which represents the inverse problem of the theory discussed above, where we considered substrate deformations in response to applied forces. In the following, we give a detailed overview about the development cellular traction force microscopy and modern advances in this field.

1.4 Traction Force Microscopy

During the last decades, it has become clear that physical and geometrical properties of the environment have a large impact on cellular behavior such like cell proliferation, migration, and differentiation (8, 9, 37). In order to measure the mechanics of the environment cells exert active forces, corresponding methods have been developed, which are summarized under the term traction force microscopy (TFM).

Deformable substrates

The development of TFM started with first experiments by Harris, Wild and Stopak 1980 (38). They developed a substrate made of a thin sheet of cross-linked silicone ($\approx 1\mu m$) on top of liquid unpolymerized silicone. Due to the small thickness of the sheet the effective stiffness was sufficient small that adherent cells could wrinkle the substrate, which was observable with common light microscopy - see fig 1.7 (A). Harris and coworkers estimated the exerted shear force by comparison with wrinkles induced by calibrates elastic glass micro needles and achieved for the first time a value for cellular traction, on the order of $1nN/\mu m^2$ for chicken heart fibroblasts (38). In following experiments, they were able to show that force magnitudes vary for different cell types (39). Although this technique allows a rough estimation of cellular traction, quantitative measurement with sub cellular resolution was not possible. The main reason for this is that wrinkling is a highly nonlinear and chaotic phenomena in material science and precise force reconstruction is not achievable. Improved substrate

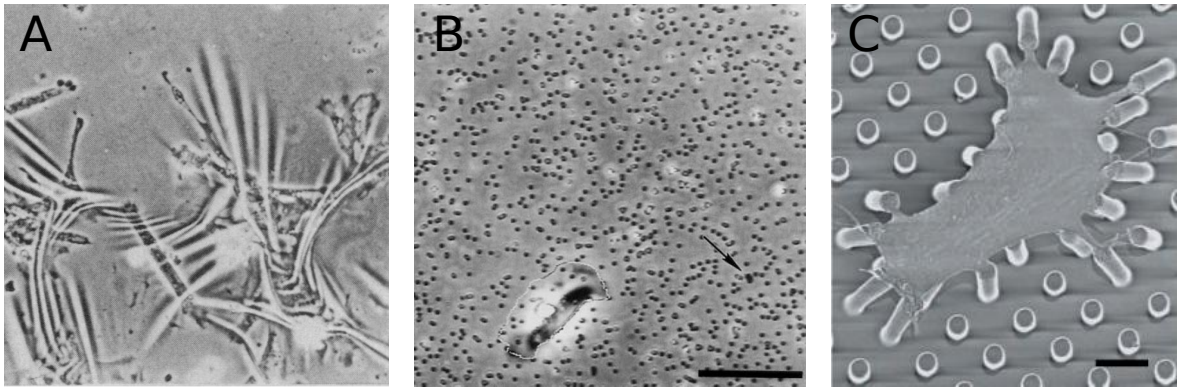

Figure 1.7: Use of elastic substrates to measure cellular traction forces. (A) Wrinkling assays - thin silicon sheet wrinkling under cellular traction, taken from (38). (B) Bead assay - displacement of embedded marker beads as measure for local substrate deformation, taken from (40). (C) Pillar assay - micro pillars fabricated by micro molding techniques. Measurement of pillar deflections due to cellular forces. Taken from (41).

preparation was subsequently accomplished by placing silicone into small chambers. The resulting sheet sticked to the chamber walls and due to effective contraction of the sheet during polymerization, mechanical tension was build up, which they called 'drumhead prestress' (40, 42). The improvement compared to the work by Harris (38) was that the tension prevents the substrate from wrinkling and makes it possible to calculate forces from substrate deformations. In order to determine local substrate displacements micrometer sized latex beads were distributed over the substrate, see fig 1.7 (B). By comparison of the same image sections in the deformed and undeformed state using single particle tracking small local substrate displacements could be measured with sub cellular resolution (40, 42, 43). The main disadvantages of thin silicone sheets is a fairly reproducible substrate preparation.

The problem was overcome by the development of polyacrylamid (PAA) gels (44). These are several ten to hundred μm thick substrates, which are rigidly attached to a glass cover slip. Similar to the tensed silicone sheet beads are distributed either within or on top of the gel in order to detect substrate displacements. The main advantages of this gel are an easy fabrication process and a tuneable substrate stiffness (controlled by the ratio of polymer and cross-linker concentration). Similar silicone substrate was developed based on polydimethylsiloxane (PDMS) (21). PDMS substrates are in particularly suitable for approaches which use micropatterning. Balaban et al. (21) for example used this to create regular patterns of fluorescent photoresist as displacement markers. Further, Tan et al. developed a traction force measurement technique base on the fabrication of arrays of micro pillars (pillar assay) (41). Adherent cells can pull on these pillars while their deflection is measured using common light microscopy, see fig 1.7 (C). Since neighboring pillars are not elastically coupled to each other and a formula can be derived from elasticity theory that relates applied force F to pillar deflection δ, $F = (\frac{3EI}{L^3})\delta$. Here, E is the Young's modulus of the material, I the moment of inertia of the pillar, and L the pillar height. Due to this relation, force reconstruction is simple (41). For the sake of completeness also rigid silicon substrates found application in the early stage of traction force microscopy. Galberaith and Sheetz developed a so called micromachined device to measure cellular forces (45). Here, the idea was (similar to Tan et al. (41) later), to achieve a precise local measurement of force without interference of other forces, which is not avoidable in experiments on homogeneous substrates. They fabricated patterns of micro-patches, which they etched out of a block of silicon. Each micro-patch remains attached to the bulk by a strip of material, acting as elastic cantilever. Focusing on fast migrating fibroblasts cells, patch displacements were measured while cells migrated over them. By comparing forces at different cellular

locations they were able to reconstruct a characteristic force profile of a migrating cell. Due to complex substrate fabrication and grown evidence that stiffness and topography effects cell behavior nowadays micromachined devices are only rarely used. Compared to that, the pillar approach is still a popular method, due to an attractively simple force reconstruction. Nevertheless, this technique has limited resolution constraint by density and separation distance of the pillars and also artificial cell behavior induced by the provided topography can not be entirely excluded.
Compared to the pillar assay, bead based approaches on solid deformable substrates are less limited. The resolution can be well tuned by increasing the bead density and using high resolution optical microscopy (22, 46, 47). Further the homogeneity of the adhesion area reduces topographic effects. The pay off for this benefit is a complex mathematical traction reconstruction, which will be discussed in the following.

The first experiments by Harris et al. (38) and also early studies on tensed silicone sheets decorated with mircobeads (40, 42) achieved only qualitative force fields by trying to reproduce measured deformation fields by one or multiple calibrated micro needles. Afterwards they calculated forces from the deflections of these needles. This allows, of course, just to rough estimate forces with poor spatial resolution. Nevertheless, they were able to find the typical order of magnitude which is $nN/\mu m^2 \Leftrightarrow kPa$ (the corresponding papers use the historical force unit *dyn*. For the sake of comparability, we converted units to SI standard). Since the late 90s, many effort went into the development of mathematical approaches to reconstruct cellular force field directly from given substrate bead displacement patterns. In this work we categorize these techniques into two classes: standard methods and advanced methods. Standard methods are a bunch of methods that have been developed just within a few year after the development of elastic gels as substrates. They use similar approximations regarding the applied substrate model, but they are very different in the way how they describe the traction field and how they invert the elastic problem. Further, they are constraint to planar substrate topography and linear elasticity. Due to these constraints diverse modern methods have been developed that almost exclusively are based on the use finite element methods (FEM). In the following a detailed overview is given over both classes of approaches.

Standard traction reconstruction methods

The first quantitative reconstruction method to measure traction patterns with sub cellular resolution was proposed by Dembo et al. originally for silicone sheets (43) and thick substrates (48). The transformation of locally measured bead displacements into a map of cellular traction is an inverse problem. It requires a substrate material model, which determines substrate deformations in response to applied cellular forces, which represent the direct problem that needs to be inverted. Dembo et al. considered the substrate as elastic halfspace for which a analytic point force solution exist, known under the term Boussinesq solution (34). Considering a traction field $\mathbf{t}(\mathbf{x})$ as superposition of point forces, we can establish the integral form of the elastic problem:

$$\mathbf{u}(\mathbf{x}) = \int_{-\infty}^{\infty} G(\mathbf{x};\mathbf{x}')\mathbf{t}(\mathbf{x}')\ dA' \tag{1.43}$$

According to Green's formalism this is a convolution integral that results the displacement field solution $\mathbf{u}(\mathbf{x})$. $G_{ij}(\vec{x},\vec{x}')$ is the Boussinesq Green's tensor (3×3 matrix). The tensor formulation arises from multiple directional combinations of force application and material response. Dembo's approach assumes that displacements are measured directly at the substrate surface where traction is applied and further displacements are only recorded in lateral direction neglecting displacements normal to the substrate surface. The later is a well-justified assumption since cells mainly exert forces in lateral directions and for incompressible materials (like PAA or PDMS: poisson ratio $\nu \approx 0.5$) the z-direction decouples from lateral directions. Hence, the Boussinesq Green's matrix can be reduced to a 2×2 matrix:

$$G(r,\mathbf{x}) = \frac{3}{4\pi E}\frac{1}{r^3}\begin{pmatrix}(r^2+x^2) & xy \\ xy & (r^2+y^2)\end{pmatrix} \tag{1.44}$$

where $r = \sqrt{(x-x')^2(y-y')^2}$ is the distance between $\mathbf{x}$ and $\mathbf{x}'$, and E is the Young's modulus of the substrate. Considering a point force, $G(r,\vec{x})$ is everywhere invertible ($\det G = r^4 + r^2(x^2+y^2) > 0$) apart from the singularity at $\mathbf{x} = \mathbf{x}'$. Far away from the traction source the displacement field decays with $1/r$. According to Saint-Vernant's principle, the difference between the displacement field of two different but statistically equivalent traction distributions (same net traction) decays with the distance from the traction source. In other words, far away, the displacement becomes the same regardless from the particular traction pattern and is only determined by the net load. Analog to 0th order multipole expansion in electrostatics. This has important implications for

the resolution of traction reconstruction because it says that displacement measurements near to features of the traction pattern are more important than measurements more far away.

We now get back to the traction reconstruction problem, where eq. (1.43) determines the direct problem. The inverse traction reconstruction problem is stated as deconvolution. Because of the finite density of bead displacement measurements and experimental noise, the inverse problem of eq. (1.43) is ill-posed, which means that solutions are either ambiguous or unstable (49). Dembo followed the common approach to solve an inverse ill-posed problem and considers the the reconstruction as optimization problem. To find an optimal traction field solution, different traction pattern are generated and compared with the data by using an error estimate. For this purpose the problem get spatially discretized by representing cell area in terms of a mesh. The traction field here is determined by a finite set of nodal traction values, which build of a continuous solution by interpolation. Thereby the integral in eq. (1.43) gets discretized and eq. (1.43) can be written as linear algebraic equation. This represent a common approach in finite element numerics and is called Boundary element method (BEM). Therefore we call up to now Dembo's method just BEM.

To solve ill-posed inverse problems, a prior information about the shape of the expected traction field needs to be introduced in the optimization process. As the simplest approach, one can require that solutions should be sufficient smooth which incorporates penalization of peaked solutions. This can be achieved by Tikhonov regularization introduced by Tikhonov and Arsin (50). We will introduce and discuss Tikhonov regularization later in chapter 2 and 3. The application of this approach delivered for the first time quantitative traction patterns with sub-cellular resolution like depicted in fig 1.8 (B). Another method has been proposed by Schwarz et al. (52), which focuses on measuring traction forces associated with mature FAs. The method is called traction reconstruction by point forces (TRPF). Compared to the BEM method, which constrains traction to the visible cell area, TRPF assumes that tractions hot spots are associated with focal adhesions (FAs). This requires additional information about the distribution of FAs, which can be obtained by staining FA proteins and applying fluorescence microscopy. It is further assumed that cellular traction stress is distributed in terms of point forces. Using this, the total traction field can be written as of point forces: $\mathbf{F}(\mathbf{x}) = \sum_{i=1}^{N_{FA}} \mathbf{F}_i \delta(\mathbf{x}-\mathbf{x}')$, where $\mathbf{F}_i$ is the force associated with the ith FA and $\delta(\mathbf{x})$ the Dirac delta function. The integration property of $\delta(\mathbf{x})$ ($\int f(x')\delta(x-x')dx' = f(x)$)

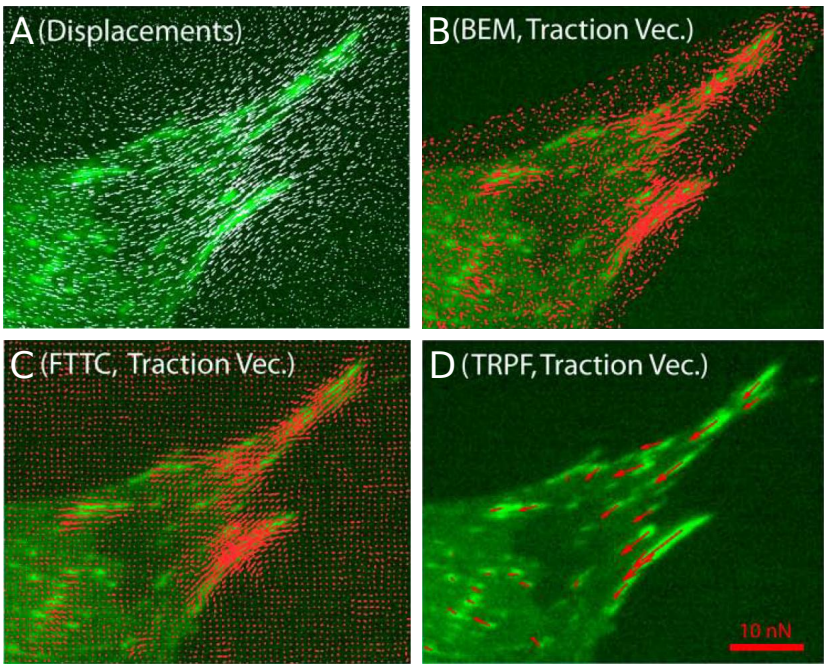

Figure 1.8: Cellular traction fields achieved by different standard methods. (A) Bead displacement field with paxillin fluorescence (adhesion area) as background. (B) Traction field result from method from Dembo et al. (43, 48). (C) Traction field result achieved with FTTC method according to Butler et al. (51). (D) Point force reconstruction TRPF with method from Schwarz et al. (52). Images taken from (46).

leads automatically to the discrete form:

$$\mathbf{u}(\mathbf{x}) = \sum_{i=1}^{N_{FA}} G(\mathbf{x}, \mathbf{x}_i)\mathbf{F}_i \tag{1.45}$$

The inversion of eq. 1.45 is in a similar way achieved as for the BEM method by considering a optimization problem minimizing a least square error estimate ($L2$). Due to the ill-posedness of the problem, in TRPF a 0th order Tichonov regularization term is added. The minimization problem then reads:

$$\min_{\mathbf{F}_i} \left\{ \sum_{i=1}^{N_{disp}} \left(\mathbf{u}(\mathbf{x}_i; \mathbf{F}) - \mathbf{u}^{exp}(\mathbf{x}_i)\right)^2 + \lambda^2 \sum_{k=0}^{N_{FA}} |\mathbf{F}_k|^2 \right\} \tag{1.46}$$

$\mathbf{u}(\mathbf{x}, \mathbf{F})$ represent the solution of eq. 1.45, $\mathbf{u}^{exp}(\mathbf{x}_i)$ is the experimentally measured displacement at position $\mathbf{x}_i$, and λ is a regularization parameter. The regularization represents a side constraint that penalizes solutions with extensively high total forces, which typically goes along with large noise effects. However, the introduction of a free parameter in terms of λ makes the solution non-unique. Large values for λ smooth

the traction field extensively, which effectively broadens traction spots and reduces the overall traction magnitude. Small values might again prefer noise dominated solutions. Without introducing any further information about the system the common way is to optimize λ with respect to the regimes of too large and too small values. This can be achieved by methods like cross validation (CV) or the L-curve criterion (53). An example for a reconstruction solution achieved by TRPF is depicted in fig. 1.8 (D).
The two methods explained above, both need additional information apart from the displacement field. Either the cell shape, for discretizing the traction field in BEM, or fluorescence images that visualize FAs when using TRPF. Butler et al. developed a method that works independent from additional information and is called fourier transform traction cytometry (FTTC) (51). The basic idea behind this method is to consider the elastic problem (eq. (1.43)) in fourier space. This effectively eliminates the integral in eq. 1.43 and leads to a linear algebraic system:

$$\tilde{\mathbf{u}}(\mathbf{k}) = \tilde{G}(\mathbf{k})\tilde{\mathbf{T}}(\mathbf{k}) \tag{1.47}$$

$\tilde{\mathbf{u}}$, $\tilde{G}$, and $\tilde{\mathbf{T}}$ are the displacement, Green's matrix and traction in Fourier space. Here, Butler et al. (51) derived an analytic expression for the elastic halfspace in Fourier space, $\tilde{G}$. This equation can be inverted since $\tilde{G}$ is invertible and numeric inverse Fourier transformation yield the desired traction field in real space:

$$\mathbf{T}(\mathbf{x}) = FT^{-1}(\tilde{G}^{-1}\tilde{\mathbf{u}}) \tag{1.48}$$

where $\tilde{G}^{-1}$ is the inverse of the transformed Green's matrix. In practice forward and backward transformation is done numerically and therefore $\mathbf{u}$ and $\mathbf{T}$ need to be available on a regular lattice. This requires a pre-processing step where bead displacements get interpolated to a grid. In the original paper by Butler et al., it was claimed that this approach represents no more an ill-posed situation due to unique inversion in Fourier space and thus don't need regularization. However, Schwarz et al. (52) showed with simulated data sets that regularization is needed due to the presents of experimental noise in the data. Note, the conditioning whether the problem is ill-posed or well-posed is also influenced by the grid constant used for numeric calculation. It is clear, that the dimensionality of the solution space growth with grid refinement. Therefore, it is an extraordinary feature of inverse problems that too fine discretization does not improve the accuracy of the solution anymore, but lead to ill-posedness. Thus, for a grid which is coarse enough the problem is possibly well-posed, however, with increased refinement regularization is again needed. Accommodating this finding, a regularized version of

FTTC was developed by Sabass et al. (46), for which a typical result is depicted in fig. 1.8 (C). Compared to BEM and TRPF, FTTC is the fastest method, while a single traction field is usually evaluated in several seconds.
Most of the current experimental studies use one of the three described standard methods. During the last decade they have largely contributed to the current knowledge about mechanisms of mechanotransduction and force generation in cells. However, these techniques are limited to analytic Green's functions, in particular to the Boussinesq solution. Thus the traction reconstruction is constraint to planar and sufficient thick substrates, while finite substrate thickness can be managed by a analytic Green's function for finite substrate layers introduces by Merkel et al. (54).

In organisms, cells commonly experience environments of diverse geometries. Fibroblast e.g. life in a three dimension gel-like matrix while e.g. kidney podocytes life on a curved membrane in the glomerulus. For the purpose of studying cells in natural geometries different substrates have been developed to e.g. embedd cells in a polymer gel (55) or curved non-planar substrate (Nils Hersch and Nico Hampe, FZ Jülich, unpublished). These situations are no more covered by standard traction reconstruction methods. During the last years different methods based on finite element substrate modeling have been developed to overcome described limitations.

FEM-based Traction Force Microscopy

These types of methods have been developed to overcome limits of the described standard techniques. They are especially suitable when considering complex substrate geometries or material models. However, compared to standard procedures, they are numerically more difficult, which increases computation time.
From a historical point of view Ambrosi (56, 57) proposed the first method based on FEM. Although he considered only two-dimensional traction, linear elasticity, and planar geometry, which is a situation covered also by standard methods, the formulation of the optimization problem is mathematically elegant. The basic idea behind this method, which we call up to now adjoint method (57), is to formulate the problem in terms of a Lagrange-type functional and search for a stationary state. While introducing linear elasticity in term of the Navier-Lamé equation, which has been still introduced in the previous chapter, e.g. 1.31, the optimization problem can be written in terms of a coupled system of Lamé-like equations associated with the forward and the adjoint problem. The equation system written in the original paper (56) is slightly

different from how we introduce it here (missing the characteristic functions on the right hand side). For the problem formulation these are not necessary and the given derivation here is more simple:

$$\hat{\mu}\Delta\mathbf{u} + (\hat{\mu} + \hat{\lambda})\nabla\nabla \cdot \mathbf{u} = \frac{1}{\epsilon}\mathbf{p} \tag{1.49}$$

$$\hat{\mu}\Delta\mathbf{p} + (\hat{\mu} + \hat{\lambda})\nabla\nabla \cdot \mathbf{p} = P\mathbf{u} - \mathbf{u}_0. \tag{1.50}$$

$\mathbf{u}$ is again the displacement field resulting from the forward problem, $\mathbf{p}$ is the variable of the adjoint problem, and corresponds to the cellular shear stress, ϵ is a penalty parameter similar to the regularization parameter defined before and P is a projection operator that projects the displacement field to measurements displacements $\mathbf{u}_0$. The derivation from the paper (56) uses the Gateaux derivative to achieve the stationary equation. An equivalent derivation can be deduced from considering a PDE constraint optimization problem, where the PDE and the regularization term are applied as Lagrangian constraint. By deriving the same eqs. 1.49 and 1.50, $\mathbf{p}$ can be identified as field of Lagrangian multipliers. The adjoint formulation is elegant, since it reduces the optimization problem to a a coupled system of PDEs, which can be solved in parallel instead of using iterative minimization procedures. Unfortunately, the approach is hard to transfer into the three-dimensional traction reconstruction since the two-dimensional elasticity approximation avoids difficulties when formulating the adjoint equation. The method derivation utilizes zero displacement boundary conditions while the boundary is assumed to be far away from the traction sources. Also the traction is converted into a body force in the two-dimensional case. Compared to that the three-dimensional case needs optimization of the boundary condition, which leads to more complicated surface integrals, while formulating the adjoint equation.

A methodically very different FEM approach has been developed by Hur et al. (58, 59). It uses FEM as suitable tool to solve mixed boundary value problems (BVPs). Mixed boundary conditions here mean that both types of boundary conditions in elastic systems appear in the equations, stress and displacement boundary conditions (31). The approach considers a cuboid substrate region around the traction source with finite thickness and extension. Subsequently on this domain the elastic BVP is formulated with respect to the Cauchy stress $\sigma(\mathbf{x})$ in the stationary state formed by the following

equations:

$$E_{ij} = \frac{1}{E}\left[(1+\nu)\,\sigma_{ij} + \nu\delta_{ij}\sigma_{kk}\right] \tag{1.51}$$

$$\frac{\partial \sigma_{ij}}{\partial x_i} = 0 \tag{1.52}$$

$$E_{ij} = \frac{1}{2}\left(\frac{\partial u_i}{\partial u_j} + \frac{\partial u_j}{\partial u_i} + \frac{\partial u_k}{\partial u_i}\frac{\partial u_k}{\partial u_j}\right) \tag{1.53}$$

The first equation is the inverted constitutive relation for a linear isotopic material. It determines the material deformation response in terms of the Green-Lagrange strain E (already introduced in the previous section) with respect to a given Cauchy stress σ. The second equation is Cauchy's momentum equation already introduced above. It defines the stationary material state. Eq. 1.51 and 1.52 form a linear partial differential equation with respect to the Cauchy stress σ. For application of displacement boundary conditions, the strain has to be related to displacements, which is determined by the third equation, where the strain is written in terms of derivatives of the displacement. The approach by Hur et al. utilizes the following boundary conditions: zero stress on the side surfaces of the cuboid, $\sigma\mathbf{n}$, with surface normal vector $\mathbf{n}$), zero displacement at the bottom surface, $\mathbf{u} = 0$, where the substrate is rigidly bound to glass cover slip, and interpolated displacement boundary conditions based on measured bead displacements - as depicted in fig. 1.9 (B). With these BCs the BVP for the equation system above is fully determined and can be solved numerically with FEM. The result of this calculation is the material Cauchy stress σ from which the cellular traction at substrate surface can be derived by using Newton's third law $\mathbf{t} = \sigma\mathbf{n}$. The approach uses no kind of regularization. However, the measured displacements enter the equation in terms of derivatives, thus noise effects might be amplified in the reconstructed traction field as pointed out in (52). The authors validated their method with simulated data contaminated with additive Gaussian noise of different strengths and measured a relative deviation of the root mean square $\Delta t = \|t_{sim} - t_{recon}\|$ of traction up to 25% for a Gaussian noise standard deviation of $200nm$. For a study with bovine aortic endothelial cells (BAECs), they determined a non-zero traction in normal direction, while observing substrate indentation around the cell center and extractional deformations at the cell edge (see fig. 1.9 (C)).

A recently proposed method, which focuses on the traction reconstruction problem for cells embedded in an elastic matrix was introduced by Legant et al. (55). This method can also be used to reconstruct three-dimensional traction patterns on planar

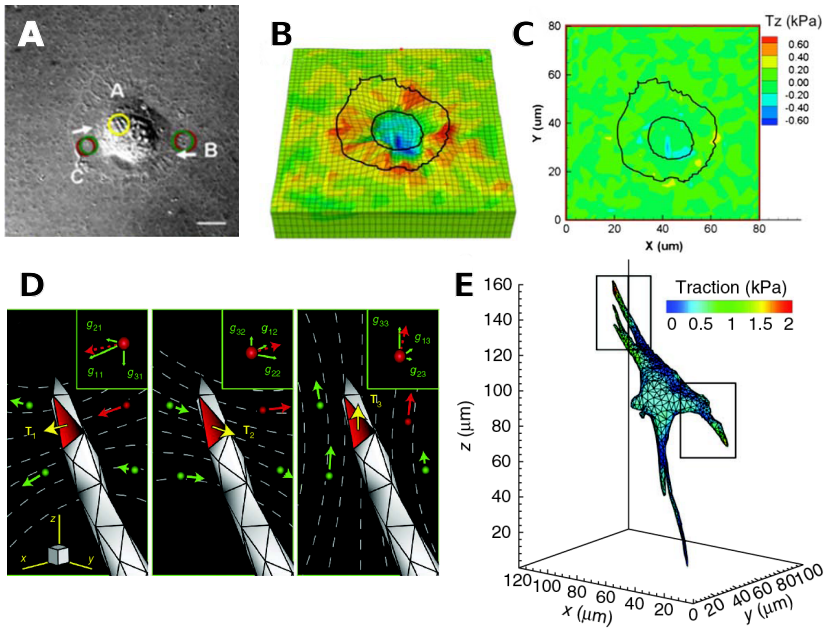

Figure 1.9: Advanced traction reconstruction methods. (A)-(C) Hur et al. approach (58): (A) Phase contrast image of a bovine aortic endothelial cell (BAEC). (B) FEM mesh with interpolated displacement measurements (color & deformation). (C) Out-of-plane component of the reconstructed three-dimensional traction. (D)-(E) Legant et al. approach (55): (D) Illustration that depicts the construction of a discretized Green's function via application of unit tractions on cell mesh facets in three spatial directions. E) Traction reconstruction result at the cell surface. All images taken form the corresponding publications (55, 58)

substrates like demonstrated in (60). Compared to the direct BVP method by Hur et al., this approach utilizes the integral formulation for the displacement, eq. 1.43, and the beads are distributed within the entire substrate volume. In case of embedded cells no analytic Green's matrix is available and moreover it changes for each experimental situation due to different cell shapes. To overcome this problem a discretized Green's matrix is numerically evaluated using FEM. Therefore the forward problem is solved for individual point forces, schematically depicted in fig 1.9 (D). For each facet of the cell surface mesh unit loads are applied separately pointing to different possible spatial directions. The corresponding FEM solutions are merged to a discrete field of local Green's matrices and the forward problem eq. 1.43 can be solved based on superposition according to different configurations of facet loads. From this starting point again standard traction reconstruction techniques can be applied replacing the analytic by a numerically evaluated discretized Green's function. Legant et al. inverted the problem by minimizing a least square estimate with a $0th$ order Tichonov with respect to the facet loads similar to the TRPF method (46, 52). A reconstruction example for a fibroblast cell embedded in hydrogel matrix is shown in fig. 1.9 (E). The Legant et

al. method represent a pragmatic hybrid method since it uses FEM numerics to face complex geometries, however, tracing back the problem to well-established standard techniques. Comparing this with the Hur approach the Legant method is more flexible since beads don't have to be distributed to a special surface.

In summary, the three methods described represent a broad overview over this massively growing topic of advanced cellular traction reconstruction techniques. It illustrates different points of view depending on the educational background of the developers: from mathematics with the Ambrosi method, from material engineering corresponding the Hur's method, or from Bioengineering according to Legant's approach.

1.5 Aims & Outline

The objective of this work was to establish improved reconstruction and simulation of cellular forces. In detail, we wanted to develop appropriate methods to reconstruction cellular traction fields on topographic substrates, to improve traction reconstruction on planar substrates, and to simulate force generation of adherent cells. In order to achieve this goal we combined finite element numerics with cell contraction modeling, and multidimensional parameter optimization for reconstructing cellular traction from measured substrate deformations. We further simulated cellular contraction with thermoelastic continuum theory applied to the concrete biologically relevant situations of leader cell formation in constrained cell monolayer colonies and tissue invasion of metastatic cancer cells. This thesis is divided into three main chapters, for which we give a short outline:

- In chapter 2 we introduce a finite element based approach suitable for 3d traction reconstruction on elastic substrates with micro-topography. Therefore, we implemented effective finite element calculation utilizing adaptive refinement and optimized fitting of data with anisotropic resolution by using robust scaled estimates. Subsequently, we demonstrated successful traction reconstruction regarding cells adhered to differently shapes substrate topographies.

- In chapter 3 we introduce a novel model-based approach to improve traction reconstruction on planar substrates. Here, we show that the combination of quantitative cell modeling allows to improve the resolution of reconstructed traction fields. Further, the model coupling allows to correlate local traction with intracellular structures of the actin-CSK. Thereby, we obtain as main result distinct

tension distributions for different SF types in agreement with their molecular assembly.

- In chapter 4 we simulated cellular contraction by means of thermoelastic continuum theory, where we considered collective contraction of cell monolayer colonies constrained to different geometries. We show that the simple model agrees well with the mean distribution of traction patterns obtained by standard traction force microscopy. Together with statistical analysis of cell morphology, the experimental and model results suggests that geometry and collective cell mechanics promote the formation of leader cells, which could be important for collective cell migration in, for example, wound healing of the skin. In a second study, we aimed at the topic of tumor metastasis, while we studied the effect of geometry and cell mechanics to promote tissue invasion. Here, we found optimal cell geometries dependent on substrate stiffness that favor environmental indentation, which is suggested to be the first step in tissue invasion by cancer cells.

2

Traction Force Microscopy on non-planar Substrates

2.1 Introduction

Substrate topography on the nm- and μm-scale alters cellular behavior regarding cell proliferation, polarization, migration, and function (61, 62, 63). For instance, cells usually align to given nano- and micro-topography, when they are cultivated on multiple groove substrates, e.g (64). Further, topography can guide polarity and growth direction of neurons (65). An interesting feature of cells is to adapt to provided substrate curvature (on μm-scale). It has been shown that cells adhered to cylindrical substrates align the actin-CSK along the cylinder axis (66) and dependent on the curvarture directional cell growth is affected (67). It is suggested that the intracellular distribution of CSK stress might allow cells to detect curvature in range of their own size (68). Recent studies consider μm-curved soft substrates using patterning techniques either with polyacrylamid (PAA) or polydimethylsiloxan (PDMS) gels (see review (69)). The application of soft non-planar substrates potentially allow quantitative measurements of forces by traction force microscopy (TFM). However, this has not been achieved up to now since standard TFM approaches are limited to planar substrates.

This chapter introduces a FEM-based method to determine cellular traction patterns on non-planar elastic substrates, like illustrated in fig. 2.1. Standard TFM methods on planar substrates consider exclusively shear traction stress, for which 2d substrate deformation measurements as sufficient to reconstruct traction forces, see introduction 1.4. Compared to that, traction reconstruction on non-planar substrates requires 3d deformation measurements. As a further fundamental difference, usually no analytic

Green's function exists, which however is utilized in standard techniques. Often therefore the half-space approximation is used, which provides a analytic Green's function, known under the term Boussinesq solution (34, 35), see introduction 1.4. Due to the lack of analytic solutions in the non-planar case, we utilize numeric methods to solve the inverse boundary value problem (inverse BVP) associated with traction reconstruction in 3d. The core of the method which will be described in the following, is efficient finite element method (FEM) embedded in a parallelized optimization framework.

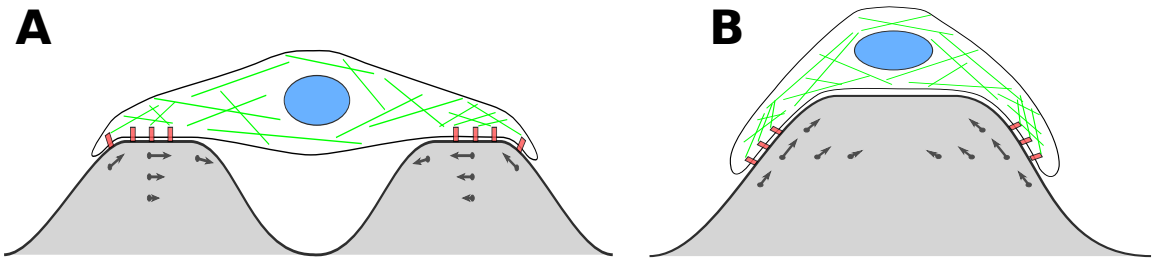

Figure 2.1: Illustrated situation of cells adhered to topographic elastic substrates. (A) Depicts the case of cell that spans a micrometer sized gap. (B) Depicts a cell covering a curved region on top of a wave. Black arrows indicate substrate displacements. Illustration details: actin CSK (green), FAs (red), and cell nucleus (blue).

TFM consists of a serial work flow of three essential stages: microscopy, image processing, and computational traction reconstruction. Errors in all parts of this work flow contribute to the absolute accuracy of determined traction patterns. Beside accurate characterization of the elastic properties of the substrate material, important issues are limited optical resolution in microscopy, varying marker bead densities, and miss matching of beads by the displacement tracking algorithm. Further model assumptions used by the reconstruction method limit the resolution, for instance, the assumption of infinite substrate thickness or the assumption of linear elastic theory. Interference of all these aspects render error estimations difficult for the achieved traction patterns. An implicit way yet to characterize the quality of the reconstruction process is to reconstruct data based on realistic simulations. This chapter provides a detailed method validation part based on such simulations, addressing the reliability of the proposed method. Here, we focus on different technical aspects, like local refinement of the FEM mesh, influence of experimental noise, and substrate topography. In addition, we analyzed the effect of outliers in the measured bead displacement fields. This leads to implications regarding the use of robust estimates in the reconstruction process. Finally, we demonstrate the application of the method to experimental data of cardiac

myofibroblast on wavy elastic substrates, for which we reconstruct traction patterns.

2.2 Method

As introduced in 1.4, the reconstruction of cellular traction from the deformation of elastic substrates is an inverse BVP. Traction reconstruction on topographic substrates proposed in this chapter consists of the different elementary parts: determination and meshing of substrate shape, calculation of the direct boundary value problem (direct BVP) by means of FEM, and solution of the inverse BVP by parallelized multidimensional parameter optimization. Fig. 2.2 illustrates the considered elastic problem (A) and the corresponding work flow to solve the inverse BVP (B). Here, we give a

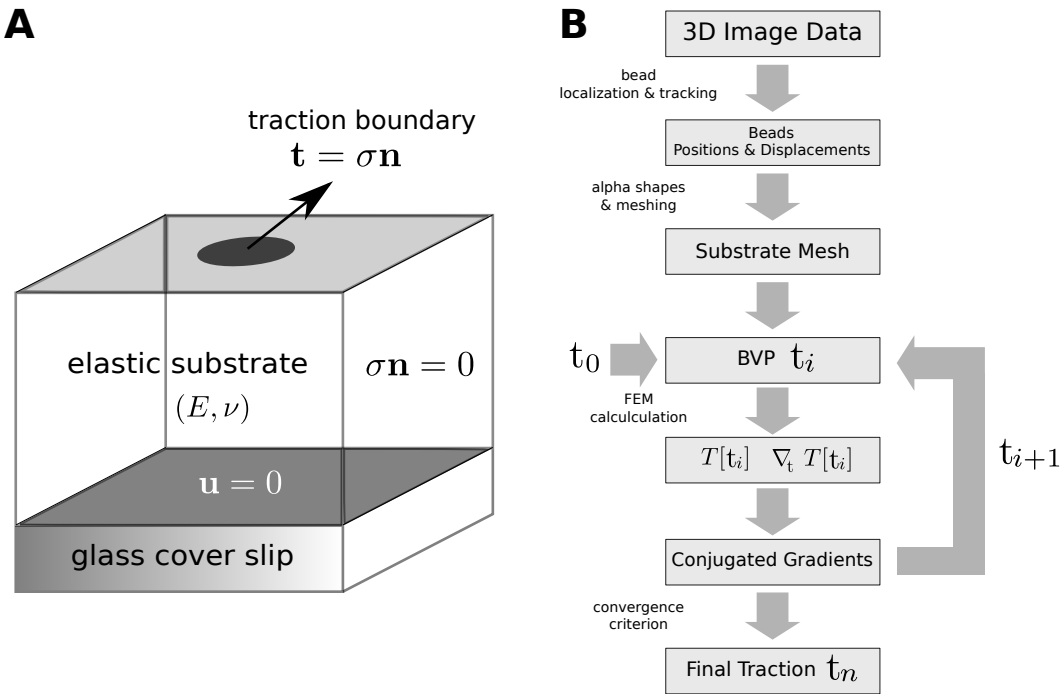

Figure 2.2: Illustration of the direct BVP and the work flow to solve the inverse problem. (A) Direct elastic BVP with mixed boundary conditions. The substrate elasticity is defined by Young's modulus E and Poison ratio ν. Boundary conditions: bottom - zero displacement ($\mathbf{u} = 0$), (sides) - zero-stress ($\sigma\mathbf{n} = 0$), top - traction field ($\mathbf{t}(\mathbf{x}) = \sigma\mathbf{n}$). (B) Method's work flow of traction reconstruction (inverse BVP). Starting from 3D image stack raw data several steps are processed: 3d bead tracking, substrate mesh generation, FEM calculations, and numeric traction optimization. Details and symbols are described in the main text.

brief overview on our work flow. At first, two fluorescence microscopy image stacks of marker bead distributions for the stressed and relaxed substrate state are correlated in

order to track the displacement of single beads in 3d. For the purpose of establishing a substrate model that agrees with the real substrate topography, we calculated the hull of the bead distribution in the relaxed state and transferred it into a mesh suitable for FEM calculations. After discretization of the direct BVP, multidimensional optimization of the Tikhonov functional was applied in order to optimize the traction boundary condition. Thereby, we started with an initial traction field $\mathbf{t}_0(\mathbf{x})$ and calculated the functional value and numeric gradients by multiple evaluations of the direct BVP for given traction configurations. In an iterative optimization process, we subsequently updated the traction field after each step i. We repeated the optimization steps until a desired convergence was achieved, for which the result represents the approximate solution of the inverse problem $\mathbf{t}(\mathbf{x})_n$. In the following, we will give a detailed description about the different implementation steps. This is divided into the separate parts of substrate shape determination and meshing, formulation of the direct BVP, description of the FEM discretization, definition of the inverse problem, and implementation of the optimization scheme.

Determination of Substrate Shape

Wavy substrates topographies were fabricated by collaboration partners (Nils Hersch & Nico Hampe, FZ Jülich) using micro molding techniques (70). This method leads to reproducible samples with micrometer accuracy. Unfortunately, shape variations and elastic material relaxation after mold removal affect the final shape. The effect of elastic relaxation can be captured mathematically as shown by Gordan et al. (71). However, in practice local shape variations in the provided data made theoretical considerations of expected substrate shapes unacceptable. We solved this problem by determining individual substrate shapes for each data set.

To determine substrate shapes, we developed a custom mesh generation program, which works as illustrated in fig. 2.3. Without using any additional experimental information, we utilized the measured distribution of bead displacements. This of course required sufficient high bead densities near to the surface region. The developed software tool based on C++ executes the following calculation steps. First bead locations are partitioned into sections along a chosen axis separated by a partition width w. In case of wavy substrates the optimal direction was tangential to the wave front. Afterwards bead positions are mapped to each section plane (normal pointing towards the partition direction), see 2.3 (A). By doing this, we end up with separated slices associated

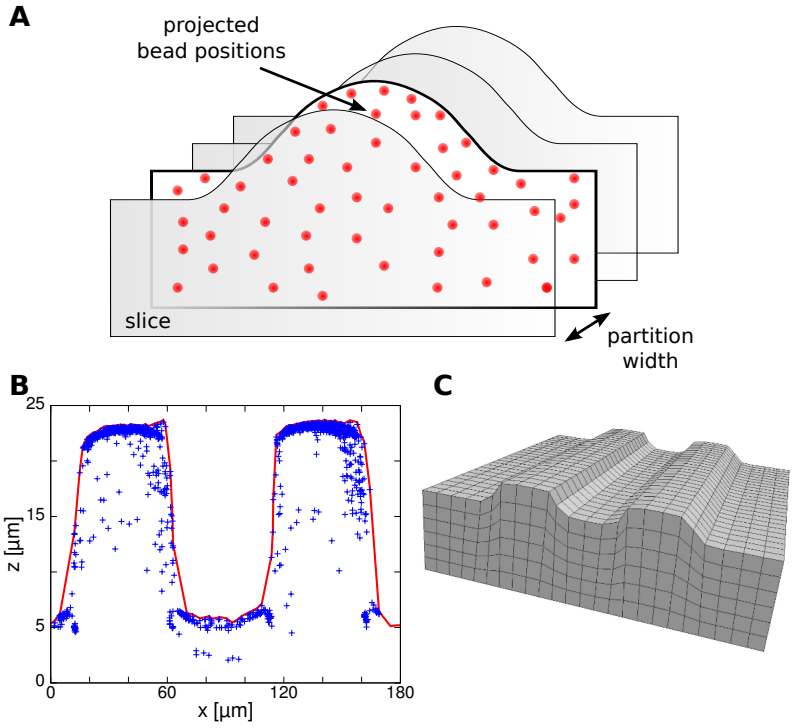

Figure 2.3: Reconstruction of substrate topography from bead positions - (A) Illustration of the computational procedure. The substrate contour get partitioned into volumes along a lateral axis. Bead displacements within the partitioned volumes get projected to boundary plane. (B) Subsequently the 2d α-shape algorithm is applied to projected bead positions (blue) in order to determine the envelope (red). (C) From multiple envelopes a 3d hexahedral substrate mesh is reconstructed.

with 2d bead distributions. Subsequently, we calculate the 2d hull for each bead distribution. For this purpose, we use the 2d α-shape algorithm (72), while utilizing an implementation provided by the open source computational geometry algorithm library (CGAL)(73). We have chosen α-shapes since it is not restricted to convex hulls, like for instance the quick hull algorithm. After hull determination for all segmented slices, the contours get stitched together along the chosen axis again separated by partition width w forming a 3d hexahedral substrate mesh. In this step the program uses the script interface of the open source mesh generator GMSH (74). An examplary result for the described procedure is depicted in fig. 2.3 (C).

Direct Elastic BVP

Traction reconstruction is established by solving an inverse elastic BVP. In the following, we define the corresponding elastic BVP considered for traction reconstruction. In this context we call it "direct BVP". The inversion of the direct BVP is in general

ill-posed, which implies that no unique or sufficiently stable solution exists. Both are strict requirements for well-posedness, see e.g.(49). In order to however find an approximated unique solution, we apply Tikhonov regularization. Here, we transfer the inversion problem to a minimization problem with respect to a so called generalized Tikhonov functional $T[\mathbf{t}(\mathbf{x}), \lambda]$. In case of traction reconstruction the functional depends on the traction field $\mathbf{t}(\mathbf{x})$ and a variable scalar regularization parameter λ (50). The calculation of this functional involves solving the direct BVP, which is in detail described in the following section.

For reasons discussed above, analytic solutions for elastic BVPs exist only in rare cases. Since this method is designed to deal with a variety of different substrate shapes, displacements $\mathbf{u}(\mathbf{x}; \mathbf{t}(\mathbf{x}))$ are solved numerically using finite element methods (FEM). Basically this allows us also to use nonlinear material models with variable strain energy density functions, which might become useful in cases of extremely soft substrates or apparently large deformations. For this purpose, our traction reconstruction also involves an implementation of a nearly incompressible Neo-Hookean material model. Unfortunately, due to highly enlarged computation times, up to now we were not able to reconstruct traction patterns with satisfying resolution. Regarding stiffness and geometry of the data described later, we expected sufficient small deformations within the limit of linear elasticity. In the following we formulate the direct BVP with respect to linear elasticity theory 1.3. This implies to solve the Navier-Lamé equation 1.31 with mixed boundary conditions:

$$\lambda\Delta\mathbf{u} + (\lambda+\mu)\nabla\nabla\cdot\mathbf{u} = 0 \quad on\ \Omega_0 \tag{2.1}$$

$$\mathbf{t} = \sigma\mathbf{n} \quad on\ \partial\Omega_{top} \tag{2.2}$$

$$\mathbf{u} = 0 \quad on\ \partial\Omega_{bottom} \tag{2.3}$$

$$\sigma\mathbf{n} = 0 \quad on\ \partial\Omega_{sides} \tag{2.4}$$

Traction exerted by cells is applied to the top surface $\partial\Omega_{top}$ of the substrate volume in the reference state Ω_0. Accordingly the traction field $\mathbf{t}(\mathbf{x})$ enters the equation system as stress boundary condition, $\mathbf{t}(\mathbf{x}) = \sigma(\mathbf{x})\mathbf{n}(\mathbf{x})$, where $\mathbf{n}$ is the normal vector of the unit surface element and $\sigma(\mathbf{x})$ the substrate Cauchy stress. Illustrated in fig 2.2 (A), we chose appropriate mixed BCs at the remaining parts arriving at a complete BVP. At the bottom surface we require zero displacement, $\mathbf{u}(\mathbf{x}) = 0$, due to rigidly substrate coupling to a underlying glass cover slip. Since the used mesh represents a cutout of the substrate, which is largely extended in lateral directions, proper boundary conditions at the side surfaces are applied. In case of an infinite half-space, right boundary condition

for the side surfaces of the cutout would be a counter stress of the same magnitude. This, in turn would lead to an undesired recursive problem, not feasible to compute it in acceptable times. Alternatively, we motivate zero stress boundary conditions, $\sigma\mathbf{n} = 0$, for sufficient large cutouts. Based on the knowledge that the displacement field monotonically decays with $1/r$ (34), the influence of boundary conditions can be neglected for sufficient large cutouts. Therefore, we occasionally extended the substrate mesh in lateral directions to ensure the repression of boundary effects. For given traction patterns $\mathbf{t}(\mathbf{x})$ the direct BVP is solved by means of FEM. The finite element discretization approach is described in the following.

Finite Element Method Implementation

Here, we introduce the FEM model for the numeric calculation of the linear elastic BVP , eq. 2.1 - 2.4. There exists a versatile literature regarding the finite element method and their application to elasticity theory. For an introduction into the mathematical background of FEM, we refer to the book of Braess (75). For a user-oriented introduction in FEM concentrating at elastic problems, we refer for instance to the books of Ameen (76) or Bonet and Wood (33).
In order to solve the BVP, we consider the principle of virtual work, which was already introduced in chapter 1.3. The principle of virtual work essential says, that an arbitrary external work applied to the elastic solid must be balanced by corresponding internal deformation work. Hence, we can write the work in case of linear elasticity as:

$$\int_\Omega (\delta\epsilon)^T : \sigma \; dV = \int_\Omega (\delta\mathbf{u})^T \mathbf{f} \; dV + \int_{\partial\Omega} (\delta\mathbf{u})^T \mathbf{t} \; dS. \tag{2.5}$$

$\delta\epsilon$ and $\delta\mathbf{u}$ are the variation of the linearized Green-Lagrange strain and the displacement. $\mathbf{f}$ and $\mathbf{t}$ represent external body and traction forces. Ω is the consider substrate volume in reference state (however in linear elasticity theory it is assumed that reference state $\approx$ current state). Since we are interested in solving the BVP without action of any body force $\mathbf{f} = 0$, we neglect the volume integral on the right hand side of the equation above up to now. We further use the linear stress-strain relation (eq. 1.28) to replace the Cauchy stress σ by its explicit expression with respect to the strain, obtaining

$$\int_\Omega (\delta\epsilon)^T : \mathrm{C} : \epsilon \; dV = \int_{\partial\Omega} (\delta\mathbf{u})^T \mathbf{t} \; dS. \tag{2.6}$$

The elasticity matrix C, here, is constant with a simple symmetric expression for isotropic elastic materials, eq. 1.29. By utilizing the strain-displacement relation of the linearized Green-Lagrange strain and the property that C is symmetric, we can rewrite the virtual work equation in terms of variations of the displacement and its derivative:

$$\int_{\Omega} (\nabla \delta \mathbf{u})^T : \mathrm{C} : \nabla \mathbf{u} \; dV = \int_{\partial\Omega} (\delta \mathbf{u})^T \mathbf{t} \; dS. \tag{2.7}$$

Note, this represents also the weak bilinear form of the Navier equation 2.1, when we consider the arbitrary displacement variation δu as a test function (multiplying eq. 2.1 with δu, integrating over the domain Ω, and subsequently applying partial integration). The following basic idea of FEM is to partition the domain Ω into smaller elements and to express the displacement field by an interpolation scheme. This has the objective to reduce the infinite dimensional space of displacement solutions to a finite dimensional subspace of nodal displacement values. The virtual work for a single element is given by:

$$\int_{\Omega^e} (\nabla \delta \mathbf{u}^e)^T : \mathrm{C} : \nabla \mathbf{u}^e \; dV = \int_{\partial\Omega^e} (\delta \mathbf{u}^e)^T \mathbf{t} \; dS. \tag{2.8}$$

In our calculations, we consider hexahedral elements with eight nodal points at element boundary. As an advantage of hexahedral elements, the volume and surface integration can be mapped to an integration over the unit cube parametrized by Cartesian coordinates, $(x_1, x_2, x_3) \rightarrow (\xi_1, \xi_2, \xi_3)$, while the coordinate transformation is determined by an individual Jacoby matrix calculated for each element. Thus the integration reads:

$$\int_{\tilde{\Omega}^e} (\nabla_{\xi} \delta \tilde{\mathbf{u}}^e)^T : \mathrm{C} : \nabla_{\xi} \tilde{\mathbf{u}}^e J_V \; d\tilde{V} = \int_{\partial\tilde{\Omega}^e} \delta \tilde{\mathbf{u}}^e \mathbf{t} J_S \; d\tilde{S}. \tag{2.9}$$

J represents the Jacobian and the tilde marks quantities with respect to the new coordinate $\boldsymbol{\xi}$. For subsequent interpolation of the displacement field we use interpolation functions $\Phi_n(\boldsymbol{\xi})$, which are based on an elementary set of linear shape functions. By interpolation of nodal values we can rewrite the displacement field, which now only dependents on a discrete number of degrees of freedom (DoFs) (hexahedral: number

of nodes multiplied by the dimension, $8 * 3 = 32$):

$$\tilde{\mathbf{u}}^e(\boldsymbol{\xi}) = N(\boldsymbol{\xi})\mathbf{u}^e_{node} = \begin{pmatrix} \Phi_1 & 0 & 0 & \dots & \Phi_n & 0 & 0 \\ 0 & \Phi_1 & 0 & \dots & 0 & \Phi_n & 0 \\ 0 & 0 & \Phi_1 & \dots & 0 & 0 & \Phi_n \end{pmatrix} \begin{pmatrix} u_1 \\ u_2 \\ u_3 \\ \vdots \\ u_n \end{pmatrix} \tag{2.10}$$

$\mathbf{u}^e_{node}$ is a vector of nodal displacement DoF values and $N(\boldsymbol{\xi})$ is the interpolation matrix, which interpolates the element displacement $\tilde{\mathbf{u}}^e(\boldsymbol{\xi})$ for a given configuration of nodal values $\mathbf{u}^e_{node}$. The same can be achieved for the virtual displacement $\delta\tilde{\mathbf{u}}^e(\boldsymbol{\xi}) = N(\boldsymbol{\xi})\delta\mathbf{u}^e_{node}$. Applying this to eq 2.9, we obtain

$$\delta\mathbf{u}^e_{node} \underbrace{\left[\int_\Omega (\nabla_\xi N(\boldsymbol{\xi}))^T : \mathrm{C} : \nabla_\xi N(\boldsymbol{\xi}) J_V \; d\tilde{V}\right]}_{K^e} \mathbf{u}^e_{node} = \delta\mathbf{u}^e_{node} \underbrace{\left[\int_{\partial\Omega^e} N(\boldsymbol{\xi})^T \mathbf{t} J_S \; dS\right]}_{\mathbf{R}^e} \tag{2.11}$$

K^e is called the element stiffness matrix and $\mathbf{R}^e$ the element load vector. Since $\delta\mathbf{u}^e_{node}$ is a vector of arbitrary values, we can reduce the problem to solving a linear algebraic system:

$$K^e\mathbf{u}^e_{node} = \mathbf{R}^e. \tag{2.12}$$

The components of the element stiffness matrix and the load vector are calculated numerically. Here, the integrals have been solved by means of Gauss quadrature. In this way we calculate the stiffness matrix and load vector for each element. In a subsequent step, we "assemble" a global system that forms the domain Ω:

$$K\mathbf{U}_{node} = \mathbf{R} \tag{2.13}$$

K, $\mathbf{R}$, and $\mathbf{U}_{node}$ are the global stiffness matrix, the global load vector, and the global DoF vector. Nodal DoFs are only shared by neighboring elements and thus K is a sparse matrix, while most of the matrix entries are zero. K is further singular and hence not invertible, since we have still not introduced constraints to avoid rigid body motions. Therefore, the system must be further restrained by incorporating appropriate BCs. For our direct BVP we consider the BCs, eq. 2.2-2.4, which are also illustrated in fig. 2.2. The traction BC enters the system through the surface integral in the load vector $\mathbf{R}$. The zero stress BC leads to no constraints of the system. Only the remaining zero

displacement BC applied to the bottom surfaces constrains eq. 2.13 and by forcing the displacement condition, we can reduce the system to

$$K_f \mathbf{U_{f,node}} = \mathbf{R_f} \tag{2.14}$$

where K_f is the reduced non-singular stiffness matrix, $\mathbf{U}_{f,node}$ is the global vector of unconstrained (free) DoFs, and $\mathbf{R_f}$ is the corresponding load vector. We solve the system with respect to $\mathbf{U}_{f,node}$ by using the conjugated gradient (CG) method. Alternatively, it is also possible to directly invert K by means of e.g. Gauss-elimination. In order to evaluate a displacement solutions at every position within the domain Ω, we apply interpolation via the introduced functions Φ_n with respect to obtained global DoF configuration $\mathbf{U}$.
For the implementation of the described FEM approach, we utilized the FEM C++ library *Deal.II* (77). It provides the essential set of features to achieve a FEM calculation, for instances, managing local and global DoF indices, Matrix manipulation feature, Gauss-quadrature, coordinate transformations, solvers for the linear algebraic system etc.. Now we will concentrate on the inversion of the described BVP.

Inverse Elastic BVP

According to Tikhonov and Arsenin (50), the inverse problems can be formulated as a minimization problem and in TFM the corresponding Tikhonov functional $T[\mathbf{t}(\mathbf{x}), \lambda]$ has the general form:

$$T[\mathbf{t}(\mathbf{x}'), \lambda] = L[\mathbf{u}(\mathbf{x}, \mathbf{t}(\mathbf{x}'))] + R[\mathbf{t}(\mathbf{x}', \lambda)] \tag{2.15}$$

Here, $\mathbf{x} \in \Omega_0$ and $\mathbf{x}' \in \partial\Omega_{top}$. $L[\mathbf{u}(\mathbf{x}, \mathbf{t}(\mathbf{x}'))]$ represents an error estimate that gives a value to difference between calculated and measured displacements. The larger the deviation, the larger is the scalar value the estimate returns. The second term $R[\mathbf{t}(\mathbf{x}')]$ is a penalty functional introduced to recover a well-posed solution (49).
We discretized the traction field $\mathbf{t}(\mathbf{x})$ according to the FEM mesh in order to set up a finite space of parameters. For this purpose, we use interpolation based on shape functions, introduced above. Hence, the entire field is characterized by a set of fixed point values t_i, with $i \in \{1...N_t\}$, which represent the degrees of freedom (DoFs) for the considered optimization problem. Since we use linear shape functions, fixed point values are associated with nodal positions on the top surface of the FEM mesh $\partial\Omega_{top}$. Thus, the total number of optimization parameters N_t is determined by the number of

surface mesh vertices N_v^{top}, and the number of space dimensions ($N_d = 3$), $N_t = 3{*}N_v^{top}$. The discretized version of the Tikhonov functional (eg. 2.15) then reads:

$$T[\mathbf{t}(\mathbf{x}')] = L(\mathbf{u}(\mathbf{x}, \{t_1, ..., t_{N_t}\})) + R(\{t_1, ..., t_{N_t}\}) \tag{2.16}$$

Up to now, standard TFM exclusively used least square estimates $L(\mathbf{u}(\mathbf{x}, \mathbf{t}(\mathbf{x}'))) = \sum_{i=1}^{N_{beads}} \|\mathbf{u}(\mathbf{x}, \mathbf{t}(\mathbf{x}')) - \mathbf{u}_i^{exp}\|^2$ to measure deviations between measured and computed displacements. Additionally, most methods use 0th order Tikhonov regularization $R[\mathbf{t}(\mathbf{x}')) = \lambda' \int_{\partial\Omega_{top}} \|\mathbf{t}(\mathbf{x}')\|^2 \, dA$, which corresponds to the squared norm of the traction field. This enforces a smooth traction solution by penalizing the amount of total force. This is the most simple approach to repress noise-induced fluctuations (46, 48, 52). By using this explicit expression, we write the Tikhonov functional as:

$$T[\{t_1, ..., t_{N_t}\}] = \sum_{i=1}^{N_{beads}} \|\mathbf{u}_{FEM}(\mathbf{x}_i; \{t_1, ..., t_{N_t}\}) - \mathbf{u}_{exp}(\mathbf{x}_i)\|^2 + \lambda \sum_{j=1}^{N_t} \|t_j\|^2 \tag{2.17}$$

From a statistical point of view, the least square estimator can be derived as the maximum likelihood estimate (MLE) for Gaussian distributed errors (78). This will be discussed later on, when we consider outliers in the data. The form written in eq. 2.18 implicitly assumes an isotropic error (same error distribution in all spatial directions). Especially for 3d displacement measurements this assumption is not satisfied anymore, due to a reduced resolution in z-direction of common microscopy setups. Therefore, we introduce a scaling vector $\mathbf{s}$ that weights the estimate contribution due to their relative accuracy. For instance, if $\sigma_{x,y} = 1$ is the standard deviation of the lateral noise and $\sigma_z = 3$ of the normal noise, $\mathbf{s} = (1, 1, \sigma_{x,y}/\sigma_z) = (1, 1, 1/3)$. Subsequently, we scale the estimate based on the known resolution anisotropy, achieving the functional:

$$T[\{t_1, ..., t_{N_t}\}] = \sum_{i=1}^{N_{beads}} \|\mathbf{s}(\mathbf{u}_{FEM}(\mathbf{x}_i; \{t_1, ..., t_{N_t}\}) - \mathbf{u}_{exp}(\mathbf{x}_i))\|^2 + \lambda \sum_{j=1}^{N_t} \|t_j\|^2 \tag{2.18}$$

In the following part of this chapter, we will pick up the issue of estimates describing alternatives to the standard least square measure.

Due to repeated time consuming FEM calculation of the direct BVP during minimization of the Tikhonov functional, efficient computation is a key issue in solving the inverse problem. The overall computation time depends in main parts on the number of traction DoFs N_t. Hence, a major objective was to achieve the best possible

local accuracy for a given number of DoFs N_t. In order to achieve this demand we used predefined mesh refinement and adaptive local mesh refinement (h-refinement). Mesh refinement is employed by dividing selectively volume elements into smaller elements, which effectively increases the density of DoFs. The idea behind it is to use local variations of the mesh size to concentrate DoFs at regions with higher levels of $\mathbf{t}$. Other region far away from the traction sources remain coarser at the same time. For the sake of completeness, we want to mention the alternative of local polynomial refinement, which describes local variation of the polynomial degree of used shape functions, called p-refinement. Also combinations of both refinement types in terms of hp-refinement schemes are conceivable. However, as h-refinement and p-refinement have similar effects to the local resolution, we here consider h-refinement only. In practice, the h-refinement in our program is done by an adaptive scheme. Based on reconstruction results on a coarser mesh, it is decided by global thresholding, whether an element gets refined. Afterwards the reconstruction process is restarted with the interpolated traction field obtained before. This process is repeated until a desired local resolution is achieved. Alternatively, we implemented also predefined local refinement based on thesholding of the measured displacement field. For the calculations in this work, we keep at local adaptive local mesh refinement schemes. The procedure tested in the validation part 2.3.1 by reconstruction of simulated data. As last part of this method section, we describe the multidimensional parameter optimization procedure, we use for minimizing a given Tikhonov functional.

Optimization Procedure

The core module of the FEM traction reconstruction program is the implemented multidimensional parameter optimization procedure based on the conjugated gradient (CG) method. The implementation follows essentially the Fletcher-Reeves variant of this algorithm as described in (79). Different from the book implementation, we parallelized most parts of the procedure, like the numeric gradient calculation $\nabla_t T[t_i]$ and the subsequent line minimization. Parallel computing was realized by using the Message Passing Interface (MPI), which is suitable for large scale distributed computing on computer clusters or sheared memory systems. Although the CG method is a common tool in the field of inverse problems, e.g. (80), we tested other optimization methods as well. Gradient-less downhill-simplex optimization, simple steepest descent, and heuristic Monte-Carlo optimization with simulated annealing (all described in (79)).

It turned out that by far the CG method led to the shortest computation times and excellent convergence.

2.3 Method Validation

We reconstructed simulated bead displacement data, for which we knew the original traction pattern. For this purpose, we introduced a simple cellular stress model, which is graphically summarized in fig. 2.4 (B). As the simplest form of cell shape, we considered a circular region as cellular area. In a ring shaped area of width d, we distributed randomly regions of accumulated traction stress, which we call "Traction Patch". The individual patch size is supposed to be variable. Like depicted in fig. 2.4 (A) by a typical reconstruction result with standard FTTC, the simulation procedure is motivated by the observation that traction spots often appear near to the cell edge. We further assume a constant traction stress distribution within a patch. According to experimental findings, we set a constant force density of $f = 3kPa$ in tangential directions (21, 23).

Previous studies (58, 81) reported appreciable cellular traction stress normal to the

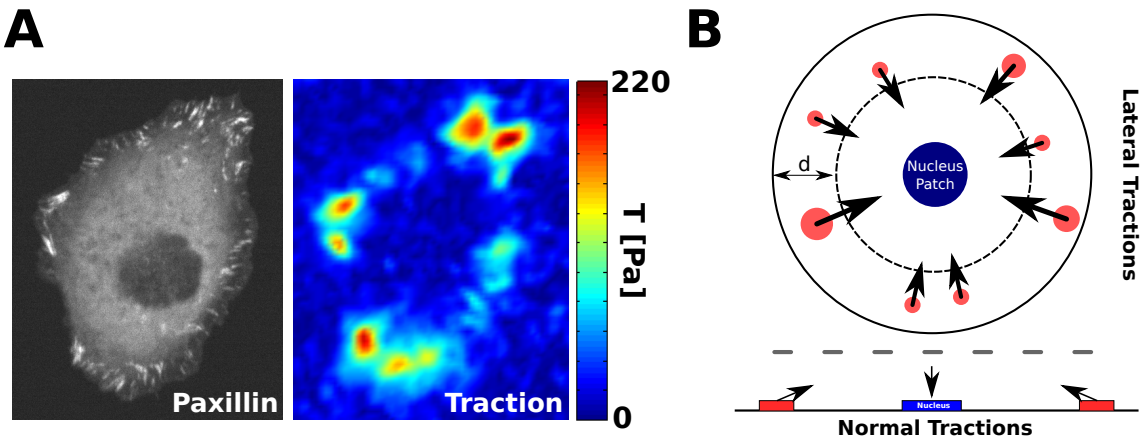

Figure 2.4: Simulation of traction patterns. (A) Experimental example: MDCK cell on $E = 8.4kPa$ PAA substrate. Paxillin fluorescence image and planar traction reconstruction result based in regularized FTTC (46), $\lambda = 1.2^{-5}$. Data from Gardel group, Institute for Biophysical Dynamics, University of Chicago, USA. (B) Illustration of traction pattern simulation. Traction patches (red circles) of random size are randomly distributed within a ring-shaped area near to the cell edge. Traction magnitude in lateral direction is set to a constant value of $3kPa$. Normal traction are randomly chosen and balanced by a nucleus patch (blue circle).

substrate surface. They found extractive deformations near to the cell edge and indentational deformations near to the cell center (compare fig. 1.9 (B)). A possible

explanation for this is contracting dorsal actin stress fibers (see classification in (82)), which connect the peripheral part of the cell to the nucleus. Hence, this suggests that indentational forces at the nucleus are counterbalanced by FA forces at the cell periphery. We picked this up and added random normal traction contributions for each traction patch. A subsequent force balance is reached by introducing an additional patch located at the cell's center acting as a "virtual nucleus". Altogether, this simple model allows us to generate realistic traction distributions that satisfy required balance of forces. After simulating traction fields with the described simple model, we calculate accordant substrate displacements by solving the direct BVP introduced above (eq. 2.1-2.4) with FEM. From the resulting displacement field, we sampled N_{bead} randomly distributed bead displacements. The evaluated numeric bead displacements are at this time only limited by the accuracy of the FEM calculation. In order to simulate the contribution of experimental noise, we introduced an additive displacement error $\mathbf{u}_{err}$, which modifies each displacement component by a random value chosen from a given statistical distribution. Thus the final simulated bead displacement becomes $\mathbf{u}_{bead} = \mathbf{u}_{FEM} + \mathbf{u}_{err}$. Subsequent reconstructions of the generated data allowed us to validate and characterize features of the proposed method.

2.3.1 Validation of adaptive Local h-Refinement

In order to increase local traction accuracy and to keep computation times feasible, we introduced the novel technical feature of adaptive local h-refinement. Since we employed adaptive local mesh refinement based on preceding calculations on coarser meshes, it may biases the resulting traction reconstruction compared to a calculation on a regular mesh. We addressed this concern and validated our adaptive h-refinement scheme by reconstructing traction fields from simulated data as described above. An exemplary simulated reconstruction is depicted in fig. 2.5. Here, we considered a traction pattern with three distinct traction patches of similar size and a nucleus patch located at the center of the simulated circular cell shape, fig. 2.5 (A). According to the simulation process, the direct BVP was solved for the given traction field (B) and a bead displacement field was sampled with respect to randomly chosen positions, see (C). In order to study the pure influence of applied adaptive h-refinement, we simulated without noise contribution ($\mathbf{u}_{err} = 0$) and focused on correct traction field reconstruction. Figs. 2.5 (D)+(E) depict a comparison of reconstruction results on a homogeneous and a adaptively refined mesh. For the adaptive reconstruction, we started with a two times larger mesh size compared to the homogeneous mesh. After

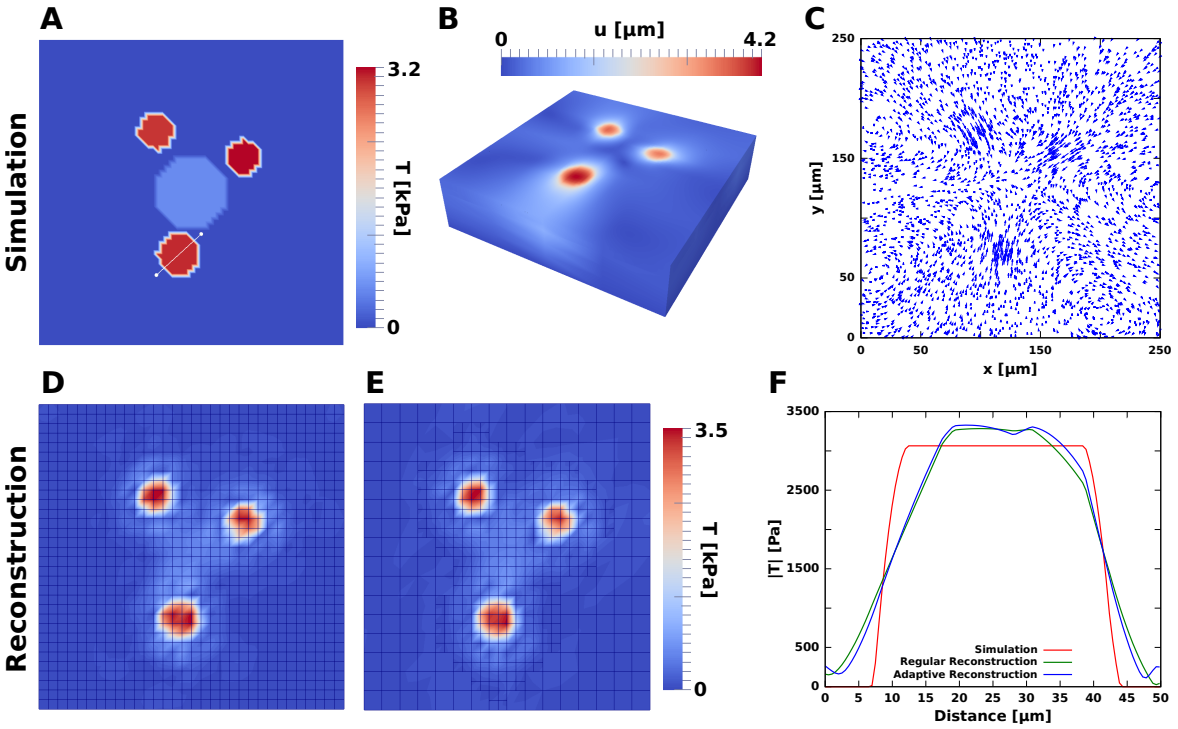

Figure 2.5: Local adaptive h-refinement in traction reconstruction. (A)-(C) Simulation of bead displacement field according to the procedure introduced in 2.3. Simulated bead density $n_{bead} = 0.048\frac{beads}{\mu m^2}$, which corresponds to a bead number of $N_{bead} = 3000$. (D) Reconstruced traction on regular mesh (3267 DoFs). (E) Reconstruction on locally h-refined mesh (1848 DoFs). (F) Comparison of simulation and reconstruction (D)+(E) along a traction profile through a force patch (white line in A)).

one refinement step, we subsequently achieved the same mesh size at refined regions, which made the results comparable. Both results show excellent agreement with each other and reconstruct well the original traction pattern. The depicted mesh topology shows the adaptive refinement automatically adjusted the local mesh size to regions of accumulated traction stress, while establishing the same accuracy as on the regular mesh. However, we saved 47% of DoFs by refinement. Although some parts of the benefit are diminished by the iterative nature of the adaptive refinement scheme. With increasing DoF number, however, the benefit dominates more and more. Fig. 2.5 (F) shows the traction profile through a reconstructed traction patch. Both reconstructions led to a slightly smoothed profile compared to the original profile. The problem of reduced resolution of sharp edge is explained by the resolution limit due to a limited bead density (in our simulation $n_{bead} = 0.048\frac{bead}{\mu m^2}$). Due to the sampling theorem by Nyquist and Shannon there exists a lower bound for the reconstruction accuracy. From the simulation results we conclude that adaptive local mesh refinement has less effect on the traction reconstruction accuracy, compared to a homogeneous mesh and is

appropriate for application in FEM-based TFM. We now examine the question, about noise sensitivity of the methods.

2.3.2 Effect of Experimental Noise

The stability of solutions of inverse problems and eventually the property of ill-posedness is highly affected by noise contributions in the provided data (49). This has been shown also for the concrete case of traction reconstruction (52). As mentioned in the introduction, observation uncertainties limit the resolution of the displacement field. The reasons are limited optical resolution of the underlying microscope images and mismatching of beads during the tracking process. The first issue can be treated as Gaussian shaped errors that limits the spatial localization of beads. The latter is less relevant in the planar 2d case since state of the art 2d tracking methods are very accurate with eventually negligible error rates. However, bead localization and tracking in 3d is by far more challenging, even with modern microscopy setups like laser scanning microscopes (LSM). This is due to anisotropic optical resolution resulting typically in a notably inferior accuracy in z-direction compared to the corresponding lateral directions. There exist improved setups like dual objective super resolution microscopy techniques (83, 84, 85), but they are not standard and rarely available. Further no application has been demonstrated up to now in TFM. Hence, one has to accept unfortunately a reduced resolution in z-direction. This is also the case for our study on experimental data described below. Therefore, our objectives were to improve bead tracking in 3d and to consider anisotropic optical resolution for the traction reconstruction process. Regarding the former, we struggled with a locally varying point spread function (PSF) due to surfaces topography, which effectively impeded the tracking with image cross-correlation techniques. Therefore, we applied more robust single bead tracking based on feature vectors as described in (55). The experimental image acquisition in 3d took over 30 min recording ≈ 100 stack slices. It turned out that this led to complex drifting effects, which further made adequate bead tracking difficult. To solve this problem, we applied drift correction for each individual slice, which successfully canceled the drift. Nevertheless, the derived displacement data showed anisotropic deviations and occasionally higher densities of outliers due to the challenging data processing.

To get a broader impression on the effect of different noise contributions, we simulated two different noise types: Gaussian distributed noise and mixed distributed noise established by a Gaussian and box-shaped distribution, which introduces data outliers. In order to quantify noise strength, we introduced the noise level as $n_{noise} = \sigma_{Gauss}/u_{max}$,

while σ_{Gauss} is the standard deviation of a Gaussian shaped error distribution and u_{max} is the maximal displacement in the noise-free original displacement field. Thus, we write the additive error as $\mathbf{u}_{err} = \boldsymbol{\chi}(\sigma_{Gauss})$, where $\boldsymbol{\chi}(\sigma_{Gauss})$ is a vector valued Gaussian distributed random variable. Separate choices of σ_{Gauss} for the vector components here allow to adjust the degree of resolution anisotropy.

Gaussian Noise

Fig 2.6 depicts an exemplary reconstruction for isotropic Gaussian noise with noise level $n = 0.2$. The corresponding noise-free reconstruction ($\mathbf{u}_{err} = 0$) was discussed before, see fig 2.5. Compared to the noise-free simulation the additional contribution of $\mathbf{u}_{err}$ led to fluctuations, when solving the inverse BVP without regularization ($\lambda = 0$), see (B). This is, however, an expected phenomenon explained in the general literature of inverse problems (50) and for the practical case of TFM (52). Accordingly, we utilized 0th order Tikhonov regularization ($R = \lambda\|\mathbf{t}\|^2$) to find an approximated reconstruction solution. Here, we determined an optimal regularization parameter by using generalized cross validation (GCV) (53). The optimal value of λ depends on the noise level and for the given example, we determined $\lambda = 1e{-}6$. The regularization improves the result significantly, which is depicted in fig. 2.6 (C). The penalization of total force induced by zero'th Tikhonov regularization, however, led to traction underestimation and edge smoothing. In order to avoid this and to further increase the accuracy, it is crucial to improve experimental conditions with enhanced microscopy like shown in a recent study by Plotnikov et al. (47). Beyond that we will come back to this issue, while we propose a novel regularization-free approach in chapter 3.

Mixed Distributed Noise

Next, we simulated the presence of outliers. Therefore, we draw the additive random displacement error $\mathbf{u}_{err}$ for each bead either from a Gaussian distribution $N(\sigma_{noise})$ or from a box-shaped distribution $H_i(w_i)$ limited by the box width w. We decided from which distribution an error contribution is drawn, by calculating an equally distributed random variable $\mathbb{X}$ over the interval $[0, 1]$. If $\mathbb{X} <= \epsilon$, we draw u_{err} from the boxed-shaped distribution, corresponding to an outlier. In case of $\mathbb{X} > \epsilon$, we calculated a Gaussian distribution u_{err}. Here, ϵ corresponds to the fraction of outliers.

Fig. 2.7 shows a comparison of simulated bead displacement fields for pure Gaussian noise, $n_{noise} = 10\%$, and with additional outlier contribution of $\epsilon = 0.3$. The width of the box-shaped distribution was set to $w = 10\mu m$. Qualitative inspection of the

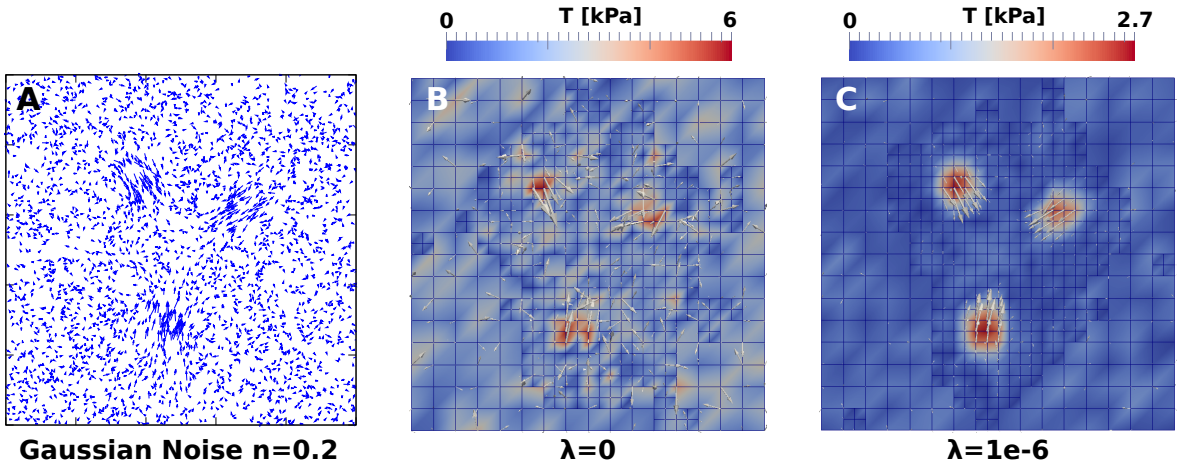

Figure 2.6: Effect of Gaussian noise and the need for regularization. (A) Simulated displacement field with additive Gaussian noise - fig. 2.5 (C) with $\mathbf{u}_{err} = \boldsymbol{\chi}(\sigma_{Gauss})$, while $\boldsymbol{\chi}(\sigma_{Gauss})$ is a Gaussian distributed random variable. The standard deviation of the Gauss distribution is set according to a noise level of 20%. (B) Reconstruction without regularization ($\lambda = 0$) leads to a noise dominated reconstruction. (C) Reconstruction with a regularization parameter $\lambda = 1e{-}6$, selected by GCV, recovers qualitatively the original traction pattern, however, with a reduced maximal traction magnitude of $\sim 11\%$ compared to the simulated pattern.

different displacement fields reveals a more chaotic displacement field with higher directional disorder. Basically there are two possible approaches to diminish the effect of outliers for the reconstruction. One is to filter out outliers based on certain criteria. This demands to set up appropriate filter limits. In our case, however, it is not desired to possibly throw away valid information in the data. The second approach is to use robust estimates for the optimization process. In the subsequent part, we will show that reconstruction can be improved, when the least square estimate in the Tikhonov functional gets replaced by a robust measure more insensitive against data outliers.
For this purpose, we use estimates based on the maximization of likelihood, called maximum likelihood estimates (MLE). The following brief derivation is according to the book of Maronna et al. (78), adapted to the problem of fitting a FEM solutions to an experimentally measured bead displacement fields. In this case the likelihood function is given by (for a single displacement vector component):

$$L(u_1^{exp}, ..., u_n^{exp}; u_1^{FEM}, ..., u_n^{FEM}) = \prod_{i=1}^{n} f(u_i^{exp} - u_i^{FEM}). \tag{2.19}$$

$f(u_{err})$ is the distribution function density of the additive error (note: $u_{exp} = u_{FEM} + u_{err}$). The maximum likelihood argument requires the maximization of this product

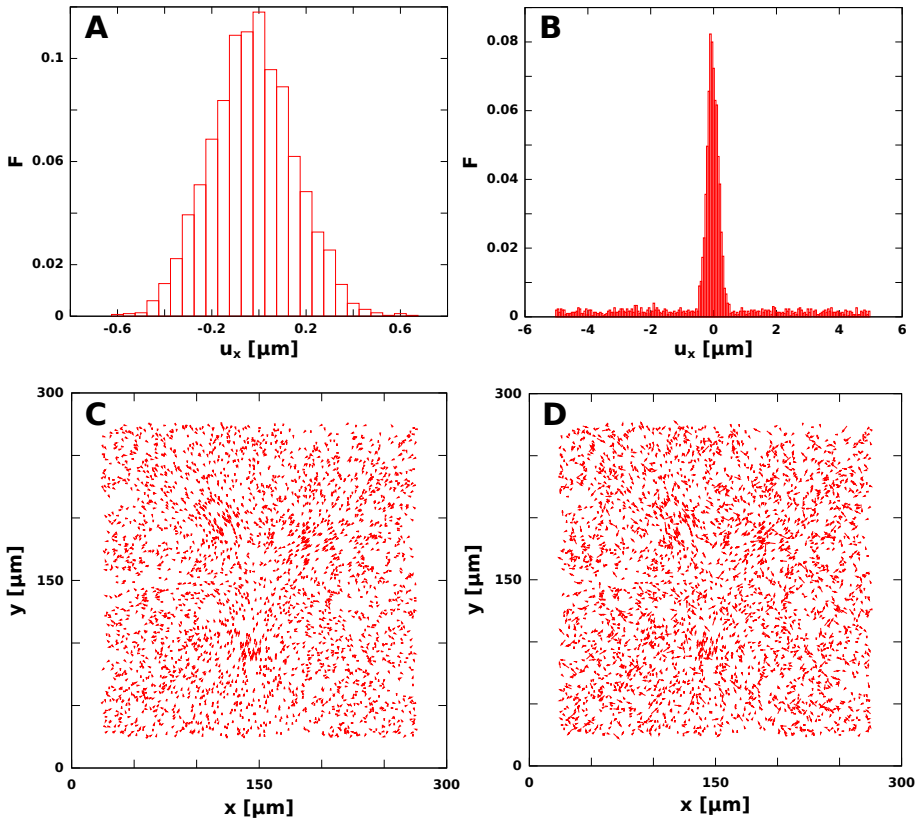

Figure 2.7: Simulation of outliers. Sampled error u_{err} in simulatd data: (A) From Normal distribution for $\epsilon = 0$ and $n_{noise} = 0.1$ (B) From mixed distribution with $\epsilon = 0.3$ and box width $w = 10\mu m$. (C)+(D) Corresponding displacement field projected to the xy-plane.

with respect to the FEM solution:

$$\max_{u_i^{FEM}} \left\{ L(u_1^{exp}, ..., u_n^{exp}; u_1^{FEM}, ..., u_n^{FEM}) \right\} \tag{2.20}$$

In case of a Gaussian shaped error distribution, the density function is represented by a Gaussian:

$$f(u_i^{exp} - u_i^{FEM}) = \frac{1}{\sqrt{2\pi}\sigma} \exp\left(-\frac{1}{2} \left(\frac{u_i^{exp} - u_i^{FEM}}{\sigma} \right)^2 \right) \tag{2.21}$$

f is everywhere non zero and positive, thus we can apply the standard trick of replacing f by its logarithm $\rho = -\log f$. Due to the sign change, we now search for a minimum instead of a maximum. In case of a Gaussian distribution the maximum likelihood

condition reads now:

$$\min_{u_i^{FEM}} \sum_{i=1}^{n} \left(u_i^{exp} - u_i^{FEM}\right)^2 / \sigma^2. \tag{2.22}$$

This is exactly the minimization condition of the L2 estimate. Comparing the equation above with the established term in the Tikhonov functional, eq. 2.18, we can correspondingly correlate the inverse of standard deviation σ for a given spatial direction with the components of the scaling vector $\mathbf{s}$ introduced above. In case of isotropic noise the scaling can be neglected. However, in the anisotropic case this kind of scaling is important. As we will see below, the quadratic dependence of the L2 estimator

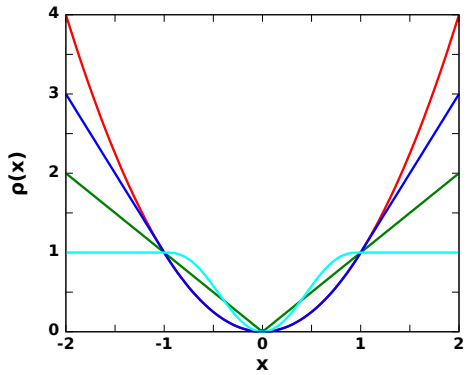

Figure 2.8: Comparison of different error estimates $\rho(x)$. Least square (L2) (red), L1 estimate (green), Huber function based estimate (blue), Biweighting function based estimate (turquoises). k=1.

caused problems during fitting of data perturbed by outliers, since their contributions get weighted quadratically. In order to diminish the effect of outliers, we propose the use of more robust estimates in TFM. Fig. 2.8 outlines different estimates (including the L2), which are all implemented in our FEM reconstruction program.

The simplest robust estimate is the L1, $\rho(x) = |x/\sigma|$, see fig. 2.8 - green curve. Same as the L2, it can be derived analytically from the maximum likelihood assumption based on a Laplace distribution $f(x) = \frac{1}{2\sigma} \exp\left(-|x|/\sigma\right)$. The essential advantage of this estimate is its weighting of deviations, which compared to the L2 damps outlier contributions. As alternative estimates, we implemented also Huber functions (blue curve) or Biweighting functions (turquoises), see Maronna et al. (78). They require an additional cutoff parameter k to characterize transition feature of the effective deviation weighting. This indeed needs a good guess about expected outlier strength and represents, for instance, in case of biweighting functions a filter, because contributions lager than k are completely neglected during optimization (see fig. 2.8 vertical part in

the turquoise curve).

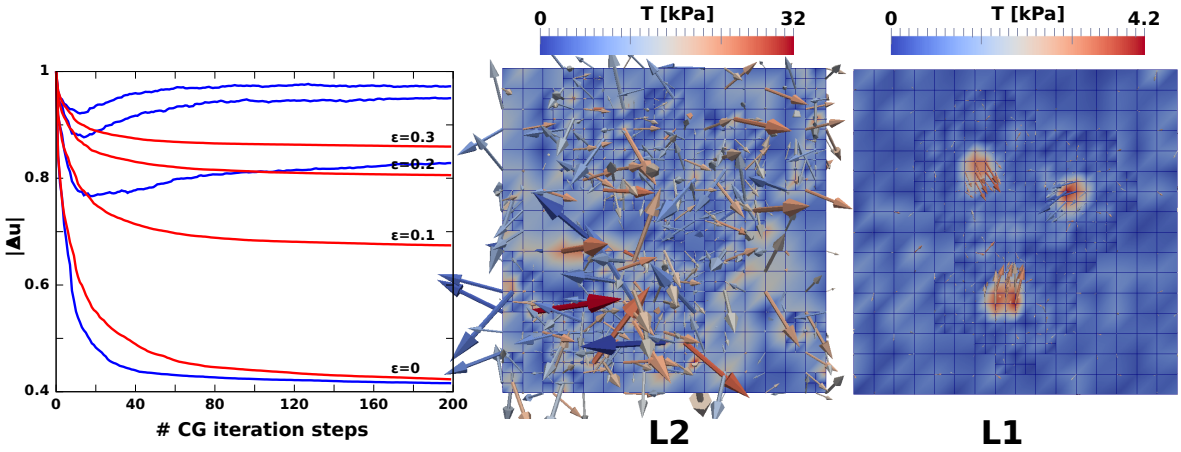

Figure 2.9: Reconstruction of data with mixed distributed error, including outliers. Left - mean relative deviation plotted over the number of optimization steps for different outlier fractions $\epsilon = 0, 0.1, 0.2, 0.3$ and for two different estimates, L2 (blue) and L1 (red). Middle - L2 based reconstruction result for outlier fraction $\epsilon = 0.3$. Right - L1 based reconstruction result for outlier fraction $\epsilon = 0.3$. For all simulation the Gaussian noise level was $n_{noise} = 0.1$.

Fig. 2.9 depicts the influence of the used estimate to the quality of the reconstructed traction field. The simulation study considered an isotropic Gaussian based noise of $n_{noise} = 0.1$ and a isotropic outlier distribution with $w = 10\mu m$. We investigated the convergence behavior for the optimization achieved by L2 and L1 estimate with respect the the outlier fractions $\epsilon = 0, 0.1, 0.2, 0.3$ (the data for $\epsilon = 0.3$ is depicted in fig. 2.7). To compare the results, we introduced the relative displacement deviation $|\Delta u| = \sum_{i=0}^{n} |u_i^{exp} - u_i^{FEM}|/|u_i^{exp}|$. For $\epsilon = 0$ (no outliers), both estimates converge to a similar result, however, the L1 converges slower (expected from the literature, see (78)). If we chose a non-zero fraction of outliers $\epsilon > 0$ the convergence dynamics of the optimization procedure starts to differ between L2 and L1. The L1 shows still a monotonic decreasing $|\Delta u|$, while in case of the L2 the curve starts to increase again saturating into a different solution. Corresponding traction field solutions for $\epsilon = 0.3$ are depicted in fig. 2.9. In case of using the L2, the reconstruction is strongly influenced by the fraction of outliers. Compared to that the reconstruction with the L1 led to satisfying results comparable with the simulated field. The simulation results show that not only a penalization term, but also robust estimates can improve the reconstruction of traction fields. This is especially relevant in case of 3d traction reconstruction, where challenging bead tracking increases the probability for outliers in bead displacement fields.

2.3.3 Comparison with Standard Traction Force Microscopy

Up to now, we considered only simulated data for which the material model perfectly matches the data. To demonstrate that the method works also for experimental data and that the result is comparable to state of the art TFM, we compared FTTC and FEM-based TFM for experimental data on planar substrates. Since the FEM approach considers a finite substrate thickness, we used a FTTC version that utilizes a Green's function for finite thick substrate layers introduced by Merkel et al. (54) (FTTC evaluation was carried out by Georg Dreissen, Merkel group, FZ Jülich, Germany). This represents an alternative to the most often used halfspace approximation (34). We reconstructed the traction field of a cardiac myofibroblast cultivated on a $E = 15\ kPa$ PDMS substrate with embedded single color marker beads. The bead displacements were tracked by image cross correlation (carried out by Georg Dreissen, Merkel group, FZ Jülich, Germany).

Fig. 2.10 depicts the reconstruction results. FEM-based TFM yielded adequately resolved traction features down to roughly $10\mu m$ (B). The adaptive mesh refinement automatically refined regions covered by the cell, depicted in (A). Unfortunately, we found no distinct traction contributions normal to the substrate surface larger than the surrounding noise. On the one hand this hints to an insufficient z-resolution, on the other hand also to too low z-traction magnitudes. However, for flatly shaped myofibroblast, we also expect small normal traction compared to those in lateral directions. According to optimal parameter selection, we derived an optimal regularization parameter of $\lambda = 1 * 10^{-5}$. A subsequent comparison with FTTC is depicted in (D) by an overlay of both solutions. The depicted vector plot allows to compare traction magnitudes ($\propto$ vector length) and direction. Both are in excellent agreement confirming the reliability of the method. Hence, as a last step of validation on planar substrates, we demonstrated successful application of our proposed method to experimental data with a resolution comparable with standard FTTC. We expect that the method's properties found on planar substrate are also valid on non-flat substrates. The validated technical aspects in term of refinement, regularization and impact of noise should be independent substrate geometry. Nevertheless, in a final step, we tested simulated traction reconstruction on topographic substrates.

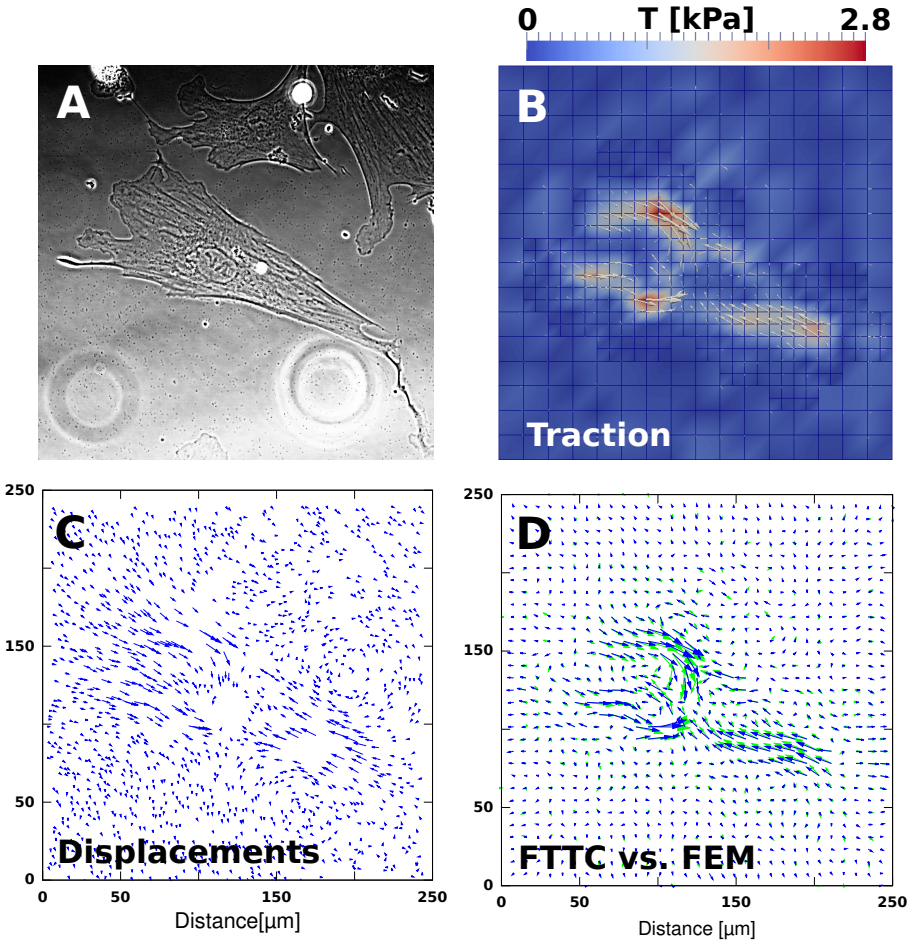

Figure 2.10: Comparison of FEM-based TFM and FTTC with experimental data on planar substrates. Here, we used a FTTC method that utilizes the Green's function for finite thick substrate (54). (A) Phase contrast: Cardiac Myofibroblast on planar $E = 15kPa$ PDMS substrate. (B) Reconstruction with FEM-based TFM using adaptive refinement (black mesh lines). (C) 3d displacement field projected to the xy-plane ($N = 1359$). (D) Comparison of both reconstruction results, FEMTFM (blue) and FTTC (green).

2.3.4 Simulated Reconstruction on Topographic Substrates

After a detailed method validation on planar substrates, we finally applied the method to simulated data considering a wavy substrate topography. We simulated traction patterns in a similar way as described for the planar case. Here, we adapted the simple cell model to the 3d case as illustrated in fig. 2.11. The considered sinusoidal substrate shape reflects the experimentally relevant case of cells adhered to a wavy substrate. In order to generate traction patterns, we first distributed random traction patches at both flanks of the sinusoidal shape, while the traction vectors point at a "virtual point". In a second step, all traction directions got reoriented due to movement of the virtual point in 3d, until a balance of overall force was achieved.

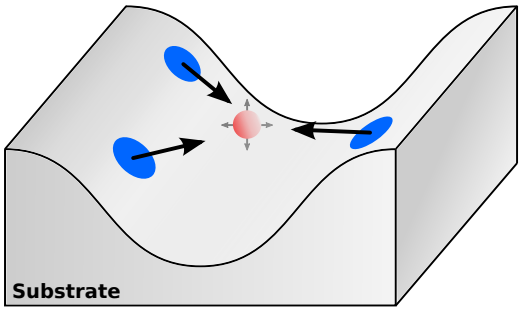

Figure 2.11: Traction field simulation mimicking a cell that spans two flanks of a sinusoidal wave. All forces point to a virtual point between the two wavefronts. After random generation of traction patches, the virtual point is moved in such a way that the force sum is zero.

Fig. 2.12 depict an exemplary simulation result. It shows a traction field with four distinct traction patches with force density $f = 3kPa$. The corresponding simulated bead displacements are depicted in fig. (B) and (C) in terms of projections to the xy-plane and xz-plane. Compared to the planar case, the displacements in z-direction became more prominent, see fig. 2.12 (C). The resulting reconstruction is as successful as for the planar case, compare fig. 2.12.

2.4 Results: TFM on non-flat Substrates

We applied the proposed traction reconstruction method for cells cultivated on different substrate topographies. As objective of this study, we wanted to investigate the influence of environmental topography on cellular contractility. Unfortunately, up to now only three data sets have been carried out from experiments (data from Merkel group, FZ Jülich, Germany). The limited data therefore allowed us to make only preliminary and qualitative statements. We expect, however, more data with improved resolution in the near future. Nevertheless, with the given data we could successfully demonstrate traction reconstruction on non-planar elastic substrates, for the first time to our knowledge.

In the experiment, cardiac myocytes were cultivated on non-planar PDMS substrates with Young's modulus $E = 15\ kPa$. Beads were distributed within the volume and on top of the non-planar substrate surface with separate bead colors. From the latter, we determined the substrate shape as described in the methods part 2.2.

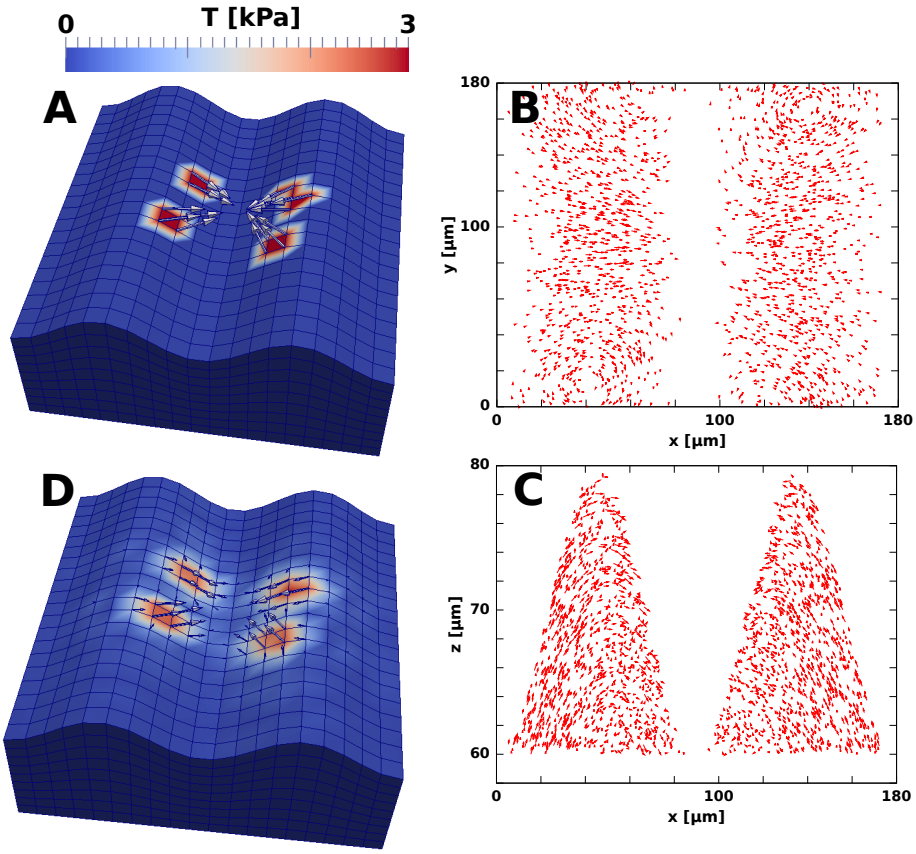

Figure 2.12: Traction reconstruction simulated on a sinusoidal substrate topography. (A) Simulated traction field with four traction patches $f = 3\ kPa$. Simulated displacement field with bead volume density $n^V_{bead} = 0.003 \frac{bead}{\mu m^3}$ ($N_{bead} = 2000$), (B) projected to the xy-plane, and (C) projected to the xz-plane. (D) Shows the achieved reconstruction.

Two different topographies were fabricated, micro-grooves and wave shapes. The detail fabrication process is not yet published (Waves: Nils Hersch et al. and Grooves: Nico Hampe et al., Merkel Group, FZ Jülich). For the reconstruction, we used the adaptive mesh refinement approach. We first calculated the traction solution on a coarser mesh ($\sim$ 50 optimization steps) and afterwards refined $\sim$ 40% of the cells at the surface based on obtained traction magnitudes. By doing this, we achieved a local mesh sizes of $d_m = 7/10/6\ \mu m$ for the corresponding cells A/B/C (see fig. 2.13). We further utilized a scales L1 estimate and zero'th order Tikhonov regularization (same regularization parameter for all data). The scaling vector was chosen in such a way that displacements in z-direction were weighted by 1/3, according to ~ 3 times poorer resolution in z-direction compared to lateral directions, $\mathbf{s} = (1, 1, 1/3)$. The results for the different data sets are depicted in fig. 2.13.

Cell A was adhered on top a slightly curved surface between two grooves (dimensions:

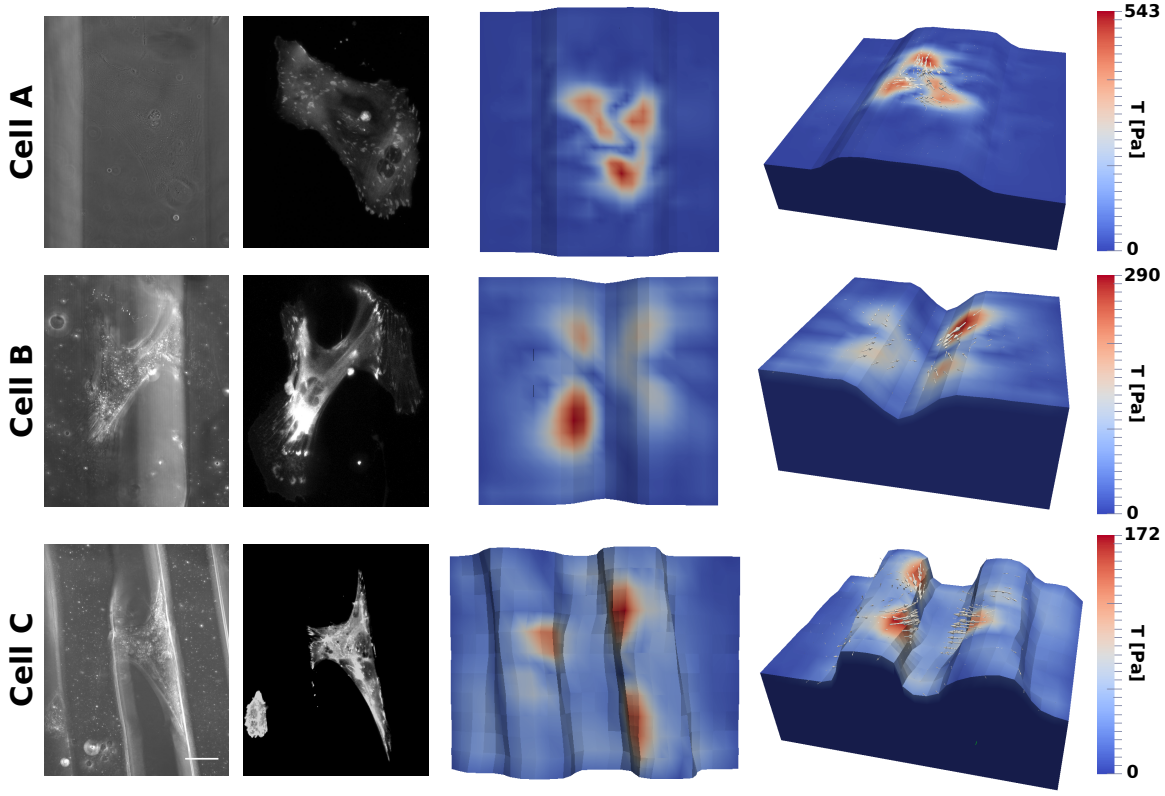

Figure 2.13: Traction reconstruction for cardiac fibroblasts cultivated on three different topographies. From left to right it is depicted: phase contrast image, VASP-GFP fluorescence image, top view and 3d view of reconstructed traction field. For the reconstruction, we used a scaled L1 estimate with scaling vector $\mathbf{s} = (1, 1, 1/3)$. Scale bar $50\mu m$.

$h = 25\ \mu m$, $w = 120\ \mu m$). Compared to the others it shows the largest spread area and a roughly homogeneous distribution of FAs (Vasodilator-stimulated phosphoprotein (VASP) fluorescence image). For this cell, we obtained also the largest maximal traction with $T_{max} = 543\ Pa$. Cell B occupied the edge region of two opposite groove flanks (groove dimensions: $h = 30\ \mu m$, $w = 70\mu m$). FAs were concentrated to limited region at the edge and the cell spanned the groove with actin SFs bridging free space. The maximal traction was $T_{max} = 290\ Pa$. The traction vectors revealed that most of the forces were balance along the edges and not to the opposite groove flanks. Cell C spanned the gap between two wave shaped hills (wave shape: $h = 30\mu m$, $w = 25\ \mu m$ with separation distance $d = 60\ \mu m$). FAs were more concentrated at vertical parts of the edge region with similar total area compared to Cell B. We derived the lowest maximal traction $T_{max} = 172\ Pa$ for this cell. But again as for Cell B most of the forces seemed to be balanced along the right wave instead of across the gap.

2.5 Summary & Discussion

We described a novel FEM-based approach to reconstruct cellular traction forces from measured deformation of soft elastic substrates. The method is based on a multidimensional parameter optimization process considering a discretized traction field. We take care for efficient calculation utilizing adaptive local refinement schemes and parallel computing. We further validated the model by reconstructing simulated data for planar and topographic substrates. Additionally, we could successfully crosscheck the method's results with standard FTTC reconstruction. The method is designed for full 3d traction reconstruction, which requires displacements of embedded marker particles in all three space dimensions. In case of standard confocal microscopy this goes along with a reduced optical resolution in z-direction and subsequently larger displacement errors and outliers. In order to improve the traction reconstruction by incorporating knowledge about the experimental deficiencies, we introduced robust estimates and directional weighting. We simulated different error contributions and demonstrated the reliability of the approach. As a consequence, we replaced for the reconstruction of our data the usual least square estimate by a scaled L1 estimate.
Subsequently, we applied the proposed method to experimental data of cardiac myocytes cultivated on elastic substrates modified micro-topographies. The objective of this was to investigate the impact of environmental topography to cellular contractility. Due to a currently low number of available data ($N = 3$), the study allowed us to make only qualitative statements. The results, nevertheless, hint to following preliminary conclusions. Cells on our soft topographic substrates seemed to be less contractile than on planar substrates. All three studied cells on topographic substrates (fig. 2.13) showed apparently less traction forces compared to these on planar substrates (e.g. see fig. 2.10). Typically cardiac myocytes on planar substrates exert high traction forces, up to several kPa. On topographic substrates we found up to now only magnitudes lower than 1 kPa. A possible explanation for this is a topography dependent lower effective substrate stiffness. Since it is known that cells adapt their traction forces to the stiffness of the environment (8), cell's may respond to an effectively softer environment with less traction stress. The traction results further suggest that cells which span micro grooves or wave shapes exert no increased traction forces in the "bridging" direction. Interestingly, most of the forces were balanced along the curved substrate regions parallel to the grooves or waves respectively. According to experiments mentioned in the introduction of this chapter, cell adhered to cylindrical substrates tend to orient their actin fibers along the main axis of curvature e.g. (66). This suggest also

increased traction stress along convex edge part of the considered substrate topographies. In summary our results hint to interesting cell behavior regarding their ability to adapt their contractility to the topographical features. They may provide a deeper understanding of the mechanical response of cells to topographic signals, with implications for to growing field of tissue engineering. In the future it would be interesting to extend the experiments to other cell types, especially cells that are known to live on micro sized topographies. For instance, podocytes live on strongly curved surface within the glomerulus of the kidney. The proposed method, here, would allow us to quantify cellular forces under natural geometric conditions.

3

Model-based Traction Force Microscopy

3.1 Introduction

Cells exert traction forces mainly via micrometer-sized cell-matrix contacts called focal adhesions (FAs). As described in the introduction (1.2), these kinds of contacts establish a stable connection to ligands in the ECM. The direct connection to the ligand is build up by transmembrane proteins of the integrin class (19). Via a hierarchical assembly (30) of over 150 different proteins that constitute mature FAs (20) a connection to the actin CSK is established, which allows to transmit intracellularly generated forces to the extracellular environment. As they are thought to play a essential role in mechanotransduction, FAs are of special interest (27, 86, 87, 88). There is evidence that defects either in the actin-CSK or within cell-matrix contacts cause different kinds of diseases with large socioeconomic influence including cancer (89). In order to understand the origin of these diseases on a detailed level it is a key issue to quantify cellular forces and to correlate them with individual FAs and intracellular structures of the actin-CSK such as SFs.

In this chapter we address the issue of improving traction force microscopy (TFM) to single FAs resolution. In contrast to the previous chapter, we are now focusing on planar elastic substrates. Standard traction reconstruction procedures, introduced in (1.4), are the starting point of our development. Typical for an inverse problem, traction reconstruction is very sensitive to experimental noise and limited bead density. Eventually, unique traction reconstruction is only possible using regularization schemes, which always introduce a priori assumptions about the considered system

(49). Typical traction reconstruction methods deal with 0th order Tikhonov regularization (e.g. (48, 52, 60)) assuming a sufficiently smooth traction field. The effect of this kind of regularization depends on the size of a variable regularization parameter λ, which controls the strength of regularization and effectively penalizes solutions with large total forces. Tikhonov regularization represses noise very effectively, however, it also affects reconstructed traction magnitudes, feature sizes, and positions of traction hot spots. For illustration, fig 3.1 shows a comparison of reconstruction results achieved by regularized FTTC (46). In order to compare the effect of regularization we used different regularization parameters λ. The reconstructed results show that with increasing regularization strength, the maximal traction decreases and an initially more speckled distribution of traction hot spots smooths out to few large remaining spots. It is a good practice to employ well-established parameter selection methods in order to find an optimal value for λ. Here, "Optimal" means a parameter value, sufficient large to repress noise contributions, but not too large to dump signal information. Among others, the two most popular methods are the L-curve criterion and generalized cross validation (GCV) (49, 53). Both methods optimize the regularization parameter in a general way, with respect to best noise repression. No additional information about the physical system is used here. Referring to the reconstruction example depicted in fig. 3.1, it is not entirely clear why the strength of experimental noise eventually should determine the feature size and distribution of traction via the determined regularization parameter.

Recent studies tried to assess single FAs forces with standard resolution FTTC by evaluating total tractions under ellipsoidal areas according to segmented FAs (90, 91). The evaluated traction patterns in these studies show apparently large spots that cover multiple neighboring FAs. Large traction hot spots may indicate either missing local displacement information or over-regularization (λ chosen too large). Consequently it is not verified that the local traction resolution is sufficient to assign unique traction values to single FAs. Plotnikov et al. (47) approached this issue by further increasing the experimental resolution achieving reconstruction of well-separated traction spot of the size of single FAs. For this purpose they increased the bead density significantly and resolved bead positions beyond the diffraction limit, using multiple bead colors ($>$ 2 colors). This improvement allowed them to track the force dynamics of single FAs over time with satisfying resolution. Another method to mention, is the application of so called molecular tension sensors, a technique developed by Grashoff et al. (92). The idea is to modify FA proteins like vinculin, which are supposed to be stretched during

force application. Using genetic engineering elastic peptide chains are added to the protein body and decorated with FRET donor and acceptor proteins on both ends. FRET is an abbreviation for Förster resonance energy transfer that describes an non-optical energy transfer between donor and acceptor fuorophores. The energy transfer depends on the distance between both proteins and the ratio of both fluorophores emissions allow the determine a distance between both ends of the peptide chain. Hence, the FRET signal indicates the strength of protein stretch and with preceding calibration measurements local tension values can be determined. These type of experiments lead to speckled fields of micron sized tension hot spots. Unfortunately, both mentioned high resolution methods are experimentally challenging, which makes their application to quantitative studies difficult.

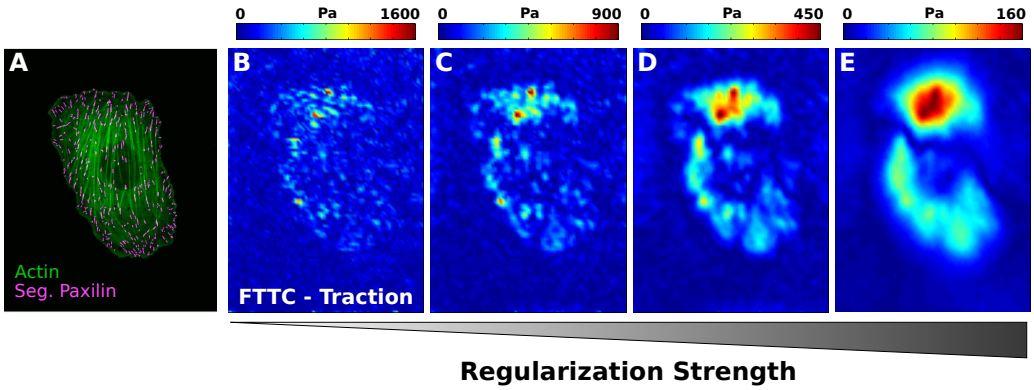

Figure 3.1: FTTC reconstruction applied for a U2OS cell on $E = 8.4kPa$ Polyacrylamite substrate. (A) Overlay fluorescence image of actin and segmented paxillin (FA protein). (B) to (E) FTTC reconstruction according to (46) using zero'th order Tikhonov regularization. The regularization parameter λ over several order of magnitudes $\lambda = 0, 5 * 10^{-6}, 5 * 10^{-5}, 5 * 10^{-4}$, increasing from (B) to (E). While the noise gets increasingly repressed with stronger regularization also the traction magnitude (see color bar limits) and typical feature sizes, number, and location changes. The total force accordingly decreases with increased traction $T = 596, 422, 298, 160\ nN$ according to the simulated λ values.

In this chapter, we describe a novel model-based traction reconstruction approach, which we call model-based TFM (MB-TFM). This technique allows us to overcome the need for Tikhonov regularization and improves the resolution down to the level of single FAs although using TFM with standard resolution. The basic idea behind this method is to invert the concept of evaluating ellipsoidal areas by incorporating the information about the distribution and shape of FAs into the reconstruction process. This extends basically the point force approach by Schwarz et al. (52), where points forces are distributed to positions of FAs. In addition to this constraint, a quantitative

model for cellular contractility is incorporated involving structural information about the actin CSK. For a particular model implementation, we show that the combination of both aspects allows us to reconstruct unique traction fields without requiring Tikhonov regularization. From a mathematical point of view, we state that the simple smooth traction field assumption behind Tikhonov regularization is here replaced by a non-trivial regularization scheme represented by a quantitative cell model. As the method's benefit, we demonstrate unique reconstruction of forces at single FAs and estimation of intracellular tension, which is not directly accessible in experiments.
In the following a detailed method description is given. Like for the FEM approach in chapter 2, we present a method validation based on simulated data and compare the results with standard FTTC. Subsequent method application to experimental data for U2OS cell demonstrates a detailed quantitative analysis of traction forces on the length scale of single cells and FAs. As most distinguished result, we estimated the tension distribution of different SF types with important implications how cells control their contractility.

3.2 Method

3.2.1 Overview

MB-TFM as a general concept is based on using secondary experimental information about the biophysical system in addition to measured substrate displacements to reconstruct cellular traction patterns. After problem discretization usual traction reconstruction consists of finding an optimal configuration in a finite space of typically $10k$ nodal traction values. In MB-TFM, this parameter space is further reduced by typically two orders of magnitude to a space of cell model parameters (≈ 100), which guarantees that obtained traction solutions satisfy biophysical constraints. This involves e.g. a mechanical model for intracellular stress propagation or the balance of forces required for closed systems. In order to gain solutions for the inverse elastic problem, the model parameters are directly optimized towards a best agreement of measured bead displacements. This kind of modified reconstruction has two advantages compared to standard TFM methods. First, it allows to overcome resolution limits given by bead density and experimental noise. Secondly, the reduction of parameter space dimensionality eventually makes the inverse problem well-posed for the case of appropriate cell modeling. To achieve the latter mentioned benefit, on the one hand the cell model must provide a certain level of detail in order to describe complex

traction patterns, on the other hand the number of model parameter should be small enough to avoid ambiguous solutions. The model quality can be checked in different ways. One can qualitatively cross check results by comparison with standard TFM or with models with reduced level of detail. Therefore one can compare the final L2 estimator value in any case, which indicates the agreement with the experimental data.

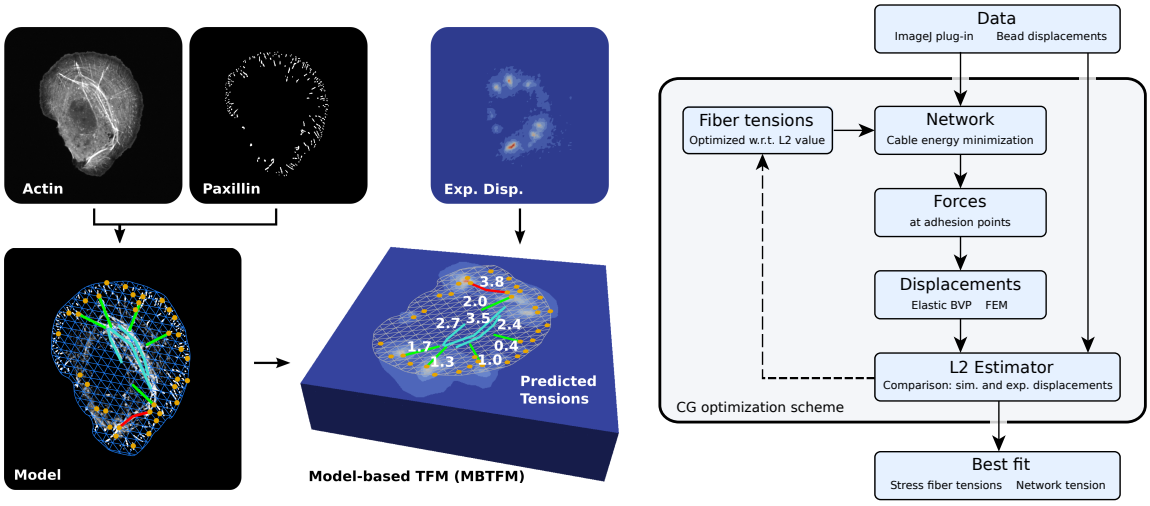

Figure 3.2: MBTFM with active cable model. From actin and paxillin fluorescence images SFs and FAs are segmented. Subsequently, a network model is generated incorporating the segmented data. In order to optimize model tension parameters the conjugated gradient is applied with requires iterative application of network contraction, force determination at FAs, calculation of resulting substrate model displacement and comparison with experimental data. The result is a configuration of cellular tension that fits best to experimentally measured substrate displacements.

In this chapter, we propose the application of active cable networks in MB-TFM. Here, cellular contraction is described by a two dimensional network of cables under active contractile tension. This kind of model has been successfully used to describe cell shapes of adherent cells and it is suggested to match mechanical properties of cells in a two-dimensional limit (93, 94). Fig. 3.2 gives an illustrative view on the concrete MB-TFM work flow. In our implementation we use experimental information about the distribution of FAs and actin SFs. For this purpose, we apply image data pre-processing with a self-written *ImageJ*-plugin. As a result of this process, we define a mechanical network that incorporates the collected data. In a next step, we used multidimensional optimization to find a solution for the inverse problem. This again requires repeated calculation of the corresponding direct problem like described in chapter 2. In case of MB-TFM with active cables the direct problem is to calculate substrate displacement fields for a given configuration of active cable tension parameters. This is done in the

following way: For a given distribution of network and SF tension (parameter configuration) the energy of the cable network is minimized (network contraction), while FAs considered as fixed points stabilize the solution. Afterwards resulting forces at FAs are read out and applied to a finite element substrate model that solves the elastic BVP. By doing this we transfer resulting network forces determined at FA positions into a model substrate displacement field. The solution of the direct problem is subsequently compared with measured bead displacements. For this purpose we calculate the fitness using the L2 estimate, which has been already introduced in chapter 2. The corresponding scalar fitness $T[t_i]$ is optimized by means of a modified conjugated gradient (CG) method (described later) in order to find a best fitting intracellular tension distribution fitting to measured substrate displacements.

3.2.2 Image Processing and Network Generation

We developed an "easy-to-use" plugin for the open source image processing program *ImageJ* (95), that provides all necessary features and which we called **S**egmentation **o**f **F**ocal **A**dhesions and **St**ress fibers plugin (So-FASt plugin). This includes SF segmentation and classification based on actin fluorescence images, FA segmentation and shape fitting based on paxillin (FA protein) images, segmentation of cell shape and network generation. The combined data is saved in a *Visualization Toolkit* (VTK) mesh file format (96) ready for use with the MB-TFM optimization tool.

FA Segmentation and Ellipse Fitting - The distribution and shape of FAs were segmented from paxillin fluorescence images. Local varying background and signal intensities impeded to segment FAs with global thresholding techniques. Therefore we accomplished this task by a serial work flow of local thresholding, background subtraction, and despeckling algorithms. The *ImageJ* plugin therefore utilizes several build-in functions of *ImageJ*, while image processing parameters can be interactively changed in order to achieve optimal results. After proper segmentation of the FA distribution, individual FAs are identified by a particle analysis algorithm and automatically fitted with ellipses saving FA position, area, orientation, and eccentricity.

SF Segmentation and Classification - The *ImageJ* plugin provides an interactive selection tool to segment and classify SFs following the classifications proposed by Hotulainen and Lappalainen (82). The user marks SFs as region of interest (ROI) and by switching the background between actin and segmented FA, image classification of SFs into dorsal SFs (DSF), transverse arcs (TA), and ventral SFs (VSF) is optimally

supported. In practice we classified SFs in the following way: SFs connected to a FA at one end have been classified as DSFs, SFs connected at both ends as VSFs, and SFs which are apparently not connected to any FA have been classified as TAs. In most cases this requirements were sufficient to uniquely classify a SF, otherwise requirements like orientation and relative position within the cell have been checked.

Network Generation - Triangular networks were generated based on segmented cell areas. In order to manage the introduction of SFs into the model network we established an adapted version of the distmesh algorithm (97). In detail this worked as follows: First vertices and links along segmented SFs were created. Afterwards, the remaining area was filled with a triangular grid embedding the SF links. In order to gain a nearly constant mesh size and homogeneous network contraction the network is homogenized according to the dist mesh algorithm. Here, network links are considered as compressed springs and network vertices are not allowed to leave the segmented cell area. To preserve the segmented actin structure SF vertices are held fixed. Mechanical equilibrium of the network results in a nearly homogeneous network with only small local variations. After the network was generated vertices close to FAs and links associated with segmented SF have been flagged accessible for the optimization tool.

3.2.3 Cell Contraction Network Model

Cellular contraction was modeled by an active cable model (ACM). This model combines the mechanical properties of passive cables and active force generation (93, 94). Compared to a spring, a cable shows no resistance to compression while following Hooke's law for extension. The model is appropriate for actin bundles, which show little resistance to compression. This has essentially three reasons: (1) they tend to buckle under small compression forces, (2) they show telescopic sliding due to motor activity and (3) they locally depolymerize if tension is relieved (88, 98). The resistance to tensile forces mainly reflects the elastic properties of crosslinkers in the bundle like α-actinin and non muscular myosin II. Active force generation is modeled by introducing force dipoles into the model, which corresponds to distributed action of myosin II minifilaments. By using static force dipoles, we assume that the minifilaments work in the stall regime of myosin II motors (velocity $v = 0$). Active cables have been used successfully to reproduce arc-like shapes of cells on micropatterned substrates (93) robust with respect to network topography (94). It has been shown as well that this type of model can predict traction forces on patterned substrates (99).
Embedding SFs into an active cable network has been introduced by Guthardt Torres

in his PhD thesis (100). In our version of this model, every link represents either a part of the background actin network (AN) or of an individual SF. In order to allow diverse anisotropic contraction modes, individual tension values t^{AN} and t_i^{SF} can be assigned to the AN and each of the N segmented SFs, $i = 0...N$. These tension values also represent the model parameters for the optimization process described later. For a given set of tension values the network is contracted by minimizing its total energy. Therefore, we use a conjugated gradient method like described in (79). A special feature of the active cable model is its stability properties. Without a fixed boundary condition, an active cable model is unstable since the state of minimized energy is a network collapsed to a single point following the special cable property regarding the missing network stress response against compression. Fixed boundary condition provide that elastic energy is build up during contraction due to links that switch in the extension regime counterbalancing the applied contractile tension. In our model vertices flagged as FAs are held fixed whereas all other vertices are free to move until force balance is reached.

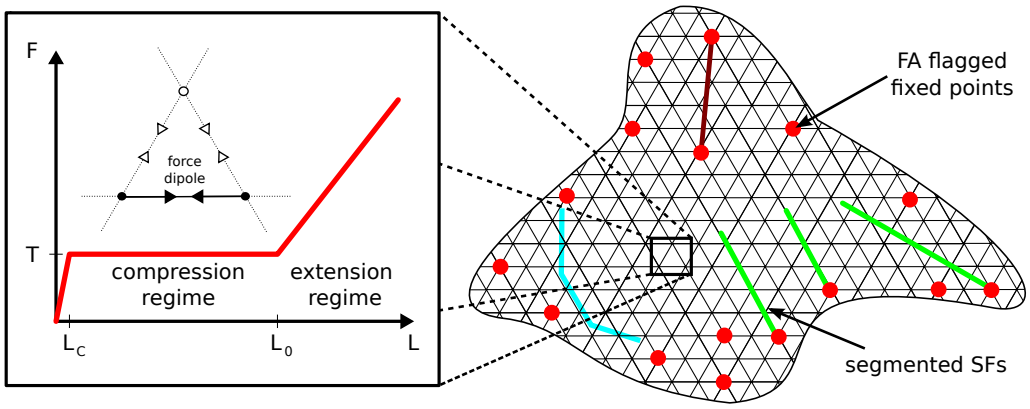

Figure 3.3: Active cable model (ACM) with embedded SFs and FA flagged fixed points. Red points mark fixed vertices located close to segmented FAs. Colored lines indicate segmented SFs of different type. Inset: force extension relationship of an active cable link. The modeled force dipole represents a tension plateau until a critical length l_c in the compression regime. In extension regime the links satisfies like a spring Hooke's law.

It is important to note that we only care for the distribution of tension within the network and not its elastic properties. In principle, a 1d modulus of $EA = 50\ nN$ is assigned to each link. However, we consider a strongly contracting network, most links will be in the compression regime (see inset of fig 3.3) and thus the link modulus has no large impact due to the intracellular tension distribution. Some few links will be under tension predominantly those at free parts of the cell periphery. Consequently the elastic modulus essential effects the resulting cell shape after contraction. In order to focus on

the reconstruction of cellular tensions we disregarded more complicated dynamically effects of the system like e.g. viscoelastic properties of SFs (101) or retrograde actin flow (102, 103).

3.2.4 Substrate Model

We calculated substrate displacements from network forces by coupling the ACM to a finite element (FEM) substrate model. For this purpose we run the same calculation like in chapter 2.2. We solve the direct BVP for linear elasticity according to eq. 2.1-2.4 (31, 77). Though instead of variable traction boundary condition, we determined traction fields from the cell network model. Therefore, we read-out resulting forces at vertices flagged as FAs and distributed the force homogeneously over correspondingly segmented ellipsoidal FA shapes. In order to properly interpolate FA traction despite their small size, which is 2 orders of magnitude smaller than the considered substrate sample size, we use again local mesh refinement. Compared to the topographic reconstruction case, the details of the traction field are known due to segmented FAs. Therefore, instead of using an adaptive refinement scheme, we directly refined regions coinciding with segmented FAs. We did this in such a way that at least 4 elements cover each FA shape. After subsequent calculation of the corresponding BVP we achieve a 3d displacement field. In practice, we omitted the z-component in order to compare with experimental data only available in both lateral directions.

3.2.5 Tension Optimization

Starting with all tension parameters set to zero, tensions of SF links and the AN were optimized to achieve an optimal agreement of simulated and experimental displacement field. As distance measure for deviations, we use the least square estimator defined in chapter 2.2. Compared to standard TFM (43, 46, 51, 52) a new feature of the MB-TFM implementation is that the model constrictions makes Tikhonov regularization dispensable (see below). Our method only allows forces at fixed positions distributed over a segmented FA shapes. This represents a kind of template for possible traction patterns. The remaining undetermined DoFs of the system are force magnitude and directions. The active cable model provides a meaningful force distribution according to a known structure of the actin CSK. In addition the cell model guarantees global force balance, which is a required constraint for closed systems (in absence of external forces).

In order to fit model parameters to a given measured displacement field we minimized the least square estimator with a modified version of the iterative conjugated gradient method described in (79). Here, each iteration step involves multiple calculations of cellular network forces and FEM substrate deformations for different tension configurations. As this is expensive in terms of computation time, we parallelized large parts of the numerical work using multi-threading. For this purpose, we utilized the multi-threading feature provided by the open source library boost (104). Due to the definition of our active cable network, changes in AN tension t^{AN} affect the traction force distribution in a global manner, whereas changes in individual SF tensions t_i^{SF} affect displacements more locally. The latter can be understood from the properties of an active cable network, which does not propagate stresses over large distances due to the lack of compression induced stresses. The different nature of DoFs lead to slow or no convergence of values when optimization is performed on both at once. Our modification of the usual conjugated gradient consists of a separate optimization of tensions t^{AN} and t_i^{SF} one after the other in terms of iterative blocks. For completeness we want to remark that an alternative would be appropriate parameter rescaling regarding the optimization in order to prevent slow or failing convergence. However, this has not been tested here. The different convergence behavior of conjugated gradient and modified conjugated as proposed here are further discussed in the validation part below.

3.3 Method Validation with Simulations

Similar to chapter 2, we validated and characterized the implemented MB-TFM method by reconstructing simulated data. Therefore displacement fields have been calculated based on test cell segmentations for known model tension configuration, see fig. 3.4 (A). For these simulations we kept the network tension constant $t_{AN} = 0.06\ nN$. Individual SF tensions t_i^{SF} were drawn randomly from an interval $[0, 10]\ nN$. After network equilibration for the given parameter configuration $N = 10000$ displacements (typical bead density) have been evaluated by interpolating the FEM solution at random positions on top of the model substrate surface, illustrated in 3.4 (B). The purpose of the validation was to verify unique traction reconstruction by the optimization procedure and to investigate the method's sensitivity against experimental noise and SF segmentation errors.

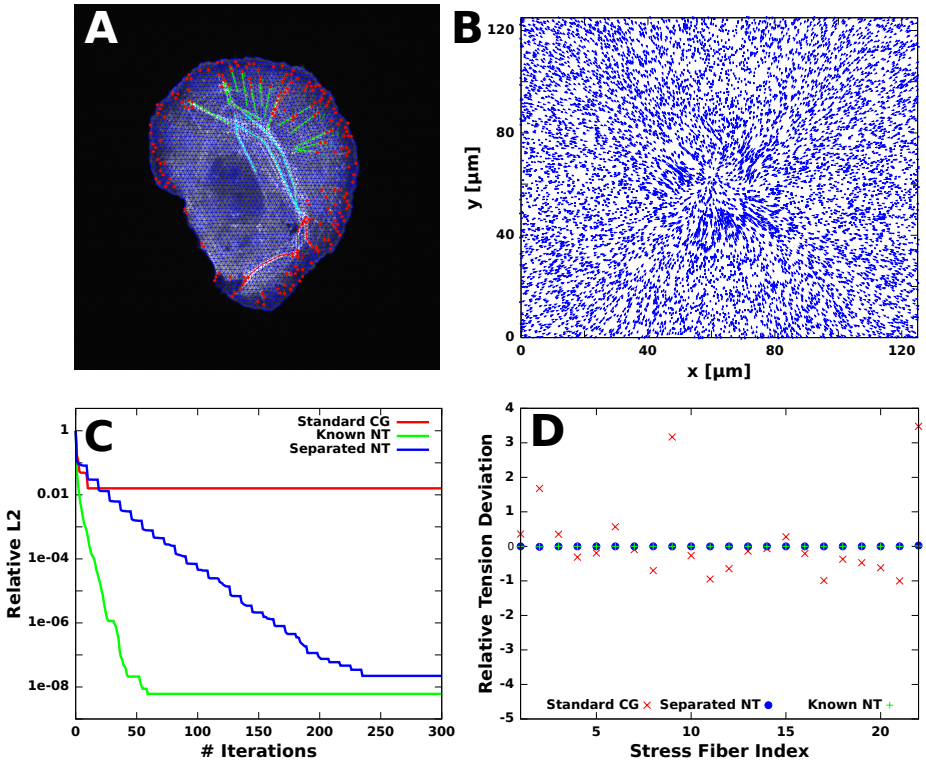

Figure 3.4: Validation of the optimization procedure. (A) Displacements are simulated for a given segmentation based on experimental data. Network contraction is simulated with a fixed network tension $T_{AN} = 0.06\ nN$ and randomly drawn tension values for each SF between 0 and 10 nN. (B) Sampled displacement field from FEM solution, $N = 10000$. (C) Relative L2 value over number of iteration steps for different optimization approaches. Standard CG optimization fails to reconstruct the displacements (red). For optimization with fixed NT (green) a perfect reconstruction can be achieved only limited by the numeric accuracy. Alternating block-wise optimization of NT and SF tensions (blue) allows to almost perfectly reconstruct the simulated pattern. (D) Relative deviation between simulated and reconstructed SF tensions.

3.3.1 Validation of the Optimization Procedure

In chapter 2 we described that the conjugated gradient (CG) method is suitable for minimizing the Tikhonov functional (eq. 2.15). In this case the DoFs of the system had equal weight for influencing the error estimator. In MB-TFM this is different since the model parameters have eventually different impact on the resulting displacement field. The network tension affects all FAs near to the periphery in a similar manner leading to a global change in displacements. Compared to that, variations in single SF tensions induces force changes only at few FAs and thus the effect in the displacement field is locally constraint. At FAs connected to SFs further both tension types tend to compete with each other when optimizing local substrate displacements. Both effects mentioned impede the CG method to converge to the correct solution. A typical fail

of convergence is demonstrated in fig. 3.4 (C) (red curve) for simulated data without noise. To confirm that this originates from the suggested issue, we tested optimization with a fixed network tension $t_{AN} = 0.06\,nN$, which corresponds the simulated value. In that case the CG procedure optimizes the remaining SF tensions to the correct values, see fig. 3.4 (C) (green curve). As a consequence, we modified the CG method by block-wise separated network and SF tension optimization. In detail, a period of one network optimization is followed by subsequent ten iteration steps of SF tensions with the network tension fixed at the current value. Iterative application of this scheme leads to quite the same solution as with fixed network tension just limited by the numerical accuracy, see fig. 3.4 (C) (green curve). The relative deviations of tension values according to the discussed optimization procedures are plotted in fig. 3.4 (D). The plot in detail validates that the reconstruction leads to the same tension configuration, in both cases to successful optimization, while deviations occur in case of the normal CG procedure.

3.3.2 Influence of Noise

Inverse problems are in general very sensitive to noise in the input data and it is important to investigate the noise sensitivity of a new method. Compared to the case of non-planar substrates, discussed in the previous chapter, the contribution of outliers and anisotropic noise is not an issue in the planar case, because we deal only with 2d bead displacements in one plane. Therefore we focused on pure isotropic Gaussian noise in this evaluation. We again defined the noise level n_{noise} via the standard deviation σ_{Gauss} of the noise distribution and the maximal displacement u_{max} appearing in the data set, $n_{noise} = \sigma_{Gauss}/u_{max}$. According to a given noise level random values are sampled from the Gaussian noise and added to each displacement data point. Subsequent evaluation of the result made it possible to analyze the noise influence to different quantities like the relative L2 value, reconstructed cellular total force, and single SF tension values.

Fig. 3.5 shows an exemplary simulated reconstruction for a noise level of $n_{noise} = 25\%$. The example demonstrates the ability of MB-TFM to correctly reconstruct traction patterns even under high noise strength. For the simulated noise level the FTTC completely fails to resolve the correct pattern, since crucial information is missing to discriminate signal from noise. For a subsequent systematic analysis, we investigated a noise range from $n_{noise} = 0\%$ to $n_{noise} = 25\%$, with increased resolution for the experimentally relevant range below $n_{noise} = 10\%$. In this region we evaluated the noise

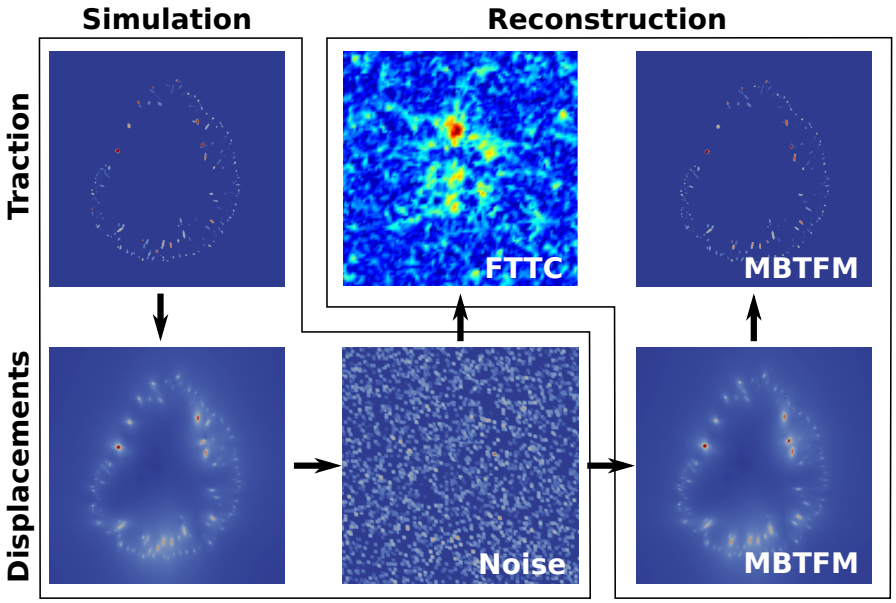

Figure 3.5: Simulation and reconstruction under influence of Gaussian noise. For given traction pattern the displacement field is calculated and afterwards perturbed with Gaussian noise ($n_{noise} = 25\%$). FTTC fails to reconstruct the traction field due to the high noise influence. Reconstruction with MBTFM is almost noise independent and the resulting traction pattern agrees well with the simulation.

levels 3%, 5%, 7% and 10%, while using steps of 5%. For each considered noise level we simulated $N_{sim} = 10$ different displacement fields and averaged over the derived quantities. Fig 3.6 contains the combined result. As expected, the obtained relative L2 value monotonically increases with increasing noise level and converges to 1 in case of extreme noise levels. The grey area in the plot indicates the expected range of L2 values for experimentally relevant noise levels. In case of a perfect model description we expect a L2 value between 0% and 25%. Surprisingly, the total force of reconstructed traction patterns is nearly independent of the simulated noise level, see fig. 3.6 - (middle, blue). Note, the method uses no Tikhonov regularization and thus the result is not influenced by any chosen regularization parameter. A further superior feature of the model-based reconstruction is the ability to deconvolve the different contribution of network and SF tension hidden in the total force. In order to calculate the network contribution, we equilibrated the network a second time using the reconstructed configuration, however, with SF tensions set to the obtained network tension value, $t_i^{SF} = t^{AN}$. The corresponding SF contribution to the total force then corresponds to the difference between total force and network contribution. In fig. 3.6 - (middle, green) the reconstructed network force is plotted over simulated noise levels showing a similar insensitivity against noise like the total force. Obtained SF tensions are,

however, affected. The reconstructions revealed a quadratic dependence of the mean relative deviation $MRD = 1/N_{sim} \sum_{n=1}^{N_{sim}} \left(1/N_{SF} \sum_{i=1}^{N_{SF}} |t_{n,i}^{rec} - t_i^{sim}|/|t_i^{sim}| \right)$ of achieved SF tensions (referred to the real value). Variations from the mean value also increase with the noise level. Within the relevant range regarding experimental data, we expect a noise-influenced SF tension deviation of at most 10%. For the experimental data, which will be discussed in subsequent sections of this chapter, we evaluated an average noise level of $\bar{n}_{noise}^{exp} = 7 \pm 3\%$.

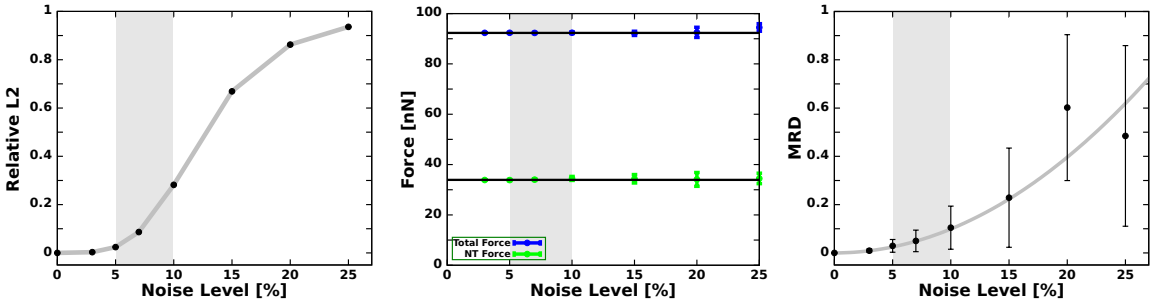

Figure 3.6: Influence of noise to MBTFM reconstruction. The relative L2 value increases monotonically for increasing noise level (left). Nevertheless, the total force F_{tot} (blue points) and network force F_{AN} (green points) hardly deviate form the simulation value (solid black lines). The mean relative deviation (MRD) of SF tensions increases quadratically with increasing noise level (right).

3.3.3 Over- and Undersegmentation of Stress Fibers

Precise segmentation of SFs and FA with our *ImageJ* plugin is a key issue in MB-TFM. Since the introduced SFs directly enter the optimization in terms of their tension value and FAs determine the traction distribution, imprecise segmentation of both could have a negative effect to the results. Especially introduction of more or less SFs may induces a different intracellular tension distribution.

FA segmentation is done automatically with high accuracy and thus we do not expect much inaccuracy. However, due to interactive SF segmentation it is possible in some cases that too less (under-segmentation) or too many SFs (over-segmentation) have been segmented. In order to explore how imprecise SF segmentation affects the reconstruction result, we considered three exemplary segmentation mistakes, which are depicted in fig. 3.7 (A)-(C). The first segmentation represents an over-segmentation by three eventually random VSFs at positions with less obvious actin structure. Here, we checked if the optimization procedure ignores the additional SF parameters. In

a second segmentation, two DSFs have been removed compared to the original segmentation. This allowed us to study, to what extend other SF tensions balance a unsegmented fiber. In the third case we removed a VSF. The chosen SF has no parallel neighbors suggesting that a larger reorganization occurs while fitting an approximated solution to the displacements.

The simulation results are summarized in fig. 3.7 (D)-(F). Here, we find that over-segmentation with random SFs (yellow triangles) leads to correct L2 values and reconstructed SF tensions are almost uneffected by the additionally introduced DoFs. Hence, as we expected the optimization procedure ignores additional DoFs. This makes clear that the model supports reconstruction but however results can not be biased by introducing arbitray numbers of additional DoFs. The effect of under-segmentation is different. Since the number of DoFs is reduced, the system can not describe the entire displacement field anymore. This leads to an increased L2 value and some SF tension values tend to deviate from the true value. Looking closer, the latter is a localized effect in most parts since particular SFs close to the missing ones try to compensate lacking tension with larger values. E.g. in case of the second segmentation, SFs 13 and 15 were removed (yellow triangles) and in the reconstruction the neighboring SFs (red triangles) show increased deviations larger than 50% while all others show deviations smaller than 40%. In case of the third segmentation the contribution of the missing VSF (yellow triangle) is compensated by a multiple SFs. Here, the removed VSF had a central impact on the displacement field and in especially the TA (red triangles) respond with deviating tensions above 50%, however the others stay below. Regarding cellular total and network force, over-segmentation has no influence. In case of both under-segmentations the total force is slightly underestimated, while the network force is in the same way overestimated. This agrees with expectations since the network tension partially tries to compensate a missing fiber tension.

In summary, under-segmenation seems to have a larger effect on the reconstruction of SF tensions than over-segmentation. However, the different results in case of both exemplary under-segmentations show that also the position and the structure of the close neighborhood to a missing fiber influences the intracellular tension distribution. Nevertheless, due to the special mechanical property of the cable network, which does not propagate tension over longer distances, a global impact to SF tensions is damped.

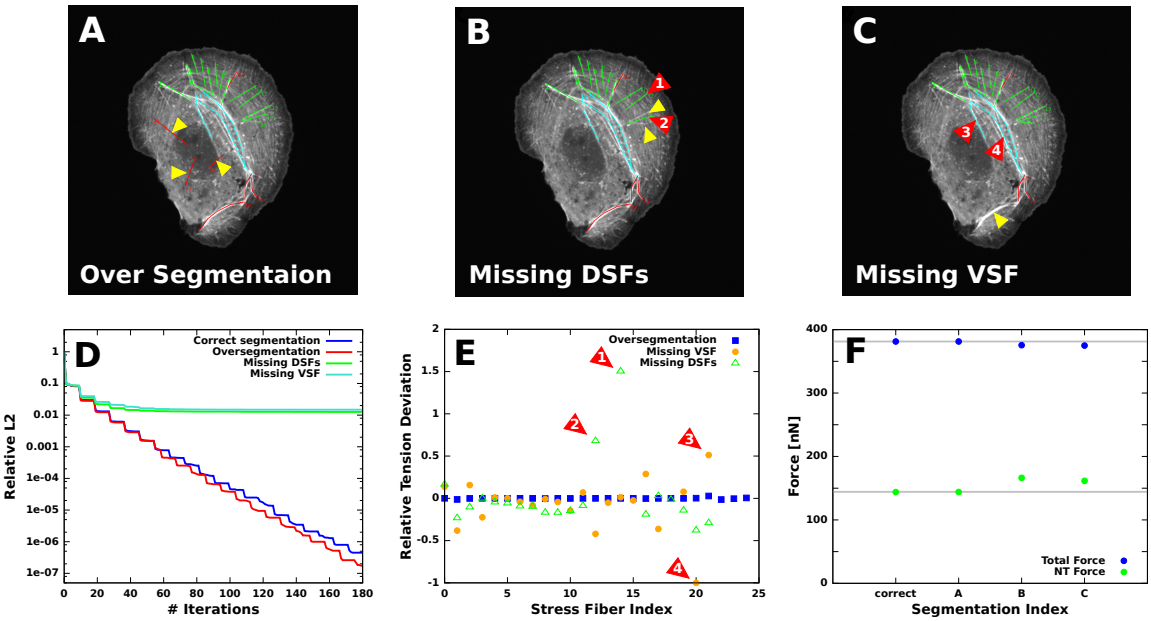

Figure 3.7: Effect of over segmentation and missing SFs. (A)-(C) Simulated exemplary segmentation mistakes. (A) Over-segmentation: additionally introduced VSFs. (B) Under-segmentation 1: two missing DSFs. (C) Under-segmentation 2: removal of a prominent VSF. (D) Convergence plot of the optimization procedures given for the separate segmentations. (E) Relative tension deviations of reconstructed SF tensions. (F) Reconstructed total force and network.

3.4 Comparison with FTTC

The different conceptual difference of standard FTTC and MB-TFM is illustrated in fig. 3.8. MB-TFM incorporates available secondary biophysical information about the CSK and FAs into the traction reconstruction process. In contrast to that standard techniques like FTTC reconstruct traction fields by knowledge of substrate properties and deformations alone. This demands additional regularization in order to achieve stable approximate solutions of the inverse problem. The disadvantages of Tikhonov regularization has been discussed before. We note again that the regularization strength is controlled by a scalar parameter, which among other things influences the typical feature size of traction hot spots. In our opinion it is reasonable to consider a fixed feature on the length scale of a few micrometers according to the typical size of a FA. Hence, if we want to compare results from MBTFM and FTTC, we are searching for an optimal regularization parameter that accounts for the feature size of traction hot spots. Currently used parameter selection methods like the L-curve criterion only target an optimal noise reduction without further knowledge about the system (53).
In order to compare FTTC and MB-TFM, we plotted the total force per cell obtained

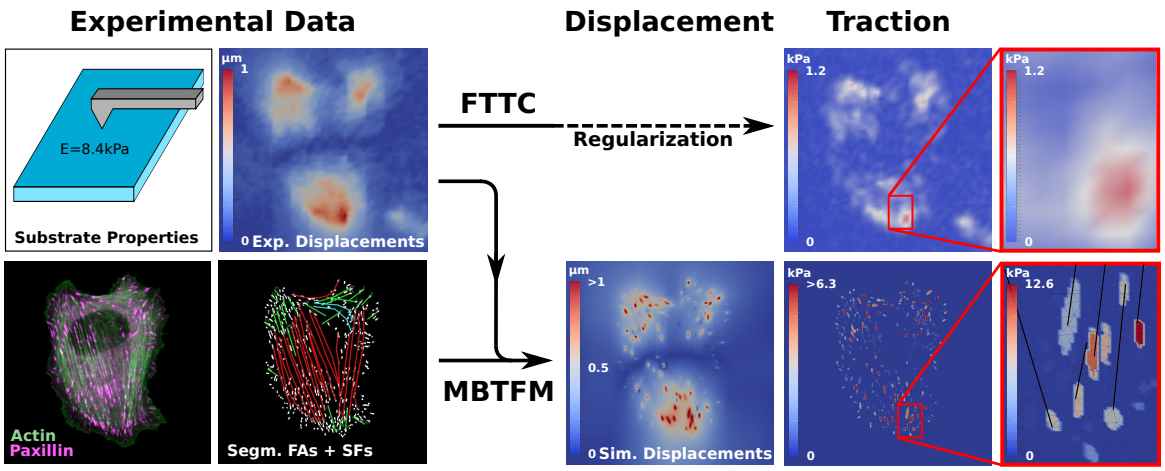

Figure 3.8: Illustrative comparison of FTTC and MB-TFM. The main difference between FTTC and MBTFM is the used information that enters the traction reconstruction. FTTC uses measured substrate properties and deformations alone, while MB-TFM additionally incorporates the distribution of FA and the actin CSK structure in terms of segmented SFs. FTTC needs additional regularization ($\lambda = 5 * 10^{-5}$ fitted by comparison with MB-TFM). The reconstructed traction distributions differ in their resolution. While FTTC distributes traction forces over neighboring, MB-TFM selectively reconstructs traction on the level of single FAs. Black lines in the lower inset indicate SFs.

with FTTC (integrated traction underneath the cell area) over those achieved with MB-TFM for experimental data of 19 U2OS cells. Interestingly, we found a robust linear relation over the entire sequence of different regularization parameters. The slope, respectively the correlation coefficient turned out to be only dependent on the regularization parameter. This motivated us to propose a calibration scheme for an optimally chosen parameter λ by adjusting the total force value derived from FTTC to the corresponding MB-TFM reconstruction by choosing an regularization parameter λ that fits to a one to one relation. This allows to effectively adjust the regularization strength in a noise independent fashion eventually based on biophysical considerations since MB-TFM results are shown to be almost insensitive against experimental noise. For the given data we obtained an optimal parameter of $\lambda = 5 * 10^{-5}$, which is on the right order of magnitude according to experiences with high resolution FTTC measurements (personal communication with B. Sabass (Co-author of (47))).

3.5 Results: Quantitative Study for U2OS Cells

After method validation we demonstrated the application to experimental data. We analyzed a data set of 21 U2OS cells, provided by collaboration partners (Jonathan Stricker and Patrick Oakes, Gardel lab, University of Chicago, USA). All cells were

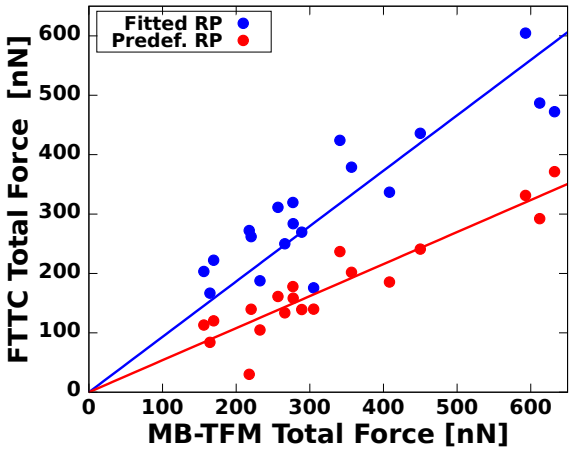

Figure 3.9: Calibration of FTTC measurements to MB-TFM. Plot of reconstructed total forces from FTTC over these from obtained from MB-TFM results in a linear relationship. The slope depends only on the chosen regularization parameter. (red) predefined $\lambda = 1 * 10^{-4}$ and (blue) $\lambda = 5 * 10^{-5}$ optimized by fitting a one to one relationship (the straight line through origin with slope 1).

seeded on planar PAA substrates with a Young's module of $E = 8.4kPa$. Due to the incompressibility of these substrates the Poisson ratio was chosen to $v \approx 0.5$. Taking advantage of the model-based approach, we present a detailed correlation analysis of cell generated total forces regarding cellular properties like cell area, FA area, and number of FAs. We evaluated how the connection of SF to FA promotes their probability to exert larger forces, and how the classified SF types differ in their contractile strength. We started the analysis with a direction orientation analysis of local displacements, FAs, and SFs, which confirms basic model considerations.

3.5.1 Actin Organization Determines Direction of Traction Forces

As a preliminary step, we checked the agreement of model considerations with the provided data. The model approach with active cable networks uses two basic assumptions: traction forces are constricted to areas of segmented FAs and the particular distribution of forces is a consequence of cell contraction caused by network and SF generated tensions. The difference between these two types of tension generating modes is that network contraction (as we model it by a single tension value) has a global isotropic effect on FAs at the periphery. On the other side SFs tensions are transmitted almost exclusively via few FAs leading to localized effects on the substrate displacement. Larger resulting network forces appear just at FAs near to the cellular periphery and their directions are radial directed perpendicular to the cell edge. The condensation of

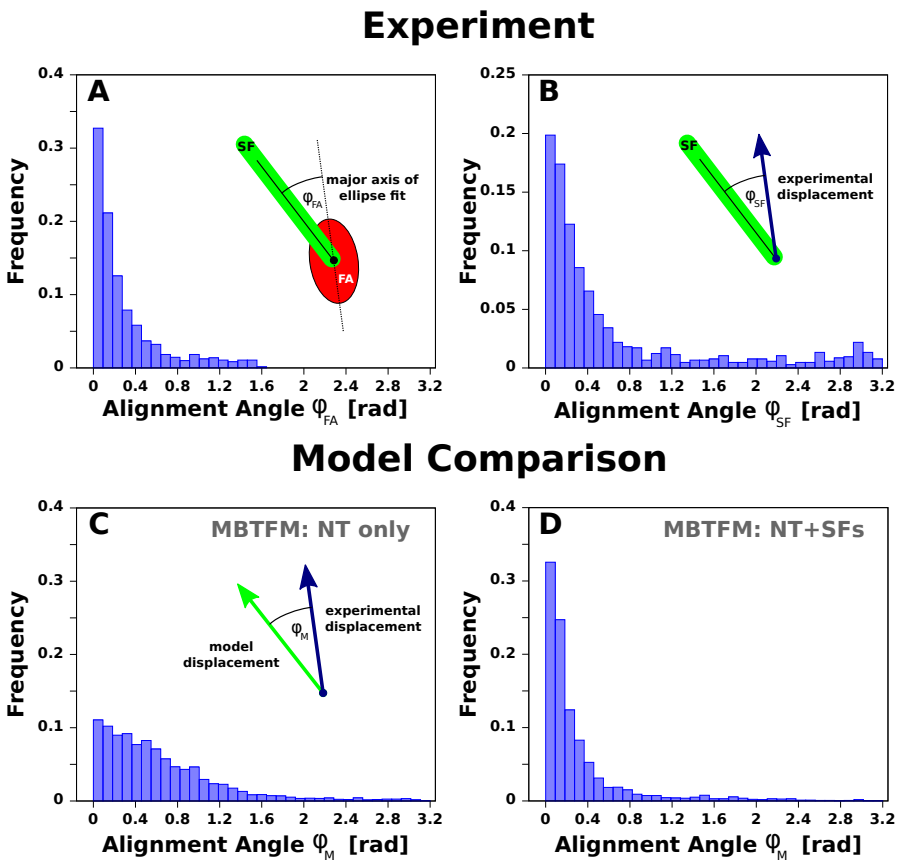

Figure 3.10: Correlation of FA, SF, and local displacement directions. (A) Frequency of angular differences between the direction of the main axis of the FA and the direction of an attached SF ($N = 1305$). (B) Frequency of angular differences between SF direction and locally measured substrate displacement at the SF's anchoring point ($N = 1297$). (C) Frequency of angular differences between experimental local displacements and the corresponding displacement obtained by MB-TFM only optimizing network tension (isotropic network contraction). (D) Frequency of angular differences between experimental local displacements and the corresponding displacement obtain by MB-TFM optimization network and SF tensions (anisotropic network contraction).

forces to the cell edge is a typical effect described also for isotropic continuum models (105, 106, 107). Compared to that SF induced forces contribute in a much more local anisotropic fashion and force directions are guided by SF orientations. Depending on the SF types diverse orientations can be found strongly deviating from a strict radial direction.

In order to analyze the impact of SFs to local forces, we determined local displacement direction and SF orientation on their anchoring points. In case of a isotropic contraction, when e.g. the network is the only force generating component the directions should lead to no or less correlations. Reversing this argument, a prominent correlation would hint to an apparent contribution of SFs to local stresses. Indeed the result

for $N = 1297$ evaluated positions shows that local substrate displacements and SF orientations most often coincide well with each other, see fig. 3.10 (B). Subsequently, we compared the local displacements on the same positions for a model-based reconstruction for active cable networks with (anisotropic model) and without SFs (isotropic model). The results in fig. 3.10 (C) + (D) strikingly show that only the full model with embedded SFs recovers the observed correlations, while a SF free network achieves only a poor agreement. The results on the one hand confirm the model considerations and on the other hand point out apparent limitations of purely isotropic models.

3.5.2 Force Correlation Analysis on Cellular Level

Since the invention of quantitative force measurement techniques many studies have been published that aim at revealing cell properties that promote contractile strength of cells. The goal of this studies is to get a deeper insight into cell mechanics and mechanisms of mechanotransduction. As an example, previous studies found that stem cell fate decisions are influenced by early changes in cytoskeletal contractility (23) and that the metastatic potential of cancer cells increase with the amount of exerted traction stress (69). However, experiments have yielded no clear picture and some of the results are contradicting. Positive correlations of traction forces have been found for cell area (108, 109, 110, 111), FA area and number (21, 23), as well as cell geometry (112, 113, 114). Possible reasons for the different results are versatile. From a biological point of view, a potential problem is that each study deals with different cell types. It is self-evident, that an epithelial cell (e.g. Reinhart-King et al. (115)) may show different properties than for example human mesenchymal stem cells (hMSC) studied by Fu et al. (23) or human airway smooth muscle (HASM) cells surveyed by Wang et al. (110), as they fulfill different functions in the body. Another issue is that the experiments have been carried out under different conditions. Some of them used elastic pillars instead of planar substrates or used micropatterning techniques that constrain cells to unnatural geometries. More various combinations can be found in the literature. However, these conditions are known to influence cell behavior (61, 116). As last point we emphasize that the entire set of traction reconstruction techniques were applied including their advantages and disadvantages.

With the advantages achieved by MB-TFM, we contribute a cell forces analysis for human bone osteosarcoma (U2OS) cells on planar substrates with unconstrained cell shape. The amount of force exerted by a cell was measured by summing up obtained FA forces. In a subsequent step we carried out a correlation analysis with respect to traction force, cell area, FA area, FA number, and number of SFs counted per cell. In

addition, we use the novel model-based feature of MB-TFM to determine the separate intracellular strength of actin network contraction and SF tension contributing to the cellular traction force pattern. The newly accessible data may then hint to the mechanism a U2OS cell uses to control force application to the environment. In order to obtain the same correlation qunatities as used by the studies referred before, we use the data from our image processing tool, where we quantified cell area, FA area, number of FAs, and number of SFs.

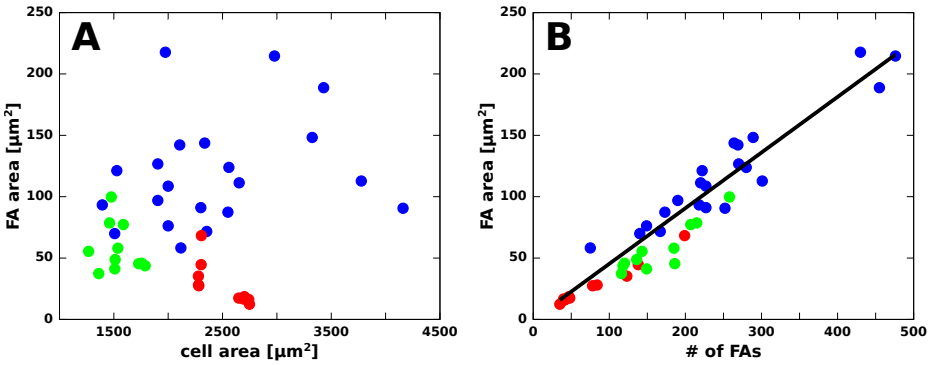

Figure 3.11: Correlation of cell area, FA area, and number of FAs. Cell area and FA area show no distinct correlation, while FA area and number of FAs show a clear linear scaling, which can be fitted by a line through origin with slop $m = 0.46 \pm 0.1\ \mu m^2/FA$, which represents a measure for the mean area per FA. Color code: WT cells (blue, $N = 21$), Y27632 inhibited cells (red, $N = 11$), and α-actinin 1 knockdown cells (green, $N = 11$).

First, we investigated a possible force dependency on cell area, FA area and number of FA. The two plots, fig 3.11, depict that in contrast to Fu et al. (23) we found no clear scaling between cell and FA size in our data set. However, the number of FAs and FA area show a distinct linear relation, which can be fitted by a line through origin, which allows us to calculate a mean area per FA of $0.46 \pm 0.1\ \mu m^2$. Regarding inhibition of the cell's contractility with Y-27632 and knockdown of the actin cross-linker α-actinin, a slight effect on the mean FA area towards the development of smaller FAs can be observed. This is consisted with other more detailed studies on the maturation of FAs (91, 117).

In fig. 3.12 the essential plots regarding correlations with cellular forces are depicted. We found a clear scaling between total force per cell and number of FAs. This also corresponds to a scaling with respect to FA area since we found a clear linear relation between number of FAs and FA area (fig. 3.11 (B)). From fitting the U2OS wildtype cell data points with a line through origin, we obtained a mean force per FA of $1.9 \pm 0.05\ nN$. Considering a constant force distribution over FAs, we calculated a mean traction value

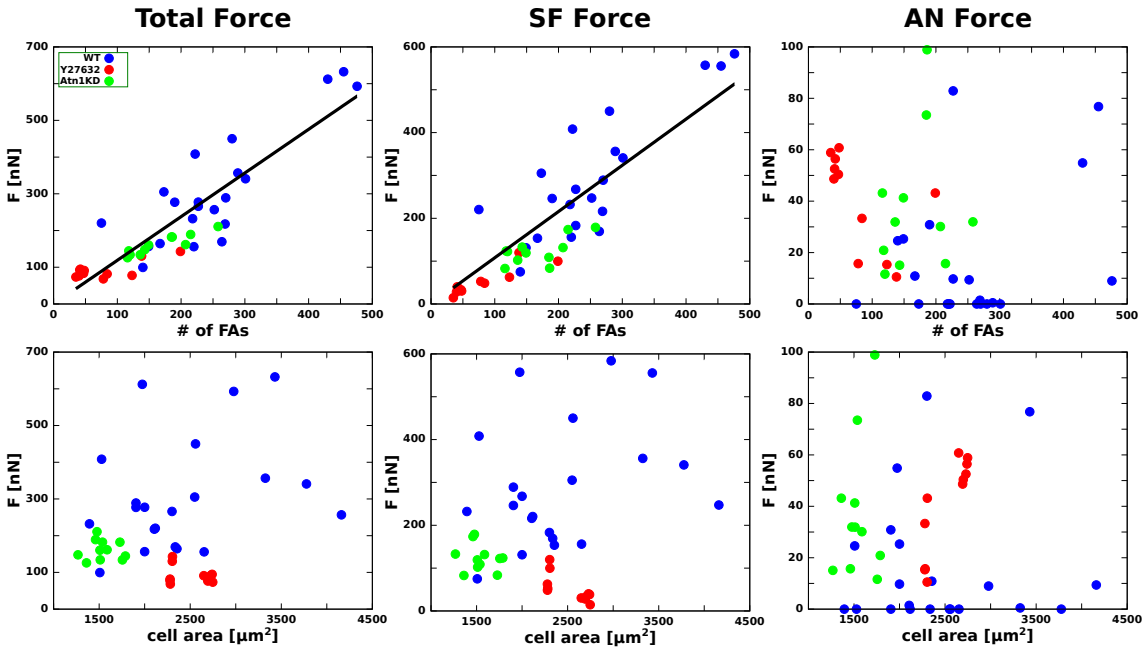

Figure 3.12: MB-TFM: Cellular Total-, SF- and AN force plotted over FA number and cell area. Total and SF force show a linear scaling with the number of segmented FAs (fit: black lines, slopes: $m_t = 1.19 \pm 0.05\ nN$, $m_{sf} = 1.08 \pm 0.05\ nN$). Plotting the same result with respect to cell area reveals at most a weak dependence. The AN force is neither correlated with FA number nor cell area. The data points represent WT cells (blue, $N = 21$), Y27632 inhibited cells (red, $N = 11$), and α-actinin 1 knockdown cells (green, $N = 11$).

(force per FA area) of $4.13 \pm 0.1\ \frac{nN}{\mu m^2}$. This value is on the typically order of magnitude compared to results carried out by e.g. studies on strong cardiac myocytes ($5.5 \pm 2\ nN$ (21)), humane mesenchymal stem cells ($3.7 - 2.0 \pm 0.5\ nN$ (23)), or 3T3 fibroblasts ($2 - 10\ nN$ (118)).

Interestingly, we found out that SF induced contractility dominates the overall forces exerted by these cells. This was already suggested by the orientation analysis (fig 3.10 (B)), where we determined a strong alignment of SFs and local substrate displacements. The analysis shows that the SF contribution is roughly six times larger compared to the actin network. We also found that the amount of SF forces per cell scales positively with FA area. Compared to that the network force seems to be uncorrelated to both quantities, FA area and cell area. This result supports the picture that U2OS cells control the application of traction forces by the amount of assembled FAs or FA area respectively, while SFs connected to FAs are the main force generating structures within the cell. In the following section we will investigate this aspect more elaborately by analyzing MB-TFM results at the level of individual FAs and SFs.

3.5.3 Correlation Analysis for Single Focal Adhesions

Evaluation of tensions on the level of single FAs is of particular importance. The reason for this is that FAs are known to respond sensitively to applied tension (87) and are suggested to act as force sensors in mechanotransduction (25, 27, 119, 120). In order to achieve a better comprehension of the molecular mechanisms of this kind of signaling, it is desired to established force microscopy methods with single FA resolution. Successful early approaches have been carried out by Schwarz et al. (52) and Tan et al. (41) on solid elastic substrates and micropillars, where both found a positive correlation of FA area and single FA force. Note, the distinction between the results based on total force per cell and FA area per cell will be discussed in the previous section. They allow only an averaged conclusion. Further experiments by Stricker et al. (90), in which dynamics of FA growth have been traced, came to the conclusion that a positive correlation of FA size and traction forces only exists during the initial stage of FA maturation, while mature FA miss such a relation. This contradicts the previous results since the other experiments deal mainly with very large mature adhesions, which accordingly should show no correlation.
Although various cell types have been used again, we suggest that the application of different traction reconstruction techniques might explain these contracting results. The main problem on reconstructing highly resolved traction patterns on solid elastic substrates is the superposition of displacements caused by different traction source in terms of neighboring FAs. In order to distinguish the exact contribution of e.g. each FA, weak differences in the local substrate displacement have to be recorded. This needs extraordinarily large bead densities and super resolution microscopy (compare to (47)). We already discussed that Tikhonov regularization in FTTC affects feature size and magnitudes of traction spots and may lead to biased force distribution in the vicinity of neighboring FAs. Unfortunately, according to our knowledge there exists no adequate formulation of experimental requirements for confident single FA resolution. Different from this, with MB-TFM we propose a way to compensate insufficient displacement resolution by incorporating additional information to the reconstruction process. The MB-TFM approach with active cables allows us to achieve higher resolutions based on a well-founded cellular contraction model. This permits to determine unique FA force distributions in a parameter-free way without requiring Tikhonov regularization.

For the subsequent analysis we focused on the question, how FAs differ in their potential to exert traction stresses if a SF is attached to them and how the size of FAs might

be influenced by applied SF or network tension. The size of a FA at a certain time t results from a continuously ongoing maturation and degradation process. In MB-TFM, we determine the forces of all segmented FAs with respect to the current cell state. Since we here do not discriminated FAs by their position or maturation state the result includes the entire ensemble of different states. By means of the So-FASt ImageJ plugin we evaluated for each FA whether it is connected to a SF or not. A subsequent frequency analysis of FA areas revealed the tendency of FA connected to SFs to be significant larger than these, which are not connected (fig 3.13 (A)). This hints at higher force values since FA growth from nascent adhesions to mature FAs is proposed to be tension dependent (28, 87), especially at the initial stage incorporating the maturation of focal complexes to FAs (90, 121).

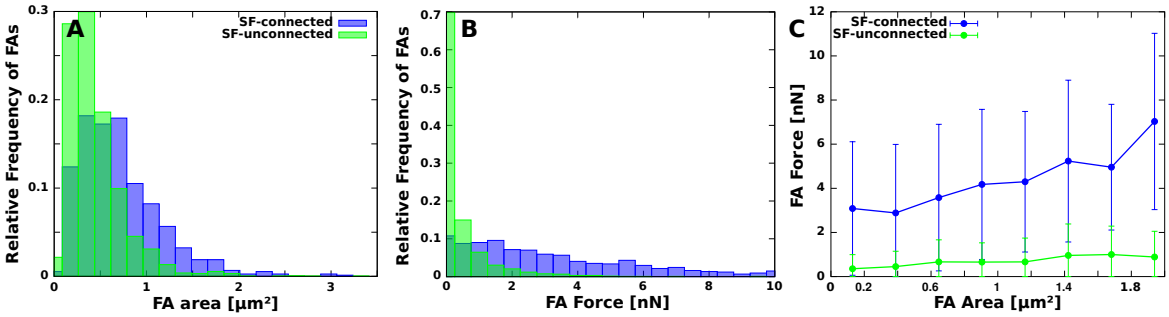

Figure 3.13: Force distribution of FAs connected and unconnected to SFs. Distribution of relative force frequency (left) reveals a distinct tendency of FAs attached to SFs to exert higher traction forces. Mean force over FA area separated by FA-SF connection (right), $N = 3612$.

The combined MB-TFM results for the entire data set of U2OS wild type cells discussed in the previous section are plotted in fig. 3.13 (B)+(C). In agreement with our biophysical considerations, we obtained different force distributions for connected and unconnected FAs. Unconnected FAs are most often weaker with a low probability to exert forces larger than 1 nN. For connected FAs, we got a much broader distribution with a high probability to exert larger forces (> 1 nN). For both FA types we got a broad distribution with apparently unclear scaling with FA size, which might reflect the diversity of mixed FA states (plot not shown here). However, calculation of binned mean forces for both types reveals a weak correlation. Despite large standard deviations, the mean forces of connected FAs show an approximately linear relations with FA size. Nevertheless, also small SF-connected FAs exert apparently larger forces than unconnected ones. In case of SF-unconnected FAs the scaling is less clear and seems to be constant on a level of lower force magnitudes compared to connected FAs. It can be argued that the model introduces a bias towards a preference of Sf connected FAs,

however, the results fit into the picture drawn by the direction correlation analysis presented in section 3.10 and to distinct area distributions of both types of FAs (fig 3.13 (A)). Nevertheless, values for the distribution of internal stress are only guided by a fitting process towards a best agreement with measured displacements. Thus the essence of our reconstruction bias is the broadly accepted picture of contractile cell whose force generating machinery consists of a contractile actin network and contractile SFs.

3.5.4 Distribution of Tension in Different Stress Fiber Types

As already mentioned briefly in the methods part of this chapter 2.2, we classified SFs according to the definitions proposed by Hotulainen and Lappalainen (82), which discriminate SFs by an individual assembly mechanism. According to the literature we distinguished three types: dorsal SFs (DSF), transverse arcs (TA), and ventral SF (VSF) (82, 122, 123, 124). DSFs are attached to one FA and grow by actin polymerization localized at the connecting FA supported by formins. To form a bundle they also require the crosslinker α-actinin (125). TAs are suggested to play an important role in cell migration (126) and to be generated by annealing network actin filaments with myosin II at the lamella. VSF are suggested to originate from both, former DSFs or TAs (82). They are connected on both ends to FAs and show a sarcomeric internal structure similar to myofibrills in muscle cells, suggesting strong contractility (127). Although the assembly mechanisms of different SF types are known, it is completely unclear if they also differ in their contractile potential. Kovac et al. (125) e.g. suggested that DSFs are non-contractile since they found no myosin II in the fiber assembly. However, it is also known that high association and dissociation rates of crosslinker and motor proteins allow the cell to quickly change the mechanical properties of actin fibers and their contactility (82).

In the subsequent analysis we show a quantitative analysis of the SF tension distributions within U2OS cells ($n_{SF} = 369$). Here, we concentrate on the separate evaluation of tension in different SF types. According to our knowledge, this is the first evaluation of this kind since up to now appropriate methods were not available. Fig. 3.14 shows the obtained distribution of single SF tensions. The evaluation for each fiber type is based on entire data set of U2OS cells in order to average out effects from the current cell state (e.g. more quiescent or motile shape). Interestingly, we found apparently

different single SF force distributions. Although the distributions overlap, distinct distribution shapes can be found. DSFs are most frequently weaker than 1 nN (fig. 3.14 - green), while VSFs dominate the region of high forces (> 5 nN), see fig. 3.14 - red. TAs seem to obey an intermediate force distribution somehow between DSFs and VSFs ((fig 3.14 - turquoise).

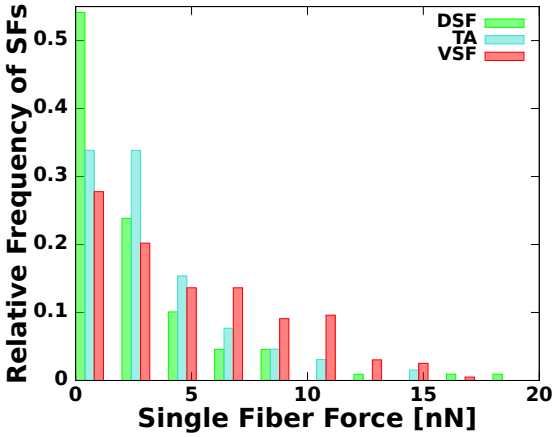

Figure 3.14: Single SF fore distribution for differently classified SF types ($N = 369$). The distribution for DSF decays quickly to towards larger forces with approx 10% is larger than 5 nN (green). Compared to that over 30% of VSF bear forces larger than 5 nN (red). The distribution for TA represent an intermediate distribution between DSFs and VSFs (turquoise).

An interesting aspect of the obtained force distributions is that the different SF types show distinct contractile behavior. However, the distributions are not clearly separated. Note, the analyzed cell ensemble consists of cells in variable internal states. Further cells highly control their contractility mediated by correspondingly quick turn over rates of crosslinker and myosin proteins (82). From this point of view, the variability in obtained SF tension is reasonable and it is even more remarkably that we found distinct tension distribution though averaging over multiple cells.

Based on this result we became interested in finding out whether the determined distributions also fit to an individual cell in the data set. In order to test this, we carried out the following simulation. For a given segmented cell, we assigned random tension values to the individual SFs based on the measured tension distributions (fig. 3.14), while we accounted for the different SF types. Afterwards we calculated the resulting substrate displacement field and compared the result with the experimentally measure bead displacement using the L2 estimator. After repeating this procedure several times ($N = 500$), we obtained a Gaussian shaped distribution with respect to obtained relative L2 values, see fig 3.15 - green. Then we repeated the simulation while we switched

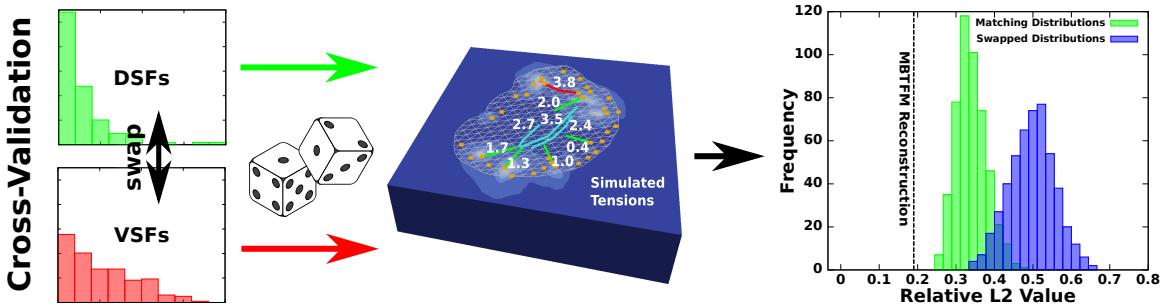

Figure 3.15: Crossvalidation of obtained SF tension distributions. Based on the obtained distributions with respect to different SF types, we draw random values, which we assigned to a exemplary segmentation in the data set. In order to check the significance of the results, we used once with distributions in correct order and once a combination in which the distributions of DSF and VSF have been switched. Simulating both $n = 500$ times led to Gaussian distributions with respect to the achieved relative L2 (correct=green; switch=blue). The dash vertical line indicates the achieved value for this data when applying MB-TFM.

the distributions of DSFs and VSFs from which the random values were drawn. Again the result was a Gaussian distribution, however, with a broader shape and centered around a significantly larger L2 compared to the simulation before. This type of cross validation shows that although we used random tension values for the segmented SFs, we get apparently better agreements with the real measurements if we use the right distributions. This supports the validity of the obtained distribution and that they are not only an effect of averaging over a limited number of cells.

In summary, on the level of multiple cells the total force is positively correlated with the number of SFs irrespective of the particular composition of SF types. Corresponding correlation plots with respect to the number of SFs can be found in the appendix A.2. On this scale the distinct force contributions of different SF types average out when only total forces are regarded. Having a look at the level of single SFs and analyzing their individual force contribution based on the same data set, we obtain distinct force distributions for each fiber type. Unfortunately, the distributions intersect each other, which may explain why this difference can not be seen when we only consider total forces.

3.6 Summary & Discussion

In this chapter we introduced model-based traction force microscopy (MB-TFM) as a novel technique to reconstruct cellular traction forces from the deformation of planar elastic substrates. As a new concept we incorporate additional data and biophysical

modeling into the reconstruction process. As a concrete implementation of this techniques, we used active cable networks with embedded SFs and the distribution of FAs as constraint to find approximated solutions of the inverse elastic problem. We proposed a combination of cell and substrate modeling embedded in an flexible optimization framework, which allows us to optimize model parameters directly from measured substrate displacements. The use of auxiliary experimental information enabled us to obtain unique traction fields without requiring additional Tikhonov regularization.
We integrated information about cell shape, actin SFs, and cell-matrix contacts into the model network by using a self-written image processing tool implemented in ImageJ. In a subsequent step we optimized network and SF tension parameters of the active cable network to achieve best agreement with measured substrate displacements. We validated the methods reliability by reconstructing simulated data. In contrast to state of the art methods, it turned out that MB-TFM is almost insensitive to simulated noise. This represents a substantial advance since it allows to determine comparable absolute total force values exerted by cells independent of a freely chosen regularization parameter. Interestingly, we found a linear relationship between cellular total forces obtained from MB-TFM and FTTC, while the proportionality constant depends only on the chosen regularization parameter. As this basically defines force scale and feature size in standard TFM methods, we are able to calibrate standard FTTC by comparison with MB-TFM results, which represents a possible alternative to commonly used parameter selection methods selection (49, 53).
Systematic reconstruction of simulated data allowed us to estimate the model-induced error of the reconstruction. The actual noise level in the data could be determined by fitting a Gaussian distribution magnitudes of displacements measured at cell free regions of the substrate. By applying comparable simulations with the same bead density and noise level an expected L2 value can be identified in case of a perfect model agreement (like shown in plot 3.6 - left). The difference of expected and obtained L2 value then allows us to give an estimate about the model error. For determined SF tensions, we obtained a noise-induced relative deviation of approximately 10%.
We applied MB-TFM to experimental data of U2OS cells. Here, we investigated cellular forces on on different length scales. On the scale of single cells, we found that the strength of cellular contractility depends on the number of FAs respectively on the area covered by FAs. For the provided data we could not confirm a positive correlation on cell area as reported in several publications based on other cell types (23, 109, 111). We cross-checked this result with FTTC traction reconstruction, see appendix A.1. Further, we used the model-feature to trace back the origin of applied force within

different components of the actin CSK. We found that $80-90\%$ of the cellular force in our data sets originate from SF contractility and the remaining $10-20\%$ are based in actin network contraction. This result was further confirmed by a correlation analysis of SF, FA, and local displacement directions. Another interesting result is that the total force depends on the number of FAs and seems to be mainly caused by the SF contractility since the network part shows not distinct correlation to any surveyed cell property. On the scale of single FAs, we obtained distinct force distributions for FAs connected and unconnected to SFs, see 3.13. The result is indirectly supported by different area distributions of FAs regarding their connection to SFs (fig. 3.13 (A)), which further hints to distinct force distributions. In summary, although the reliability of the result can be discussed it further demonstrates the need for higher experimental resolution in substrate displacements as demonstrated by Plotnikov et al. (47). Our model-based approach here represents an alternative way to enhance the resolution for data with limited substrate displacement resolution.

The application of active cable networks with SFs in MB-TFM provides another special property yet. Model-based decomposition of superposed traction sources the approach enabled us to assign reliable force values to each SF directly from optimized model parameters. Previous invasive methods based on laser cutting of SFs are just able to determine the mechanics of a few SFs in one cell. Compared to that we showed a way to estimate the entire distribution of SF tension, which makes a systematic quantitative analysis possible. The analysis of the provided data revealed a diverse contractile potential of different SF types. This has been suggested in the literature before due to distinct molecular compositions and assembly processes (82, 124, 128). According to our knowledge the results show a quantitative analysis of SF forces based on a large statistics ($N = 369$) for the first time, see 3.14. As suggested by biochemical studies that reported a lack of myosin II proteins in DSF, we found that these fibers are weaker than the other types. Compared to that VSF are found to be the strongest fiber type. This is as well suggested through their ordered structure of α-actinin and myosin II minifilaments and their dynamics when biochemically contractility is inhibited (127, 129). Transverse arcs generate intermediate forces. They are internally less ordered than VSFs, however, they recruit myosin II (126), which suggests a certain amount of contractility.

The active cable networks used in our evaluation represent a simplified static model for cellular contractility. It was originally proposed to describe the shape of adherent cells in a less motile state. However, cells are active systems. This becomes especially clear for example when we consider the cell property to switch quickly between motile and

quiescent states accompanied with a highly dynamic actin CSK. For some cell states the assumption of static equilibrium may not be entirely supported and active processes such like actin polymerization and depolymerization are supposed to dominate resulting forces transmitted to the substrate (130, 131, 132). This may explain why we found contractile DSFs. Since our model considers only contraction, appreciable forces at FAs distributed at the leading edge result in non-zero SF tensions, although the force can also be originated from friction forces with the retrograde actin flow. A dynamic investigation for this has been carried out by e.g. Shemesh et al., which considers mechanical interaction with a retrogradly flowing elastic actin network as mechanism for FA maturation and SF formation (102, 103). In case of VSFs the picture is much more clear. They are more persistent and most often located at inner less dynamic parts of the cell. Hence, it is most likely that contractile tension generates traction forces here. Although the active cable model implies considerations that are at least not entirely capable to describe cellular complexity, small estimated model errors hint to adequate description while keeping the number of free model parameters acceptable small. For future studies it would be an interesting question to extend MB-TFM with dynamic models in order to track e.g. the force dynamics in growing FAs and SFs, or to analyze the force dynamics in cell migration.

4

Thermoelastic Modeling of Cell Contraction

The ability of cells to actively contract is an important feature for multicellular organisms. Many soft tissues are under steady mechanical tension, which is called "tensional-homeostatis"(133). The degeneracy of certain tissue types like for example malignant breast tumors goes along with changes in tissue tension (133, 134). Tension in tissue is generated by contraction of cells embedded in the extracellular matrix (ECM). Cells accordingly also sense tissue tension, which feeds back into cellular biochemistry via mechanotransduction (10). A special issue in cancer research is the importance of cell and tissue mechanics in tumor progression. During metastasis cells translocate through the body in order to invade healthy tissue. When these cells are cultivated on elastic substrates, they often strongly indent the substrate surface (135). It was also found that the indentation strength correlates positively with the cell's metastatic potential. This suggests that metastatic cells actively apply contractile forces to establish tissue invasion. An open question at this point is, how cell geometry and mechanics could promote this process.

Another example we want to investigate in this chapter, is the issue of collective cell migration. This term describes the general phenomenon of collective and persistent movement of cells. A prominent example is wound healing in the skin (136), where specialized cells migrate into wounded areas to subsequently initiate the healing process. There are essentially two experimental setups to study collective cell migration in vitro. The first one is the so called "scratch assay". Here gaps are scratched into a cohesive tissue monolayer. After a short time collective cell migration starts in order to close the gap and to establish again a cohesive tissue (137). The second method is based on patterning tissue monolayers using PDMS microstencil masks (138). This

approach allows to achieve differently shaped cell-free areas, which is not possible in the scratch assay. After removal of the mask cell migration starts and can be studied. Stencils allow to establish arbitrary cell colony geometries more precisely than the scratch assay. Recent works studied collective cell migration and wound closure on different geometries (139, 140), while some of them also incorporate traction force microscopy on soft elastic substrates (141) or pillars (142). Here, the traction force results can also be utilized to estimate the intercellular tension distribution within the cell sheet, by approximating the monolayer as two-dimensional elastic material (143). This allows to integrate mechanical substrate interaction into dynamic cell layer models in 1d (144) and 2d (145). Considering collective cell migration as expansion of an elastic material like modeled in (145), one would expect traction forces pointing towards the migration directions. However, experiments show exactly the opposite, namely that cell monolayers exert contractile stress. At first glance, this sounds contradicting, however, similar to the migration of individual cells, active movement is driven by extension of broad lamellipodia supported by a highly contractile actin network. During the dynamics of collective migration it has been also shown that tension propagates through the monolayer in the form of mechanical waves (144). In summary, the achieved results of the discribed studies suggest a strong influence of cellular mechanics in collective cell migration of monolayers based on cell-cell and cell-matrix interaction.
A prominent feature in the early stage of collective cell migration is the occurrence of so-called leader cells (139). These are cells located at the sheet periphery, which show a highly active lamellipodium and that tend to spontaneously start migrating. Since these cells seem to initiate collective migration process, their emergence is suggested to play an important role for coordinated movement. The actual process how cells are triggered to become leader cells is not well understood yet. It is further an open question to what extend geometrical aspects influence this phenomenon.

We start this chapter with an overview about cell contraction models applied in the context of cell and tissue mechanics. Subsequently, we describe two studies, which we have carried out using thermoelastic tissue and cell contraction modeling. In the first part, we examine the formation of leader cells in epithelial cell monolayer colonies with controlled geometry. Here, different colony geometries have been established by means of the mentioned micro stencil technique. In a combination of cell morphology observations, applied traction force microscopy, and thermoelastic cell monolayer contraction modeling, we could show that the distribution of intercellular tension promotes the formation of leader cells as areas of increased traction stress. We found that global

colony contraction can describe the accumulation of traction stress at largely curved edge regions. In a second study we approached a biologically very different situation by simulating the early stage of metastatic tissue invasion with thermoelastic modeling of cell-substrate interaction. Here, the cell body is modeled a contracting elastic continuum rigidly coupled to a passive elastic substrate material. The results from this study suggest that an optimal 3d cell geometry exists for highest substrate indentation and can be identified as function of the stiffness ratio of cell and substrate.

4.1 Overview: Cell & Tissue Contraction Modeling

There is a broad range of literature concerning mechanical cell and tissue contraction models. This incorporates different levels of detail, from simple isotropic static models up to complex dynamic model. One can roughly distinguish two model classes: network and continuum models. Recalling chapter 3, we already used an active cable network model to describe cellular contraction. This model was introduced by Bischofs et al. (93) and further developed by Guthard Torres (94, 100). A preliminary version of this model type was originally proposed by Stamenovic et al. (146) in terms of pre-stressed cable networks, where network contraction is induced by shortening the resting length of the network links (147, 148). Also hookean spring networks found application, however, these networks were not able to reproduce correct cell shapes on micropatterned substrates (93, 94). Network models are predominantly used to describe shapes of adherent cells and their mechanical properties in a two-dimensional limit. However, they are also suitable for complex extensions like shown in chapter 3. Continuum models describe the cell as continuous material. In the past complex dynamic continuum models have been established to describe the process of cellular contraction. Deshpande et al. (149) proposed a two dimensional cellular contraction model that incorporates the dynamic development of stress fibers based on the stress dynamics during contraction. Triggered by an initial "biochemical signal" contraction starts intracellular structure emerges while stressed regions are enforced by aligned structures. This allows to predict the basic distribution of actin SFs in cells adhered to micropatterned substrates (150, 151). Extensions of this model also incorporate adhesion dynamics (152) and SF formation in 3d (153). The Deshpande model contracts not inherently but uses a biochemical trigger to induce contraction. During the contraction process intracellular structural remodeling takes place, which lets the system saturate in a contracted final steady state. Because of this feature it has been referred to as "chemo-mechanical" cell model. An alternative approach, which addresses the same

level of detail, has been proposed by Venerey and Farsad (154) in terms of a four phase mixture model. Here, each position in the cell is characterized by a mixture of four constituents: cytosol, G-actin monomers, F-actin polymers, and cytoskeletal network. The model leads to a coupled system of elastic and reaction diffusion equations, which are solved in parallel for the steady state case. Also mechanosensitivity is incorporated in terms of strain and strain rate dependent SF contraction and assembly. Extensions of this model add cortical tension (155) and elastic substrates (156). This allows to recover correct cell shapes and the observed correlation of contour radius and spanning distance of adhesion points at micropatterned substrates (93). The described dynamic models allow detailed analysis about cellular mechanics, however, they also incorporate many parameters and assumptions about cytoskeletal structure formation.

In many cases coarse grained cell contraction models are sufficient to describe simple biophysical phenomena and due to the model's simplicity it is easy to point out essential physical explanation. Examples for such an approach are isotropic tension models. In chapter 3.5.1, we argued that the general limit for isotropic continuum theory is not satisfied in all cases. This is especially the case when apparently large SFs span the entire cell volume. In chapter 3.5.1 and fig 3.10, we demonstrated the limitations of isotropic network model to simulate proper traction patterns. Certainly not all cell types show large SFs, e.g. MDCK epithelial cells tend to generate few and short SFs, but nevertheless they generate measurable traction forces (157). For such situations it seems to be justified to consider isotropic contraction and simple models might give valuable insights into cell morphology and internal stress distribution. In 2d different tension models have been established to describe free concave cell shapes between to adhesion sites on micropatterned substrates, often supported by peripheral actin edge bundles. They are based on minimizing an energy functional that accounts for a surface tension (energy proportional to cell area) and a line tension (energy proportional to cell perimeter) (158). This leads to results similar to the shape of soap bubbles in 3d. The resulting kind of Laplace law predicts a constant contour radius that only depends on the ratio of both tensions. Though, in experiments it was found that the contour radius correlates with the spanning distance of the free cell edge. Starting from this observation there exist two extensions of the simple tension model. One considers an elastic line energy (93) and another an contour bending energy (159). Both give qualitatively similar results regarding their property to describe cell shape and forces (99). Furthermore, the observed discontinuous transition to star-like cell shape for large surface tension can be captured in both bases (159, 160). However, conceptually

the approaches are very different and hence result in different explanations about the mechanical origin of certain observed shapes.

Next, we consider a second class of models, which are predominately applied to describe the contraction of tissue layers. For this approach flat tissue monolayers are considered as isotropic elastic material under application of isotropic contractile stress. Conceptually this corresponds to solving a thermoelastic problem describing thermal expansion and contraction of an elastic body due to changes in temperature. A first application of such a tissue model was shown by Nelson et al. (161), who introduced a 3d thermodelastic model for small geometrically constrained coherent cell colonies. Their model considers a contractile layer on top of a passive layer, which is again rigidly coupled to a stiff surface. Subsequent numeric calculation of the problem revealed the shear stress distribution at the interface between both connected layers. They found that highly curved boundary regions show increased traction stresses and that these spatially correlate with regions of increased cell growth rates in the colony. The study was a proof that geometry influences cell proliferation via cell-substrate interaction. Afterwards a corresponding simpler 2d model was proposed by Edwards and Schwarz (107), which predicted the displacement and stress distribution in cell monolayers coupled to an elastic foundation. Here, the thermoelastic problem is considered in 2d plane stress approximation and the contracting layer is connected to a bed of linear elastic springs. In case of a constant thermal pressure distribution and circular monolayer shapes they found an analytic solution predicting maximal monolayer displacement at the edge part decaying towards the center, which is the location of maximal elastic monolayer stress. A quite similar model was proposed by Banerjee and Marchetti (106), where they extended the model by finite substrate elasticity (162). This model also agrees well with experimentally evaluated distributions of traction stress, while simulating the entire colony as contractile object (105) or single cells with elastic interaction (163).

It is clear that isotropic models are not capable of describing cellular contraction on a microscopic level, therefore their application is constrained to phenomenological studies. However, their simplicity is a great advantage compared to complex models and they require much less experimental information. Thus, they provide a powerful tool to describe cellular mechanics on a coarse grained level. In this chapter, we demonstrate thermoelastic contraction modeling considering two different situations.

4.2 Leader Cell Formation in Geometrically Constrained Cell Colonies

In this section we investigate the phenomenon of leader cell formation in collective migration of epithelial cell colonies. This kind of cells spontaneously change their morphology and start to migrate outwards. This represents the initial stage of collective cell motion. The exact mechanisms of how cells decide to become leader cells is not yet understood, although they are suggested to play an important role for starting tissue spreading, for example in wound healing. Since contractile tension in tissue is generated by each individual cell and partly transmitted to the substrate and neighboring cells, it is suggested that intercellular stress gradients might trigger leader cell formation. In the paper by Rausch et al. (164), we studied the hypothesis that leader cell formation is triggered by the distribution of intercellular tension in tissue and that it can be controlled by tissue geometry. In the experiments, MDCK cells were constrained by patterned PDMS stencils. Here cells were only allowed to grow on regions of defined geometry. A few minutes after removal of the stencil a few cells undergo morphological changes by spreading out a large lamelipodium and become leader cells.

Following our working hypothesis, we analyzed traction forces of leader cells using standard regularized FTTC according to Sabass et al. (46). For this purpose the stencil technique was combined with elastic PAA substrates similar to (142). For the preparation of the elastic substrate the protocol of Aratyn-Schaus et al. (165) was used (same as used for the experiments in chapter 3).
We patterned two different geometries depicted in fig. 4.1 (A) and (B). A circular colony shape and a circular shape with attached spikes. For a number of experiments ($N = 17$ for each shape) frequency analysis for the angular frequency of leader cells was employed, see fig. 4.1 (carried out by Sebastion Rausch, Spatz group, Heidelberg). The results show that leader cell formation is significantly increased at spike regions of the pattern (B) compared to the a homogeneous frequency distribution on purely circular patterns (A).

In the reconstructed traction fields the underlying geometries still can be identified as regions, that show a crowded distribution of traction hot spots, see fig. 4.2. The corresponding traction directions (arrows in (A)+(B)) indicate stress gradients between neighboring cells and that an apparent part is balanced via local substrate interactions.

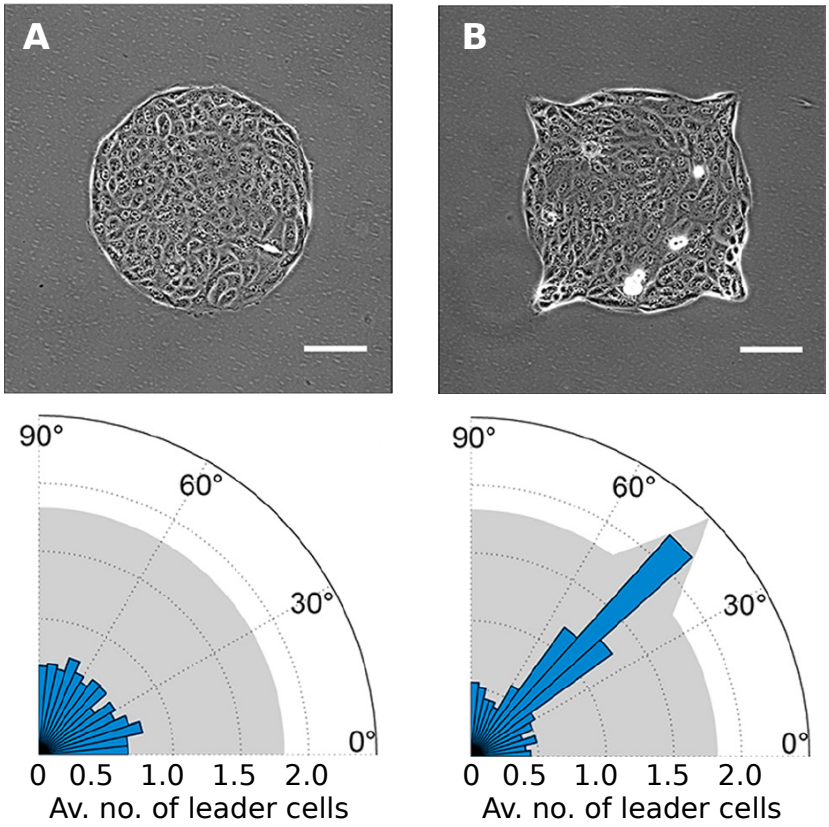

Figure 4.1: Cell collectives with defined geometries. (A) Circular cell collectives (top) show a uniform averaged angular frequency of lead cells after stencil removal (down). (B) Cell collective with locally increased curvature (top). Average angular frequency is peaked at orientations associated with higher curvature (down). Scale bar 100 μm. Images taken from (164).

Thus each cell contracts individually and the fraction of stress transmitted to the underlying substrate varies. Unfortunately, on the level of single colony traction fields it is hard to determine a clear result about the differences in both geometrical examples.

We switched to a mean field picture by using the feature of controlled geomtry calculating a mean traction field based on a group of cell colonies ($N = 17$), which share the same geometry. For this purpose, we first aligned the phase contrast images of all colonies to the same reference geometry using image registration. In a second step we applied corresponding rotation and translations to the measured bead displacement field. After the alignment, we applied regularized FTTC to reconstruct the traction fields for each colony. Here, we used a regularization parameter value of $\lambda = 1 * 10^{-5}$ for all reconstructions. After this calculation step the results were merged by determining a mean traction field. Thereby, we calculated the vectorial sum at each traction node and afterwards divided the result by the number of colonies, $\bar{T}_i^{nodal} = 1/N \sum_{n=0}^{N} T_i^n$,

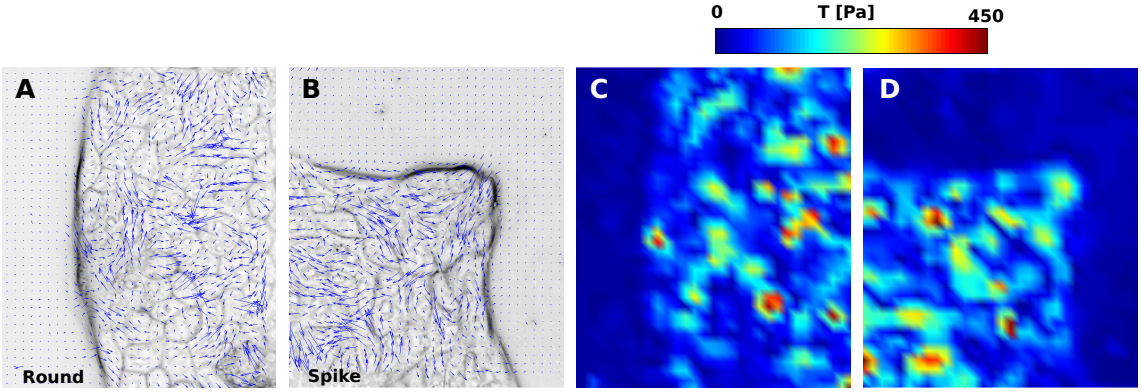

Figure 4.2: Exemplary traction reconstruction of colony traction fields (cutout) for round and spike shapes. (A)+(B) Reconstructed traction vectors for both cases. Arrow length and direction indicate traction magnitude and direction. (C)-(D) Heat map of traction magnitudes. Scaling of traction magnitudes are according to the depicted color bar. Regularization parameter $\lambda = 1 * 10^{-5}$

where i is the index of the spatial component, n indicates the colony index, and $\bar{T}_i^{nodal}$ corresponds the nodal mean traction in direction i. Since we utilized the vectorial sum, we expected to reduce these parts of the traction field according to random directions.

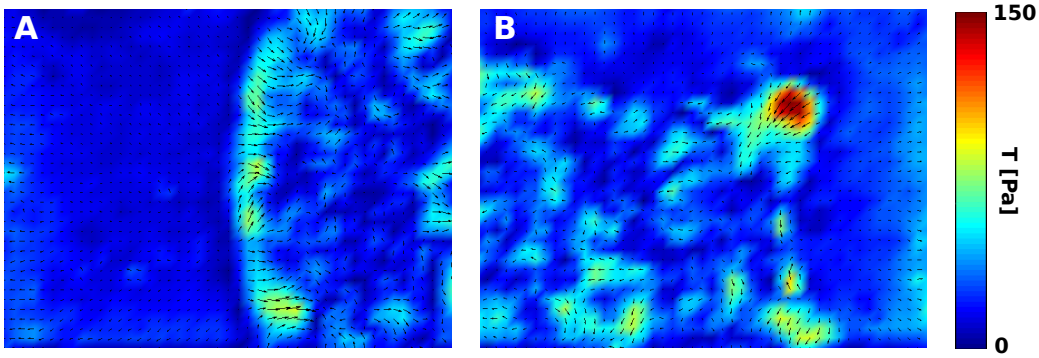

Figure 4.3: Mean traction field calculated for round and spike shaped colonies ($N = 17$,each). Mean tractions were calculated by averaging over the nodal vectorial sum. (A) Mean traction for round shaped colonies. (B) Mean traction for spike shaped colonies. Traction magnitudes are color coded and vector orientation indicate traction directions.

Fig. 4.3 shows the calculated mean traction fields for round and spike shaped colonies. Compared to the exemplary single colony traction fields depicted in fig. 4.2, the mean traction is smoothly distributed at the edge and as expected random traction within the colony is repressed. Since single colony traction hot spots are mostly randomly distributed and surrounded by area of less traction, spatial averaging leads to an overall reduction in the traction magnitude regarding the mean field. However, comparison of both cases, round and spike shaped, yields a clear picture with respect to the dis-

tribution of traction stresses. In case of spike shapes we found clearly increased mean traction stresses near the spike tip (B) compared to the circular case, where traction is homogeneously distributed over the edge (A). The relative difference in the mean traction magnitude is about 40%. This indicates that traction is on average accumulated at regions of high curvature. The result agrees with the working hypothesis since the derived mean tractions depend on the geometry. The accumulation of traction stress at the peripheral region hints to a non-local intercellular stress propagation that concentrates traction stresses at regions of high curvature.

We tested the hypothesis that intercellular stress propagation induces the traction stress accumulation by simulating colony contraction for both experimentally evaluated geometries. For this purpose we utilized the thermoelastic plane stress approach proposed by Edwards and Schwarz (107). We modeled the colony as an isotropically contracting material coupled to an elastic foundation. In case of tissue monolayers, the plane stress approximation is justified since the lateral colony extension (a few hundred μm) is much larger than its thickness ($1 - 3\mu m$). As simplest assumption for incorporating elastic interaction with the substrate, we considered the material to be connected to a bed of linear elastic springs. This leads to a harmonic body force in Cauchy's momentum equation, while we defined the strength of the elastic coupling via a coupling constant κ. Comparing the original paper by Edwards and Schwarz (107), κ can be associated to a effective spring constant k and a number density N via the relation $\kappa = kN$. The corresponding elastic momentum equation reads:

$$\nabla \cdot \sigma - \kappa \mathbf{u} = 0 \tag{4.1}$$

σ is the material Cauchy stress that consists of two parts, the internal elastic stress σ_{el} and the applied isotropic thermal contraction stress σ_{con}. The combined stress tensor in index notation reads:

$$\sigma_{ij} = \underbrace{\frac{Eh}{1+\nu}\left(\epsilon_{ij} + \frac{\nu}{1-\nu}\epsilon_{kk}\delta_{ij}\right)}_{\sigma_{el,ij}} + \underbrace{\sigma_{con}\delta_{ij}}_{\sigma_{con,ij}}. \tag{4.2}$$

E and ν are the Young's modulus and Poisson ratio of the layer, h is the layer height, and ϵ is the two-dimensional strain tensor. For the numeric calculation we used the nonlinear definition of the strain in terms of eq. (1.53) instead of its linearized form. Since we consider homogeneous contraction of the colony, σ_{con} is constant over the

entire colony area. Hence, the resulting gradient $\nabla\sigma_{con}$ becomes zero, when evaluating the momentum equation (4.1). The contraction stress σ_{con} enters the equations only as pressure boundary condition. We took the Young's modulus of the colony of MDCK cells from the literature (166), where a value of $E = 400\ Pa$ was evaluated in atomic force microscopy indentation measurements. A Poisson ratio of $\nu \approx 0.5$ is as well in agreement with this study as well. We solved the equation system eq. (4.1), (4.2), (1.53), with respect to the displacement field using the finite element software COMSOL-Multiphysics (Version 4.1).

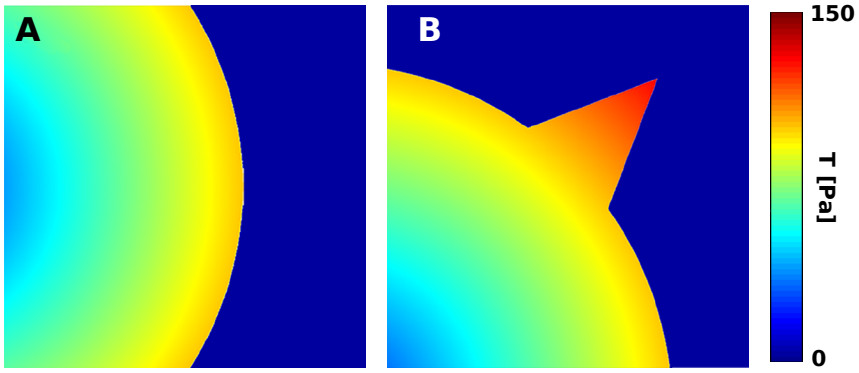

Figure 4.4: Traction fields based on thermoelastic modeling. (A) Circular shape, with homogeneous distributed traction at the colony edge. (B) Spike shape, increased traction stress at the tip region. Fit parameters: $\sigma = 3.8\ \frac{pN}{\mu m}$, $\kappa = 120 \frac{pN}{\mu m^3}$.

In order to adjust the simulations to the experimental results, we fitted the contraction stress σ_{con} and the coupling constant κ with respect to the maximal determined displacement and traction of the spike shaped data set. The traction stress was calculated from the displacement field $\mathbf{u}(\mathbf{x})$ solution via the relation $\mathbf{T}(\mathbf{x}) = \kappa\mathbf{u}(\mathbf{x})$. The best fitting parameter combination corresponded to $\sigma = 3.8\ \frac{pN}{\mu m}$ and $\kappa = 120 \frac{pN}{\mu m^3}$. The resulting simulated traction fields are depicted in fig. 4.4. In case of both geometries the traction stress shows a positive gradient reaching its maximum at the rim. This is in agreement with the experimental mean traction stress and the picture that single cell contractility stress propagates towards peripheral regions. The strongest accumulation of traction stress can be observed on the spike pattern near the spike tip, see fig. 4.3 (B). In case of the circular pattern, the traction stress is increased near the edge part, however, with lower magnitude and without a distinct spot, see fig. 4.3 (A).
The combination of angular frequency analysis of leader cell formation (fig. 4.1), traction force measurements (fig. 4.3) and modeling of colony contraction (fig. 4.4) led

to the conclusion that leader cell formation is influenced by collective mechanical cell-cell and cell-substrate interactions. A distinguished evidence for this is the increased leader cell formation at edge regions with increased curvature. By simulating tissue monolayer contraction with a thermoelastic model we contributed the connection between intercellular stress generation and propagation and measurable traction forces. From this we conclude that global tension generation and propagation led to increased cell-matrix stress at peripheral regions. Since regions of increased mean traction stress and leader cell formation match each other, we conclude that collective mechanical stress promotes the formation of leader cells and eventually influences the initiation of collective cell migration. In summary, here we showed an exciting example for the importance for mechanical interactions in cell-cell communication and how simple tissue contraction simulation can help to interpret experimental results. In the subsequent section, we investigate the secondly mentioned phenomenon of tissue invasion by cancer cells during metastasis. Here, we will highlight how cell geometry and mechanics could promote the invasion process by means of a thermoelastic cell contraction model.

4.3 3D Single Cell FEM Model

The process of metastasis demands cells with special mechanical properties. During metastasis these malignant cancer cells need to detach from the tumor, survive in the circulatory system for a certain time, and finally invade healthy tissue in order to form a new tumor. For the last step, the cancer cell has actively penetrate the tissue. In experiments, it was observed that malignant human mammary gland epithelial cancer cells show different CSK assembly dependent on their metastatic potential (167). When these cells are seeded on soft Polyacrylamid gels ($E = 1.2 - 2.3\ Pa$) they start to actively indent the substrate surface (135), see fig. 4.5. Here, the penetration strength positively correlates with the metastatic potential of the cancer cell. Together this suggests that this active cell behavior represents a starting event for tissue invasion. We applied cell contraction simulations to investigate two essential questions: is there an optimal cell geometry that promotes substrate indentation and how does the indentation strength changes with the ratio of substrate and cell stiffness.

The mentioned adherent metastatic cancer cells adopt an approximately round shape in lateral direction indicating no lateral polarization direction of the CSK. Further, the actin CSK shows usually less SFs but, however, a prominent network of microtubles. We assumed that the substrate indentation is a result of isotropic cell contraction and

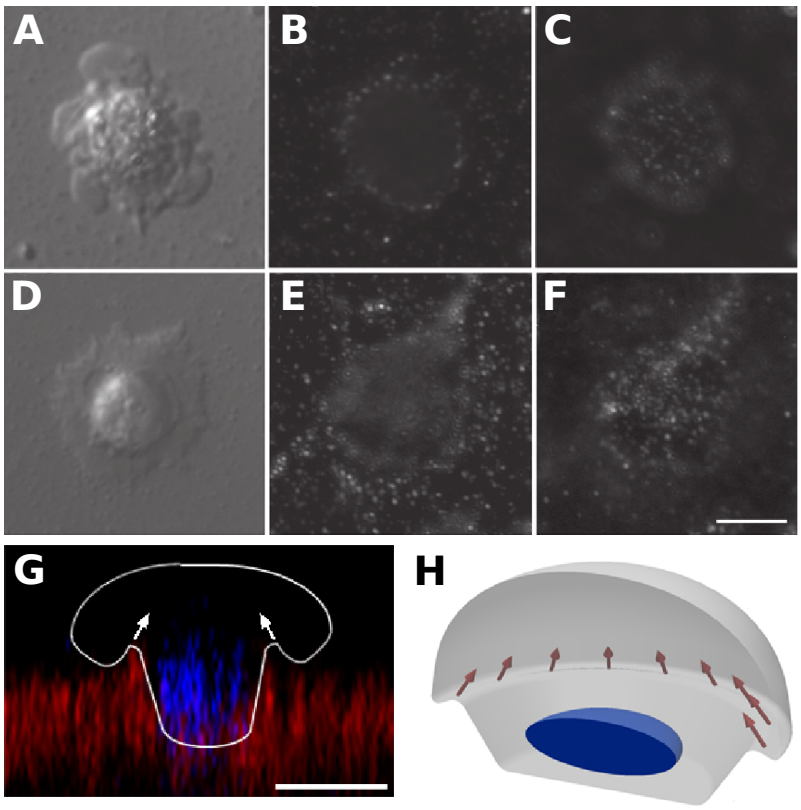

Figure 4.5: Malignant breast cancer cells cultivated on soft elastic PAA substrates ($E = 2.3\ kPa$). Two different cell morphologies are observed, (A) Bleb and (D) Skirt-like morphology. Substrate indentation is visualized by embedded marker beads. Comparison of two focal planes (Gel-surface focal height and under the cell out of focus), (B)-(C) and (E)-(F), indicate substrates indentation. Scalebar 10 μm. (G) Confocal image of a cell indenting the substrate, scalbar 5 μm. (H) Illustration of observed mushroom-like cell morphology after indentation. Images taken from (135) and slightly modified.

applied a 3d thermoelastic FEM modeling approach. For this purpose, we simulated the contraction of a spheroid coupled to an elastic substrate. We used the same definition for the Cauchy stress as for the cell colonies above, however, the corresponding tenor quantities include now a z-component. This setup requires a pressure profile at the interface between cell (contracting material) and substrate (passive material) since here derivatives of the contraction stress $\nabla\sigma_{con} \neq 0$ appear in the momentum equation. We treat this problem numerically by considering a small stress gradient across the cell-substrate interface. This is achieved by assigning the contraction stress half-and-half to cell interface surface elements and substrate interface surface elements. As a consequence of this treatment the numerically calculated displacements at the interface represent a mean elastic response between cell and substrate. This especially accounts when the stiffness ratio is different from one. Due to this numeric treatment, we

expected reduced accuracy at the interface since it depends on the actual artificial stress gradient. However, we know that the z-displacement monotonically decays with increasing substrate depth after crossing the interface and we therefore approximate the maximal indentation a few micrometer below the substrate surface (5 μm).

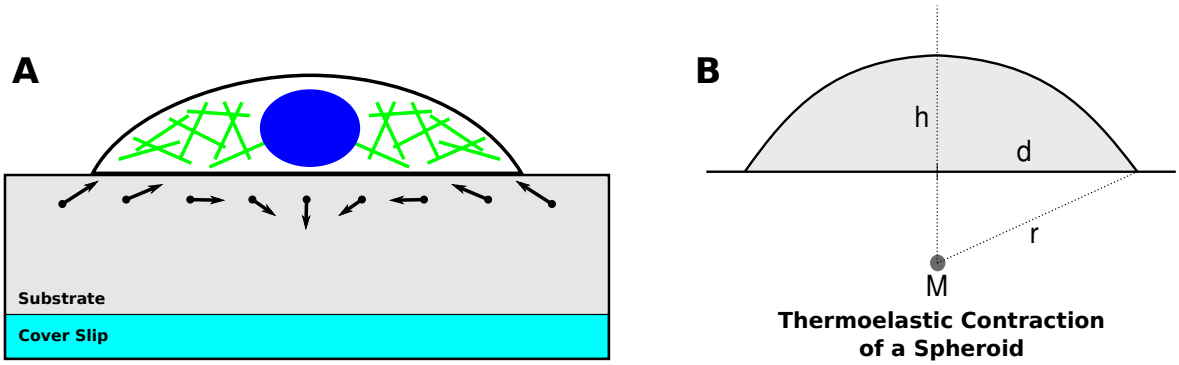

Figure 4.6: Deformations in normal direction induced by cellular contraction. (A) Illustration: cell adhered to planar substrate with actin CSK (green), Nucleus (blue), and expected substrate displacements in the xz-plane. (B)

In order to study the influence of substrate stiffness and cell geometry, we varied both aspects individually. In detail, we parameterized cell geometry as illustrated in fig. 4.6 (B). We consider the cell body as spherical section with a fixed volume V (volume constraint). The only remaining free parameter that determines cell shape and cell-substrate contact area is the section height h. The motivation for a fixed volume constraint is that cells are nearly incompressible since the largest volume part of the cell consists of the cytosol and they usually do not change the size of their volume much. Compared to that the cell highly controls contact area by assembling cell-matrix contact often adopting a flat shape far away from the spherical minimal surface. We roughly estimated the typical cell volume by $V_{cell} = 5000\ \mu m^3$, which agrees with an intermediate area of U2OS cells (compare e.g. fig. 3.11), considering a cell height of $2\mu m$. We explicitly controlled the geometry of the cell by changing the height h of the spherical section. For the given constant volume constraint the height of the corresponding hemisphere is determined by $h_{hemi} = \sqrt[3]{\frac{3V}{2\pi}} = 13.36\ \mu m$. It marks the boundary between flat cell shapes $h < h_{hemi}$ and more bubble-like shapes $h > h_{hemi}$. Due to the fixed volume constraint the contact area of the cell depends on the spherical section height h by the geometric relation $A = \frac{2V}{h} - \frac{h^2}{3}$.
In our subsequent simulations we sampled the range between $h_{min} = 5.3\ \mu m$ and $h_{max} = 15.8\ \mu m$, which corresponds to a contact area range from $A_{min} = 371\ \mu m^2$ to $A_{max} = 1857\ \mu m^2$. As typical cell stiffness we assumed $E_{cell} = 10\ kPa$. The substrate stiffness was varied from 0.1 to 2 E_{cell}. For both, substrate and cell we considered

a poisson ratio of $\nu \approx 0.5$, which reflects their nearly incompressible nature. The contraction strength was controlled by the contraction stress σ_{con}. This value was chosen in such a way that the maximal substrate displacement in the simulation (with substrate stiffness $E_{sub} = E_{cell}$) reached a value of $|u| \approx 1\ \mu m$, which turned out to be around $p \approx 30\ kPa$. In order to avoid substrate boundary effects, we further chose a lateral size of the substrate sample an order of magnitude larger than the contact area of the hemispheric shape $2 * r_{max}$, $w = 200\ \mu m$. The substrate thickness was further set to 60 μm, which is a typical value for experiments on elastic substrates.

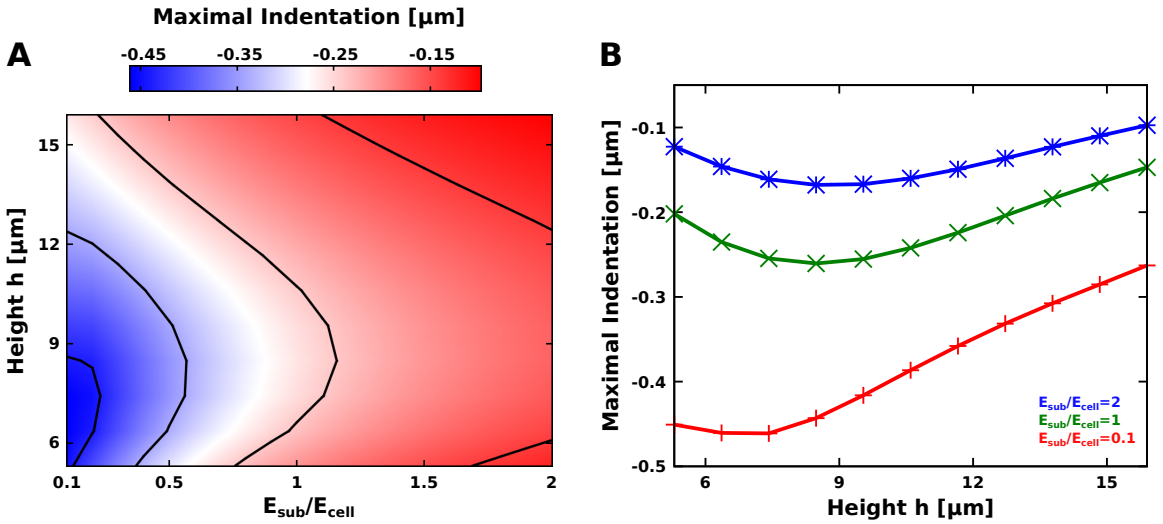

Figure 4.7: Maximal simulated indentation depth as function of cell shape and substrate stiffness. The axes describe the substrate stiffness normalized by the cell stiffness and the relative cell height h_{rel}. $h_{rel} < 0$ equals to a flat shape, $h_{rel} = 0$ corresponds to a hemisphere, and $h_{rel} > 0$ bubble shape. Black lines represent contours of constant indentation. Maximal indentation is predicted for a soft substrate and a flat cell shape optimal in the region around $h_{rel} = 7.5\ \mu m$.

The results of the simulation analysis over the defined parameter range are depicted in fig. 4.7. In (A) the maximal determined substrate indentation is plotted over the substrate stiffness (normalized by the cell stiffness) E_{sub}/E_{cell} and spherical section height h. By analyzing the heat map, we found that the deepest indentation is achieved when the substrate is much softer than the cell and the reference cell shape is flatter than the hemispheric shape ($h \approx 7.5 \mu m$). From a physical point of view it is clear that in both extreme cases, $h \to 0 \Rightarrow A \to \infty$, and $h \to \sqrt[3]{\frac{3V}{\pi}} \Rightarrow A \to 0$, the substrate indentation depth approaches zero. Therefore, we expect to find a distinct minimum. Also the mechanical effect of the substrate stiffness can be explained. Both materials are nearly incompressible and they only differ in their Young's modulus. By contracting of the cell volume with an applied isotropic stress, shear modes dominate and in order to satisfy the incompressibility constraint it is easier to push cell volume out into

the substrate material like pushing out a cherry stone. In fig. 4.7 (B) we plotted the indentation depth over the spherical section height for three different stiffness combinations (E_{sub}/E_{cell}): soft/stiff, equal, and stiff/soft. Each curve shows a distinct indentation optimum as expected, but interestingly the optimum shifts with increasing substrate stiffness towards larger section heights. The largest indentation appears on the soft substrate with $h \approx 7.5\ \mu m$ corresponding to a contact area of $A = 1274\ \mu m^2$. In case of stiff substrates the optimal height increased to a $h \approx 9\ \mu m$, which corresponds to a contact area of $A = 1026\ \mu m^2$.

In summary, we found that substrate stiffness and cell geometry commonly influence substrate indentation achieved by the cell. Soft substrates promote indentation and the cell can adopt an optimal shape to achieve largest possible indenation. However, both aspects are coupled, since the optimal geometry shifts with the substrate stiffness towards larger spherical section heights. Often, it is much easier to determine cellular contact area in experiments. If the cancer cell adopts an optimal shape for substrate penetration, the simple thermoelastic model predicts a smaller contact area for cells on stiffer substrates compared to soft substrates. From experiments it is known that metastatic cancer cells tend to soften compared to their normal corresponding cell type (168, 169). This seems to contradict to the optimal indentation picture. However, it is also known that metastatic cell adapt their cytoskeleton in a highly dynamic fashion (167). This becomes clear if we recall their property to on the one hand survive in the circulatory system without adhesion and on the other hand to establish an adherent state associated with strong contractile forces. In order to achieve this the CSK has to provide a certain degree of flexibility and thus also to dynamically change the effective cell stiffness.

4.4 Summary & Discussion

In this chapter, we addressed two biologically relevant cases for which geometry and cellular contraction plays an important role: leader cell formation in epithelial tissue monolayers and tissue invasion by cancer cells. Both are complex dynamic processes, however, at the initial state tensional homeostasis exists from which the mentioned events start. The description of cellular contraction in the steady state limit is thus capable to illuminate the effect of cell and tissue geometry. In the introduction, we gave a detailed review of the rich literature of cellular mechanical models ranging from simple static network models to complex continuum models numerically treated with FEM. For the examined cases we used a powerful class of simple thermoelastic

models to account for tension and deformation within tissue and cells adhered to elastic substrates. In the first study, we studied the case of epithelial cell sheets constrained to geometries of different boundary curvature. By studying cell morphology, substrate traction stresses, and thermoelastic contraction modeling, we found that the formation of leader cells at the early stage of collective cell migration is influenced by geometry and that collectively generated traction stresses can trigger leader cell formation. This highlights the importance of mechanical signals to initiate highly coordinated dynamic processes, not only on a single cell level, but also on the tissue level. In a second study, we simulated the substrate indentation by adherent cells. Here, we addressed the medically relevant case of malignant metastatic cancer cells, which try to invade healthy tissue. Experiments on elastic substrates suggest that these cells adhere to the tissue surfaces and actively push their cell body into the tissue volume. We modeled the early stage of this process by thermoelastic contraction of a spheroidally shaped cell rigidly attached to an elastic substrate surface. By varying cell geometry and elasticity of the substrate, we found optimal cell geometries to achieve maximal substrate indentation. Interestingly, we found that the optimal cell geometry shifts with the ratio of cell and substrate stiffness from a flat shape to a more hemispheric shape. Considering the case that these cells try to adopt an optimal shape for a given substrate stiffness and that the model considerations are sufficient, the simulation predicts decreasing cell area with increasing substrate stiffness, which can be tested experimentally.

5

Summary and Outlook

The objective of this thesis is to investigate the mechanics underlying the generation and spatial distribution of mechanical forces of tissue cells adhering to their environment. In detail we focused on two questions: how environmental geometry alters cellular force generation and cell fate, and how cells control generation and distribution of contractile tension applied to the extracellular space. Earlier studies focused on local events like the maturation of single focal adhesion (FAs) (90, 91) or cutting of individual stress fibers (SFs) (170). Here, we develop a more global picture on a whole cell level. To achieve this goal, we developed two novel traction force microscopy techniques, which improve current state of the art techniques, and simulated traction forces exerted by single cells and tissue monolayers by means of continuum elasticity theory.

In chapter 2 we described a technique that enables us to reconstruct traction forces of cells adhered to non-planar substrates. With the purpose to quantitatively study the influence of substrate topography on cellular mechanics, here, we developed a 3d FEM-based traction reconstruction approach, which is not restricted to planar substrates. The core of this method is a combination of effective finite element calculation and parameter optimization. To fulfill the special demands of a 3d technique regarding local resolution and robustness against noise in measured bead displacement fields, we introduced adaptive local mesh refinement and robust statistical estimates into the traction reconstruction process. The validation of the method was established by extensive reconstruction of simulated data and comparison with state of the art techniques on planar substrates. We demonstrated the successful application of the method for experimental data of cardiac myofibroblast adhered of substrates with different topographies. Although dealing with a low statistics at the current state of the project, our preliminary results hint to a reduced cellular contraction on non-planar compared

to the planar situation.

In chapter 3, we addressed the intracellular origin of cell traction forces and their correlation with cellular properties. For this purpose, we introduced the novel concept of model-based traction force microscopy (MB-TFM). The central element of this technique is the incorporation of quantitative cell modeling into the process of traction reconstruction. We showed that this provides multiple advantages compared to traditional traction reconstruction. Firstly, we could demonstrate the recovery of well-posedness of the reconstruction problem involving an active cable cell model. This allowed us to reconstruct traction patterns independent of regularization parameters. Secondly, by introducing additional experimental information into the reconstruction process in terms of distribution of FAs and SFs, we could effectively improve the traction resolution based on bead displacement fields with common resolution. The third and most prominent feature of this technique is that the incorporated cell model facilitates correlation analysis of obtainted forces and intracellular structure. By evaluating experimental data, we found that on average $\sim 90\%$ of the overall traction forces exerted by U2OS cells is generated by SF contraction and only $\sim 10\%$ by actin network contraction. Thereby SF-generated forces correlate positively with the number of FAs and SFs, while the actin network provides an uncorrelated force background. Comparison of single FAs connected and unconnected to SFs reveals that connected ones bear larger forces, which are also positively related to FA area. The most important result of this study was achieved by analyzing the tension within single SFs. We obtained force distributions for different SF types based on a large statistics ($N_{SF} = 369$ for $N = 14$ U2OS cells), which has not been achieved before to our knowledge. The force distributions for dorsal SFs, ventral SFs, and transverse arcs show significantly different shapes. In agreement with their molecular assembly, we found that ventral stress fibers bear predominantly larger forces compared to dorsal stress fibers, and transverse arcs represent an intermediate state regarding their contractile strength. We verified the significance of the result by cross-correlation with simulations applied to a single data set. This confirmed that the obtained single SF force distributions are not only valid when we average over multiple cells but also on the level of single cells.

In chapter 4, we applied concepts from thermoelasticity theory to model cellular traction forces regarding two biologically relevant situations. In the first part we investigated the influence of traction forces and tissue geometry for leader cell formation in epithelial cell tissue layers. Leader cells play a crucial role for initiation of collective cell migration important e.g. in wound healing. We found that leader cell formation can be triggered by the given geometry in the sense that leader cell formation is

strongly increased at edge regions with variation in curvature (164). Subsequently we addressed the hypothesis that geometrically induced traction stress triggers the formation of leader cells. Therefore we applied traction force microscopy and found regions of increased mean traction stress in the vicinity of higher edge curvatures. With a two dimensional thermoelastic plane stress model introduced before by Edwards and Schwarz (107), we were able to qualitatively recover the experimental findings. From the model results and the experimental findings, we concluded that cellular tension is not only locally balanced between neighboring cells, but tension is further globally distributed mediated via cell-cell junctions. We propose that globally generated tension is the reason for increased traction stresses at the peripheral region while the traction strength further dependents on the colony edge geometry. This suggests that epithelial cells at the tissue edge may respond to increased traction stresses, which biases morphological changes eventually ending up as a leader cells.
In the second study, we investigated the early stage of tissue invasion by cancer cells in tumor metastasis. During the process of metastasis, malignant cancer cells leave the tumor tissue towards the circulatory system in order to invade healthy tissue. In analogy to the early stage of tissue invasion, in experiments it has been observed that malignant cancer cells actively indent planar elastic substrates (135). With a simplified thermoelastic 3d cell model, we studied the question how cell geometry and stiffness may promote tissue penetration. We simulated cell contraction with rigid coupling to a planar elastic substrate regarding different cell geometry and substrate stiffness. We found an optimal cell shape that depends on the substrate stiffness, while soft substrates in general promote indentation.
In summary the presented thesis covers a large range of questions associated with cellular traction forces with a special focus on environmental geometry and CSK structure on a whole cell level. It led to new concepts of force data analysis and valuable insights about cellular mechanics.

We conclude with an outlook for future studies based on the provided work. Regarding the issue of geometry sensing by cells adhered to non-planar substrates, much can be learned from analyzing more experimental data. In detail, we plan to investigate the mechanics of kidney podocytes in addition to cardiac myocytes, which were up to now considered. Podocytes play an important role in the filtering system of the kidney and naturally live on top of strongly curved membranes in the glomerulus (glomerular basement membrane). They are known to respond sensitively to external forces like

observed in e.g. glomerular hypertension which leads to tissue damage and eventually glomerulosclerosis (171). Regarding this it is an interesting question whether they show different mechanics on non-planar substrates compared to the planar situation and compared to other cell types. Such a study might give valuable information about special mechanical features of podocytes and possible implication for drug development.

In the future it would be also fascinating to combine non-planar elastic substrates and collective cell migration assays. A recent study by Bidan et al. (172) concerned geometric control of bone tissue proliferation in curved environments. Application of wave and groove shaped elastic substrates like introduced in chapter 2 would provide a basis for 3d tissue migration assays in which cellular forces could be associated with collective cell migration and 3d tissue proliferation in a combined manner.

Regarding the MB-TFM approach in chapter 3, there exist multiple perspectives for future studies. To ensure the flexibility of the method, we implemented the corresponding software as open source C++ library, which allows us to include different cell and substrate models into the reconstruction process. One concrete next step would be to implement tracking of FA forces and SF tensions over time. This would allow us to simultaneously study the force dynamics in growing FAs and SFs. It also might extend previous studies on the dynamic of FAs on planar substrates e.g. (91) or on pillar substrates (24). Further it is conceivable to think about a combination of non-planar substrates and MB-TFM while implementing e.g. 3d cable models (100) or continuum models of the Deshpande (149) or Vernerey type (156). Currently we work also with a "null model" MB-TFM version, which we call FA constraint optimization, where each segmented FA relates to an independent force vector. By reconstruction of simulated data this methods should enable us to determine minimal requirement for single FA force resolution by reconstruction simulated data. The considered problem is that bead density and signal to noise ratio of the data contribute both to the final resolution of the traction field. Up to now, there is no analytic way to reliably estimate the spatial resolution of obtained traction field. Therefore we envision a numerical study to identify the lower bounds for bead density and noise level required to achieve single FA resolution.

Appendix A

Model-based Traction Force Microscopy

A.1 FTTC - Force Correlations

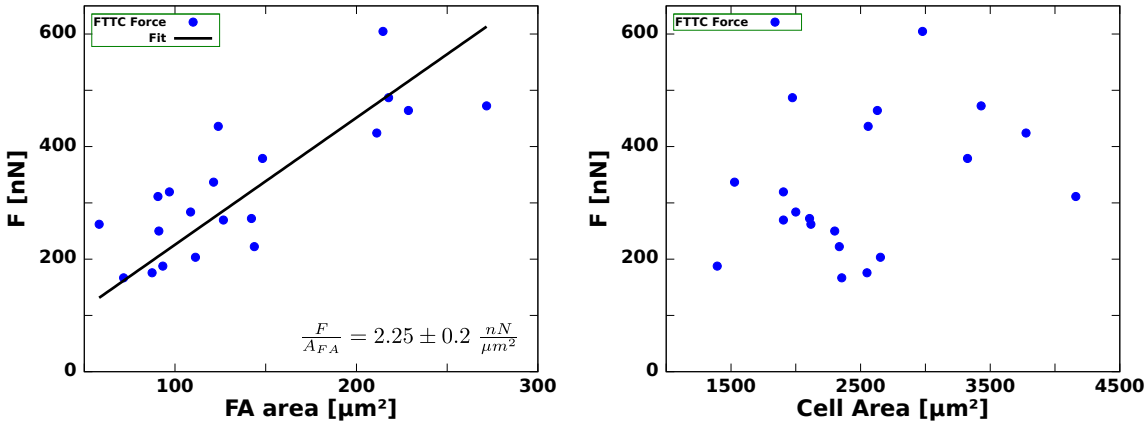

Figure A.1: Correlation of forces (reconstructed by FTTC) with FA area and cell area. Data: U2OS wildtype cells adhered to elastic PAA substrates ($E = 8.4\ kPa$).

A.2 Correlations with Number of Stress Fibers

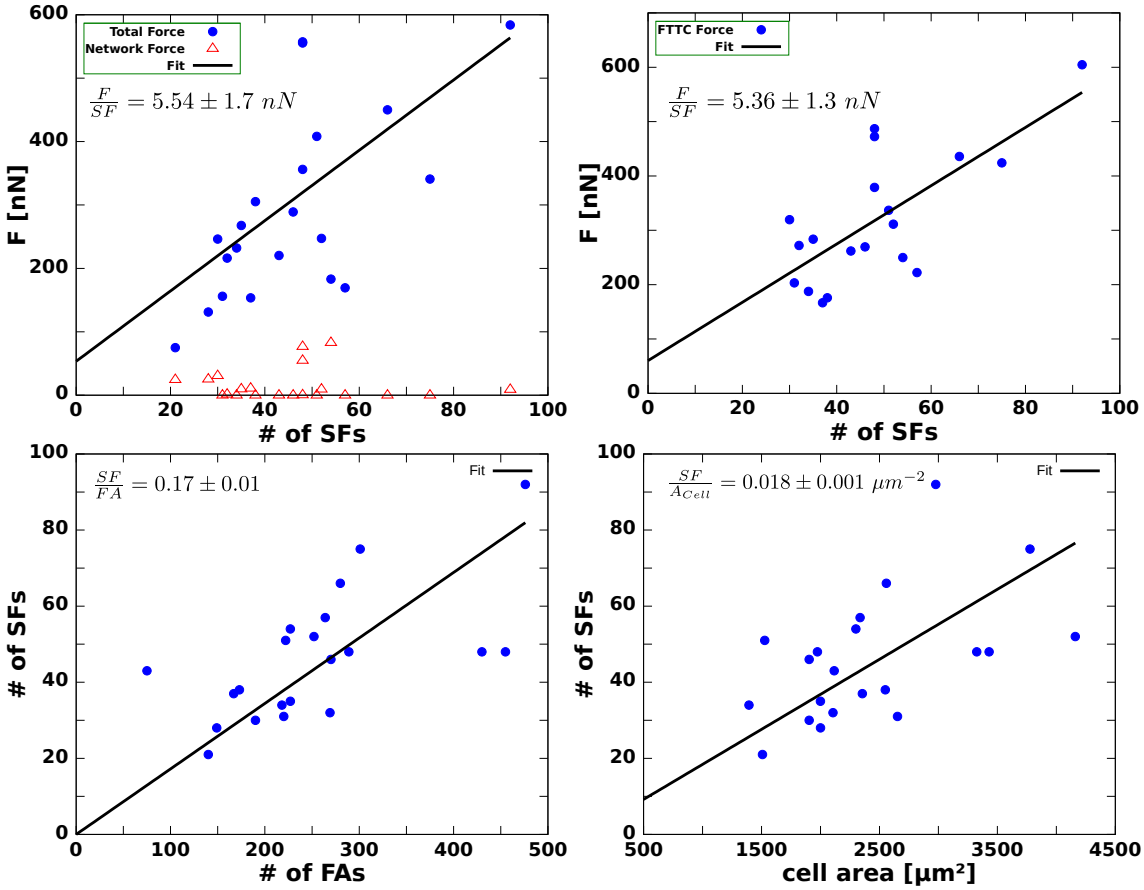

Figure A.2: Corrlation analysis regarding the number of SFs. Data: U2OS wildtype cells adhered to elastic PAA substrates ($E = 8.4\ kPa$).

References

[1] **Wikimedia Commons**. http://commons.wikimedia.org/. 2

[2] R A Brown, R Prajapati, D A McGrouther, I V Yannas, and M Eastwood. **Tensional homeostasis in dermal fibroblasts: mechanical responses to mechanical loading in three-dimensional substrates.** *Journal of Cellular Physiology*, **175**(3):323–32, June 1998. 2

[3] Christopher C DuFort, Matthew J Paszek, and Valerie M Weaver. **Balancing forces: architectural control of mechanotransduction.** *Nature Reviews. Molecular Cell Biology*, **12**(5):308–19, May 2011. 2

[4] Ulrich S Schwarz and Margaret L Gardel. **United we stand - integrating the actin cytoskeleton and cell-matrix adhesions in cellular mechanotransduction.** *Journal of Cell Science*, (July), July 2012. 2, 3

[5] Christian Frantz, Kathleen M Stewart, and Valerie M Weaver. **The extracellular matrix at a glance.** *Journal of Cell Science*, **123**(Pt 24):4195–200, December 2010. 2, 3

[6] Jessamine P Winer, Shaina Oake, and Paul a Janmey. **Non-linear elasticity of extracellular matrices enables contractile cells to communicate local position and orientation.** *PloS One*, **4**(7):e6382, January 2009. 2

[7] Bruce Alberts, Alexander Johnson, Julian Lewis, Martin Raff, Keith Roberts, and Peter Walter. *Molecular Biology of the Cell*. Garland Science, New York, 4th ed. edition, 2002. 3, 4

[8] Dennis E Discher, Paul Janmey, and Yu-Li Wang. **Tissue cells feel and respond to the stiffness of their substrate.** *Science*, **310**(5751):1139–43, November 2005. 3, 17, 57

[9] Paul a Janmey and Christopher a McCulloch. **Cell mechanics: integrating cell responses to mechanical stimuli.** *Annual Review of Biomedical Engineering*, **9**:1–34, January 2007. 3, 17

[10] Christopher S Chen. **Mechanotransduction - a field pulling together?** *Journal of Cell Science*, **121**(Pt 20):3285–92, October 2008. 3, 89

[11] Daniel a Fletcher and R Dyche Mullins. **Cell mechanics and the cytoskeleton.** *Nature*, **463**(7280):485–92, January 2010. 4

[12] Clifford P Brangwynne, Frederick C MacKintosh, Sanjay Kumar, Nicholas a Geisse, Jennifer Talbot, L Mahadevan, Kevin K Parker, Donald E Ingber, and David a Weitz. **Microtubules can bear enhanced compressive loads in living cells because of lateral reinforcement.** *The Journal of Cell Biology*, **173**(5):733–41, June 2006. 4

[13] Eric W Flitney, Edward R Kuczmarski, Stephen a Adam, and Robert D Goldman. **Insights into the mechanical properties of epithelial cells: the effects of shear stress on the assembly and remodeling of keratin intermediate filaments.** *FASEB journal : official publication of the Federation of American Societies for Experimental Biology*, **23**(7):2110–9, July 2009. 4

[14] Jonathon Howard. *Mechanics of Motor Proteins and the Cytoskeleton*. Sinauer Associates, 2001. 4

[15] Steven J Winder and Kathryn R Ayscough. **Actin-binding proteins.** *Journal of Cell Science*, **118**(Pt 4):651–4, February 2005. 4

[16] Anne J Ridley, Martin a Schwartz, Keith Burridge, Richard a Firtel, Mark H Ginsberg, Gary Borisy, J Thomas Parsons, and Alan Rick Horwitz. **Cell migration: integrating signals from front to back.** *Science*, **302**(5651):1704–9, December 2003. 4

[17] Christoph Le Clainche and Marie-France F Carlier. **Regulation of actin assembly associated with protrusion and adhesion in cell migration**. *Physiological Reviews*, **88**:489–513, 2008. 4

[18] Amanda M Hartman and James A Spudich. **The myosin superfamily at a glance**. *Journal of Cell Science*, **125**(7):1627–1632, May 2012. 4

[19] Malgorzata Barczyk, Sergio Carracedo, and Donald Gullberg. **Integrins.** *Cell and Tissue Research*, **339**(1):269–80, January 2010. 5, 59

[20] Ronen Zaidel-Bar, Shalev Itzkovitz, Avi Ma'ayan, Ravi Iyengar, and Benjamin Geiger. **Functional atlas of the integrin adhesome.** *Nature Cell Biology*, **9**(8):858–67, August 2007. 5, 59

[21] Nathalie Q Balaban, Ulrich S Schwarz, Daniel Riveline, Polina Goichberg, Gila Tzur, Ilana Sabanay, Diana Mahalu, Sam Safran, Alexander Bershadsky, Lia Addadi, and Benjamin Geiger. **Force and focal adhesion assembly: a close relationship studied using elastic micropatterned substrates.** *Nature Cell Biology*, **3**(5):466–72, May 2001. 5, 18, 43, 78, 80

[22] Jonathan Stricker, Benedikt Sabass, Ulrich S Schwarz, and Margaret L Gardel. **Optimization of traction force microscopy for micron-sized focal adhesions.** *Journal of Physics. Condensed Matter*, **22**(19):194104, April 2010. 5, 19

[23] Jianping Fu, Yang-Kao Wang, Michael T Yang, Ravi a Desai, Xiang Yu, Zhijun Liu, and Christopher S Chen. **Mechanical regulation of cell function with geometrically modulated elastomeric substrates**. *Nature Methods*, **7**(9):733–736, August 2010. 5, 43, 78, 79, 80, 86

[24] Léa Trichet, Jimmy Le Digabel, Rhoda J Hawkins, Sri Ram Krishna Vedula, Mukund Gupta, Claire Ribrault, Pascal Hersen, Raphaël Voituriez, and Benoît Ladoux. **Evidence of a large-scale mechanosensing mechanism for cellular adaptation to substrate stiffness.** *Proceedings of the National Academy of Sciences of the United States of America*, **109**(18):6933–8, May 2012. 5, 108

[25] Alexander D Bershadsky, Nathalie Q Balaban, and Benjamin Geiger. **Adhesion-dependent cell mechanosensitivity.** *Annual Review of Cell and Developmental Biology*, **19**:677–95, January 2003. 5, 81

[26] Benjamin Geiger, Alexander Bershadsky, Roumen Pankov, and Kenneth M Yamada. **Transmembrane extracellular matrix cytoskeleton crosstalk**. *Nature Reviews Molecular Cell Biology*, **2**(November):793–805, 2001. 5

[27] Benjamin Geiger, Joachim P Spatz, and Alexander D Bershadsky. **Environmental sensing through focal adhesions.** *Nature Reviews. Molecular Cell Biology*, **10**(1):21–33, January 2009. 5, 59, 81

[28] Haguy Wolfenson, Alexander Bershadsky, Yoav I Henis, and Benjamin Geiger. **Actomyosin-generated tension controls the molecular kinetics of focal adhesions.** *Journal of Cell Science*, **124**(Pt 9):1425–32, May 2011. 5, 82

[29] Karen A Beningo, Micah Dembo, Irina Kaverina, Victor J Small, and Yu-Li Wang. **Nascent focal adhesions are responsible for the generation of strong propulsive forces in migrating fibroblasts.** *The Journal of Cell Biology*, **153**(4):881–8, May 2001. 5

[30] Pakorn Kanchanawong, Gleb Shtengel, Ana M. Pasapera, Ericka B. Ramko, Michael W. Davidson, Harald F. Hess, and Clare M. Waterman. **Nanoscale architecture of integrin-based cell adhesions**. *Nature*, **468**(7323):580–584, November 2010. 6, 59

[31] Peter Howell, Gregory Kozyreff, and John Ockendon. *Applied Solid Mechanics*. Cambridge University Press, Cambridge, 2009. 6, 13, 25, 67

[32] Gerhard A. Holzapfel. *Nonlinear Solid Mechanics*. Wiley, 2006. 6, 16

[33] Javier Bonet and Richard D. Wood. *Nonlinear Continuum Mechanics for Finite Element Analysis*. Cambridge University Press, 1997. 6, 16, 37

[34] L. D. Landau and E.M. Lifschitz. *Lehrbuch der Theoretischen Physik, Elasticittstheorie*, **7**. Akademie-Verlag, 1983. 6, 13, 20, 32, 37, 52

[35] S Timoshenko and J. N. Goodier. *Theory of Elasticity*. McGraw-Hill Book Company, Inc., New York, 1951. 13, 32

[36] M. Kaliske. **On the finite element implementation of rubber-like materials at finite strains**. *Engineering Computations*, **14**(2):216–232, 1997. 16

[37] Viola Vogel and Michael Sheetz. **Local force and geometry sensing regulate cell functions.** *Nature Reviews. Molecular Cell Biology*, **7**(4):265–75, April 2006. 17

[38] Albert K Harris, Patricia Wild, and David Stopak. **Silicone rubber substrata: a new wrinkle in the study of cell locomotion.** *Science*, **208**(4440):177–9, April 1980. 17, 18, 19

[39] Albert K Harris, David Stopak, and Patricia Wild. **Fibroblast traction as a mechanism for collagen morphogenesis**. *Nature*, **290**, 1981. 17

[40] Tim Oliver, Micah Dembo, and Ken Jacobson. **Traction forces in locomoting cells.** *Cell Motility and the Cytoskeleton*, **31**(3):225–40, January 1995. 17, 18, 19

[41] John L Tan, Joe Tien, Dana M Pirone, Darren S Gray, Kiran Bhadriraju, and Christopher S Chen. **Cells lying on a bed of microneedles: an approach to isolate mechanical force.** *Proceedings of the National Academy of Sciences of the United States of America*, **100**(4):1484–9, February 2003. 17, 18, 81

[42] Juliet Lee, Michelle Leonard, Tim Oliver, Akira Ishihara, and Ken Jacobson. **Traction forces generated by locomoting keratocytes.** *The Journal of Cell Biology*, **127**(6 Pt 2):1957–64, December 1994. 18, 19

[43] Micah Dembo and Tim Oliver. **Imaging the Traction Stresses Exerted by Locomoting Cells with the Elastic Substratum Method**. *Biophysical Journal*, **70**(April 1996):2008–2022, 1996. 18, 20, 22, 67

[44] Robert J Pelham and Yu-Li Wang. **Cell locomotion and focal adhesions are regulated by substrate flexibility.** *Proceedings of the National Academy of Sciences of the United States of America*, **94**:13661–5, June 1997. 18

[45] Catherine Galbraith and Michael Sheetz. **A micromachined device provides a new bend on fibroblast**. *Proceedings of the National Academy of Sciences of the United States of America*, **94**(August):9114–9118, 1997. 18

[46] Benedikt Sabass, Margaret L Gardel, Clare M Waterman, and Ulrich S Schwarz. **High resolution traction force microscopy based on experimental and computational advances.** *Biophysical Journal*, **94**:207–220, January 2008. 19, 22, 24, 27, 41, 43, 60, 61, 67, 94

[47] Sergey V Plotnikov, Ana M Pasapera, Benedikt Sabass, and Clare M Waterman. **Force fluctuations within focal adhesions mediate**

ECM-rigidity sensing to guide directed cell migration. *Cell*, **151**(7):1513–27, December 2012. 19, 47, 60, 75, 81, 87

[48] M Dembo and Yu-li Wang. **Stresses at the Cell-to-Substrate Interface during Locomotion of Fibroblasts**. *Biophysical Journal*, **76**(4):2307–2316, 1999. 20, 22, 41, 60

[49] Curtis R. Vogel. *Computational Methods for Inverse Problems*. Society for Industrial and Applied Mathematics, Philadelphia, 2002. 21, 36, 40, 46, 60, 86

[50] Andrey N. Tikhonov and Vasiliy Y. Arsenin. *Solution of Ill-Posed Problems*. John Wiley & Sons, New York, 1977. 21, 36, 40, 47

[51] James P Butler, Iva Marija Tolić-Nø rrelykke, Ben Fabry, and Jeffrey J Fredberg. **Traction fields, moments, and strain energy that cells exert on their surroundings.** *American Journal of Physiology. Cell Physiology*, **282**:C595–605, March 2002. 22, 23, 67

[52] Ulrich S Schwarz, Nathalie Q Balaban, Daniel Riveline, Alexander D Bershadsky, Benjamin Geiger, and Sam Safran. **Calculation of Forces at Focal Adhesions from Elastic Substrate Data: The Effect of Localized Force and the Need for Regularization**. *Biophysical Journal*, **83**:1380–1394, September 2002. 21, 22, 23, 26, 27, 41, 46, 47, 60, 61, 67, 81

[53] Per Christian Hansen. **ANALYSIS OF DISCRETE ILL-POSED PROBLEMS BY MEANS OF THE L-CURV**. *SIAM*, **34**(4):561–580, 1992. 23, 47, 60, 74, 86

[54] Rudolf Merkel, Norbert Kirchgessner, Claudia M Cesa, and Bernd Hoffmann. **Cell force microscopy on elastic layers of finite thickness.** *Biophysical Journal*, **93**(9):3314–23, November 2007. 24, 52, 53

[55] Wesley R Legant, Jordan S Miller, Brandon L Blakely, Daniel M Cohen, Guy M Genin, and Christopher S Chen. **Measurement of mechanical tractions exerted by cells in three-dimensional matrices.** *Nature Methods*, **7**(12), November 2010. 24, 26, 27, 46

[56] Davide Ambrosi. **CELLULAR TRACTION AS AN INVERSE PROBLEM**. *SIAM Journal for Applied Mathematics*, **66**(6):2049–2060, 2006. 24, 25

[57] D Ambrosi, A Duperray, V Peschetola, and C Verdier. **Traction patterns of tumor cells.** *Journal of Mathematical Biology*, **58**(1-2):163–81, January 2009. 24

[58] Sung Sik Hur, Yihua Zhao, Yi-Shuan Li, Elliot Botvinick, and Shu Chien. **Live Cells Exert 3-Dimensional Traction Forces on Their Substrata.** *Cellular and Molecular Bioengineering*, **2**(3):425–436, September 2009. 25, 27, 43

[59] Sung Sik Hur, Juan C Del Álamo, Joon Seok Park, Yi-Shuan Li, Hong a Nguyen, Dayu Teng, Kuei-Chun Wang, Leona Flores, Baldomero Alonso-Latorre, Juan C Lasheras, and Shu Chien. **Roles of cell confluency and fluid shear in 3-dimensional intracellular forces in endothelial cells.** *Proceedings of the National Academy of Sciences of the United States of America*, **109**(28):11110–5, July 2012. 25

[60] Wesley R Legant, Colin K Choi, Jordan S Miller, Lin Shao, Liang Gao, Eric Betzig, and Christopher S Chen. **Multidimensional traction force microscopy reveals out-of-plane rotational moments about focal adhesions.** *Proceedings of the National Academy of Sciences of the United States of America*, **110**(3):881–6, January 2013. 27, 60

[61] Adam Curtis and Chris Wilkinson. **Topographical control of cells.** *Biomaterials*, **18**(24):1573–83, December 1997. 31, 78

[62] Christopher J Bettinger, Robert Langer, and Jeffrey T Borenstein. **Engineering substrate topography at the micro- and nanoscale to control cell function.** *Angewandte Chemie (International ed. in English)*, **48**(30):5406–15, January 2009. 31

[63] Deok-Ho Kim, Paolo P Provenzano, Chris L Smith, and Andre Levchenko. **Matrix nanotopography as a regulator of cell function**. *The Journal of Cell Biology*, **197**(3):351–360, April 2012. 31

[64] Sarah a Biela, Yi Su, Joachim P Spatz, and Ralf Kemkemer. **Different sensitivity of human endothelial cells, smooth muscle cells and fibroblasts to topography in the nano-micro range.** *Acta Biomaterialia*, **5**(7):2460–6, September 2009. 31

[65] Jospeh M Corey and Eva L Feldman. **Substrate patterning: an emerging technology for the study of neuronal behavior**. *Experimental Neurology*, **184**:89–96, November 2003. 31

[66] T.M. Svitkina, Y.A. Rovensky, A.D. Bershadsky, and J.M. Vasiliev. **Transverse pattern of microfilament bundles induced in epitheliocytes by cylindrical substrata**. *Journal of Cell Science*, **108**(2):735, February 1995. 31, 57

[67] Roy M. Smeal, Richard Rabbitt, Roy Biran, and Patrick a. Tresco. **Substrate Curvature Influences the Direction of Nerve Outgrowth**. *Annals of Biomedical Engineering*, **33**(3):376–382, January 2005. 31

[68] José a Sanz-Herrera, Pedro Moreo, José M García-Aznar, and Manuel Doblaré. **On the effect of substrate curvature on cell mechanics.** *Biomaterials*, **30**(34):6674–86, December 2009. 31

[69] Casey M Kraning-Rush, Joseph P Califano, and Cynthia a Reinhart-King. **Cellular traction stresses increase with increasing metastatic potential.** *PloS One*, **7**(2):e32572, January 2012. 31, 78

[70] Younan Xia and Whitesides George M. **Soft Lithography**. *Annual Review of Material Sciences*, **28**:152–84, August 1998. 34

[71] Ovidiu D Gordan, Bo N J Persson, Claudia M Cesa, Dirk Mayer, Bernd Hoffmann, Sabine Dieluweit, and Rudolf Merkel. **On pattern transfer in replica molding.** *Langmuir : the ACS Journal of Surfaces and Colloids*, **24**(13):6636–9, June 2008. 34

[72] Herbert Edelsbrunner, David G. Kirkpatrick, and Raimund Seidel. **On the Shape of a Set of Points in the Plane**. *IEEE Transactions on Information Theory*, **IT-29**(4):551–559, 1983. 35

[73] **CGAL, Computational Geometry Algorithms Library**. http://www.cgal.org. 35

[74] **Gmsh: a three-dimensional finite element mesh generator with built-in pre- and post-processing facilities**. http://www.geuz.org/gmsh/. 35

[75] Dietrich Braess. *Finite Elemente Theorie: schnelle Löser und Anwendungen in der Elastizittstheorie*. Springer Verlag, Berlin, Germany, 4th ed. edition, 2007. 37

[76] Mohammed Ameen. *Computational Elasticity*. Alpha Science Int. Ltd., Harrow, U.K., 2005. 37

[77] Wolfgang Bangerth, Ralf Hartmann, and Guido Kanschat. **deal.II—A general-purpose object-oriented finite element library**. *ACM Transactions on Mathematical Software*, **33**(4), August 2007. 40, 67

[78] Ricardo A. Maronna, R. Douglas Martin, and Víctor J. Yohai. *Robust Statistics - Theory and Methods*. John Wiley & Sons, Ltd, 2006. 41, 48, 50, 51

[79] William H. [Hrsg.] Press, Saul A. [Hrsg.] Teukolsky, William T. [Hrsg.] Vetterling, and Brian P. [Hrsg.] Flannery, editors. *Numerical recipes*. Cambridge Univ. Press, Cambridge [u.a.], 3rd ed. edition, 2007. Includes bibliographical references and index. - This printing is corrected to software version 3.0. 42, 66, 68

[80] D. V. Lukyanenko and A. G. Yagola. **Using Parallel Computing for Solving Multidimensional Ill-posed Problems**. In Y. Wang, A. G. Yagola, and Y. Changchun, editors, *Computational Methods for Applied Inverse Problems*, pages 49–81. De Gruyter, Boston, MA, USA, 2012. 42

[81] H. Delanoë-Ayari, J. Rieu, and M. Sano. **4D Traction Force Microscopy Reveals Asymmetric Cortical Forces in Migrating Dictyostelium Cells**. *Physical Review Letters*, **105**(24):2–5, December 2010. 43

[82] Pirta Hotulainen and Pekka Lappalainen. **Stress fibers are generated by two distinct actin assembly mechanisms in motile cells.** *The Journal of Cell Biology*, **173**(3):383–94, May 2006. 44, 64, 83, 84, 87

[83] Gleb Shtengel. **Interferometric fluorescent super-resolution microscopy resolves 3D cellular ultrastructure**. *Proceedings of the National Academy of Sciences of the United States of America*, **106**(9):3125–3130, 2009. 46

[84] Daniel Aquino, Andreas Schönle, Claudia Geisler, Claas Middendorff, Christian A Wurm, Yosuke Okamura, Thorsten Lang, Stefan W Hell, and Alexander Egner. **Two-color nanoscopy of three-dimensional volumes by 4Pi detection of stochastically switched fluorophores**. *Nature Methods*, **8**(4):353–359, 2011. 46

[85] Ke Xu, Hazen P Babcock, and Xiaowei Zhuang. **Dual-objective STORM reveals three-dimensional filament organization in the actin cytoskeleton.** *Nature Methods*, **9**(2):185–8, February 2012. 46

[86] Michele a Wozniak and Christopher S Chen. **Mechanotransduction in development: a growing role for contractility.** *Nature Reviews. Molecular Cell Biology*, **10**(1):34–43, January 2009. 59

[87] Daniel Riveline, Eli Zamir, Nathalie Q Balaban, Ulrich S Schwarz, Toshimasa Ishizaki, Shuh Narumiya, Zvi Kam, Benjamin Geiger, and Alexander D Bershadsky. **Focal contacts as mechanosensors: externally applied local mechanical force induces growth of focal contacts by an mDia1-dependent and ROCK-independent mechanism.** *The Journal of Cell Biology*, **153**(6):1175–86, June 2001. 59, 81, 82

[88] Alexander Bershadsky, Michael Kozlov, and Benjamin Geiger. **Adhesion-mediated mechanosensitivity: a time to experiment, and a time to theorize.** *Current Opinion in Cell Biology*, **18**(5):472–481, October 2006. 59, 65

[89] Paul a Janmey and R Tyler Miller. **Mechanisms of mechanical signaling in development and disease.** *Journal of Cell Science*, **124**(Pt 1):9–18, January 2011. 59

[90] Jonathan Stricker, Yvonne Aratyn-Schaus, Patrick W Oakes, and Margaret L Gardel. **Spatiotemporal constraints on the force-dependent growth of focal adhesions.** *Biophysical Journal*, **100**(12):2883–93, June 2011. 60, 81, 82, 105

[91] Patrick W. Oakes, Yvonne Beckham, Jonathan Stricker, and Margaret L Gardel. **Tension is required but not sufficient for focal adhesion maturation without a stress fiber template**. *The Journal of Cell Biology*, **196**(3):363–374, January 2012. 60, 79, 105, 108

[92] Carsten Grashoff, Brenton D. Hoffman, Michael D. Brenner, Ruobo Zhou, Maddy Parsons, Michael T. Yang, Mark A. McLean, Stephen G. Sligar, Christopher S Chen, Taekjip Ha, and Martin A. Schwartz. **Measuring mechanical tension across vinculin reveals regulation of focal adhesion dynamics**. *Nature*, **466**(7303):263–266, July 2010. 60

[93] Ilka B Bischofs, Franziska Klein, Dirk Lehnert, Martin Bastmeyer, and Ulrich S Schwarz. **Filamentous network mechanics and active contractility determine cell and tissue shape.** *Biophysical Journal*, **95**(7):3488–96, October 2008. 63, 65, 91, 92

[94] Philip Guthardt Torres, Ilka B Bischofs, and Ulrich S Schwarz. **Contractile network models for adherent cells**. *Physical Review E*, **85**, January 2012. 63, 65, 91

[95] Caroline a Schneider, Wayne S Rasband, and Kevin W Eliceiri. **NIH Image to ImageJ: 25 years of image analysis**. *Nature Methods*, **9**(7):671–675, June 2012. 64

[96] **Visualization Toolkit - opensource software system for 3D computer graphics, image processing and visualization. (Kitware)**. http://www.vtk.org/. 64

[97] Per-Olof Persson and Gilbert Strang. **A simple mesh generator in MATLAB**. *SIAM Review*, **46**(2):329–345, 2004. 65

[98] Magdalena Chrzanowska-Wodnicka and Keith Burridge. **Rho-stimulated contractility drives the formation of stress fibers and focal adhesions.** *The Journal of Cell Biology*, **133**(6):1403–15, June 1996. 65

[99] Ilka Bischofs, Sebastian Schmidt, and Ulrich Schwarz. **Effect of Adhesion Geometry and Rigidity on Cellular Force Distributions**. *Physical Review Letters*, **103**(4), July 2009. 65, 92

[100] Philip Guthard Torres. *Modeling Shape and Rupture of Filament Networks*. Phd thesis, Facultiy for Physics and Astronomy, Heidelberg University, 2012. 66, 91, 108

[101] Achim Besser, Julien Colombelli, Ernst H. K. Stelzer, and Ulrich S. Schwarz. **Viscoelastic response of contractile filament bundles**. *Physical Review E*, **83**(5), May 2011. 67

[102] Tom Shemesh, Alexander B Verkhovsky, Tatyana M Svitkina, Alexander D Bershadsky, and Michael M Kozlov. **Role of focal adhesions and mechanical stresses in the formation and progression of the lamellipodium-lamellum interface [corrected].** *Biophysical Journal*, **97**(5):1254–64, September 2009. 67, 88

[103] Tom Shemesh, Alexander D. Bershadsky, and Michael M. Kozlov. **Physical Model for Self-Organization of Actin Cytoskeleton and Adhesion Complexes at the Cell Front**. *Biophysical Journal*, **102**(8):1746–1756, April 2012. 67, 88

[104] **boost - C++ libraries**. http://www.boost.org/. 68

[105] Aaron Mertz, Shiladitya Banerjee, Yonglu Che, Guy German, Ye Xu, Callen Hyland, M. Marchetti, Valerie Horsley, and Eric Dufresne. **Scaling of Traction Forces with the Size of Cohesive Cell Colonies**. *Physical Review Letters*, **108**(19):1–5, May 2012. 77, 93

[106] Shiladitya Banerjee and Cristina M Marchetti. **Substrate rigidity deforms and polarizes active gels**. *EPL (Europhysics Letters)*, **96**(2):28003, October 2011. 77, 93

[107] Carina Edwards and Ulrich Schwarz. **Force Localization in Contracting Cell Layers**. *Physical Review Letters*, **107**(12):1–5, September 2011. 77, 93, 97, 107

[108] Joseph P Califano and Cynthia A Reinhart-King. **Substrate Stiffness and Cell Area Predict Cellular Traction Stresses in Single Cells and Cells in Contact**. *Cellular and Molecular Bioengineering*, **3**(1):68–75, 2010. 78

[109] Cynthia a Reinhart-King, Micah Dembo, and Daniel a Hammer. **The dynamics and mechanics of endothelial cell spreading.** *Biophysical Journal*, **89**(1):676–89, July 2005. 78, 86

[110] Ning Wang, Emanuele Ostuni, George M Whitesides, and Donald E Ingber. **Micropatterning tractional forces in living cells.** *Cell Motility and the Cytoskeleton*, **52**(2):97–106, July 2002. 78

[111] Shang-You Tee, Jianping Fu, Christopher S Chen, and Paul a Janmey. **Cell shape and substrate rigidity both regulate cell stiffness.** *Biophysical Journal*, **100**(5):L25–7, March 2011. 78, 86

[112] Christopher a Lemmon and Lewis H Romer. **A predictive model of cell traction forces based on cell geometry.** *Biophysical Journal*, **99**(9):L78–80, December 2010. 78

[113] Andrew D Rape, Wei-Hui Guo, and Yu-Li Wang. **The regulation of traction force in relation to cell shape and focal adhesions.** *Biomaterials*, **32**(8):2043–2051, December 2011. 78

[114] Fang Li, Bin Li, Qing-Ming Wang, and James H-C Wang. **Cell shape regulates collagen type I expression in human tendon fibroblasts.** *Cell Motility and the Cytoskeleton*, **65**(4):332–41, May 2008. 78

[115] Cynthia A Reinhart-King, Micah Dembo, and Daniel A Hammer. **Endothelial cell traction forces on RGD-derivatized polyacrylamide substrata**. *Langmuir*, **11**(7):1573–1579, 2003. 78

[116] Christopher S Chen, M. Mrksich, S. Huang, G. M. Whitesides, and Donald E. Ingber. **Geometric Control of Cell Life and Death**. *Science*, **276**(5317):1425–1428, May 1997. 78

[117] Pere Roca-Cusachs, Armando Del Rio, Eileen Puklin-Faucher, Nils C Gauthier, Nicolas Biais, and Michael P Sheetz. **Integrin-dependent force transmission to the extracellular matrix by α-actinin triggers adhesion maturation.** *Proceedings of the National Academy of Sciences of the United States of America*, **110**(15):E1361–70, April 2013. 79

[118] Steven Munevar, Yu-li Wang, and Micah Dembo. **Traction Force Microscopy of Migrating Normal and H-ras Transformed 3T3 Fibroblasts**. *Biophysical Journal*, **80**(4):1744–1757, April 2001. 80

[119] Michele a Wozniak, Katarzyna Modzelewska, Lina Kwong, and Patricia J Keely. **Focal adhesion regulation of cell behavior.** *Biochimica et Biophysica Acta*, **1692**(2-3):103–19, July 2004. 81

[120] Viola Vogel and Michael P Sheetz. **Cell fate regulation by coupling mechanical cycles to biochemical signaling pathways.** *Current Opinion in Cell Biology*, **21**(1):38–46, February 2009. 81

[121] Catherine G Galbraith, Kenneth M Yamada, and Michael P Sheetz. **The relationship between force and focal complex development.** *The Journal of Cell Biology*, **159**(4):695–705, November 2002. 82

[122] Tea Vallenius. **Actin stress fibre subtypes in**. *Open Biology*, **3**, 2013. 83

[123] Sari Tojkander, Gergana Gateva, and Pekka Lappalainen. **Actin stress fibers–assembly, dynamics and biological roles.** *Journal of Cell Science*, **125**(Pt 8):1855–64, April 2012. 83

[124] Perttu Naumanen, Pekka Lappalainen, and Pirta Hotulainen. **Mechanisms of actin stress fibre assembly.** *Journal of Microscopy*, **231**(3):446–54, September 2008. 83, 87

[125] Bianca Kovac, Jessica L Teo, Tomi P Mäkelä, and Tea Vallenius. **Assembly of non-contractile dorsal stress fibers requires α-actinin-1 and Rac1 in migrating and spreading cells.** *Journal of Cell Science*, **126**(Pt 1):263–73, January 2013. 83

[126] Dylan T Burnette, Suliana Manley, Prabuddha Sengupta, Rachid Sougrat, Michael W Davidson, Bechara Kachar, and Jennifer Lippincott-Schwartz. **A role for actin arcs in the leading-edge advance of migrating cells.** *Nature Cell Biology*, **13**(4):371–81, April 2011. 83, 87

[127] Magnus Edlund, Marc A Lotano, and Carol A Otey. **Dynamics of alpha-actinin in focal adhesions and stress fibers visualized with alpha-actinin-green fluorescent protein.** *Cell Motility and the Cytoskeleton*, **48**(3):190–200, March 2001. 83, 87

[128] Nicole Endlich, Carol a Otey, Wilhelm Kriz, and Karlhans Endlich. **Movement of stress fibers away from focal adhesions identifies focal adhesions as sites of stress fiber assembly in stationary cells.** *Cell Motility and the Cytoskeleton*, **64**(12):966–76, December 2007. 87

[129] Lynda J Peterson, Zenon Rajfur, Amy S Maddox, Christopher D Freel, Yun Chen, Magnus Edlund, Carol Otey, and Keith Burridge. **Simultaneous Stretching and Contraction of Stress Fibers In Vivo**. *Molecular Biology of the Cell*, **15**:3497–3508, 2004. 87

[130] Yu-li Wang. **Flux at Focal Adhesions: Slippae Clutch, Mechanical Gauge, or Signal Depot**. *Science*, page pe10, 2007. 88

[131] Ke Hu, Lin Ji, Kathryn T Applegate, Gaudenz Danuser, and Clare M Waterman-Storer. **Differential transmission of actin motion within focal adhesions.** *Science*, **315**(5808):111–5, January 2007. 88

[132] Colin K Choi, Miguel Vicente-Manzanares, Jessica Zareno, Leanna a Whitmore, Alex Mogilner, and Alan Rick Horwitz. **Actin and alpha-actinin orchestrate the assembly and maturation of nascent adhesions in a myosin II motor-independent manner.** *Nature Cell Biology*, **10**(9):1039–50, September 2008. 88

[133] Matthew J Paszek and Valerie M Weaver. **The Tension Mounts: Mechanics Meets Morphogenesis and Malignancy**. *Journal of Mammary Gland Biology and Neoplasia*, **9**(4):325–342, 2004. 89

[134] Matthew J Paszek, Nastaran Zahir, Kandice R Johnson, Johnathon N Lakins, Gabriela I Rozenberg, Amit Gefen, Cynthia a Reinhart-King, Susan S Margulies, Micah Dembo, David Boettiger, Daniel a Hammer, and Valerie M Weaver. **Tensional homeostasis and the malignant phenotype.** *Cancer Cell*, **8**(3):241–54, September 2005. 89

[135] R Kristal-Muscal, Liron Dvir, and Daphne Weihs. **Metastatic cancer cells tenaciously indent impenetrable, soft substrates**. *New Journal of Physics*, **15**(3):035022, March 2013. 89, 99, 100, 107

[136] Paul Martin. **Wound Healing–Aiming for Perfect Skin Regeneration**. *Science*, **276**(5309):75–81, April 1997. 89

[137] Chun-Chi Liang, Ann Y Park, and Jun-Lin Guan. **In vitro scratch assay: a convenient and inexpensive method for analysis of cell migration in vitro.** *Nature Protocols*, **2**(2):329–33, January 2007. 89

[138] Albert Folch, Byung-Ho Jo, Octavio Hurtado, David J Beebe, and Mehmet Toner. **Microfabricated elastomeric stencils for micropatterning cell cultures.** *Journal of Biomedical Materials Research*, **52**(2):346–53, November 2000. 89

[139] Mathieu Poujade, Erwan Grasland-Mongrain, A Hertzog, J Jouanneau, P Chavrier, B Ladoux, A Buguin, and Pascal Silberzan. **Collective migration of an epithelial monolayer**. *Proceedings of the National Academy of Sciences of the United States of America*, **104**:15988–93, 2007. 90

[140] Olivier Cochet-Escartin, Jonas Ranft, Pascal Silberzan, and Philippe Marcq. **Border forces and friction control epithelial closure dynamics.** *Biophysical Journal*, **106**(1):65–73, January 2014. 90

[141] Xavier Trepat, Guillaume Lenormand, and Jeffrey J. Fredberg. **Universality in cell mechanics**. *Soft Matter*, **4**(9):1750, 2008. 90

[142] E. Anon, X. Serra-Picamal, P. Hersen, N. C. Gauthier, M. P. Sheetz, X. Trepat, and B. Ladoux. **Cell crawling mediates collective cell migration to close undamaged epithelial gaps**. *Proceedings of the National Academy of Sciences of the United States of America*, **109**(27), June 2012. 90, 94

[143] Dhananjay T Tambe, C Corey Hardin, Thomas E Angelini, Kavitha Rajendran, Chan Young Park, Xavier Serra-Picamal, Enhua H Zhou, Muhammad H Zaman, James P Butler, David a Weitz, Jeffrey J Fredberg, and Xavier Trepat. **Collective cell guidance by cooperative intercellular forces.** *Nature Materials*, **10**(6):469–75, June 2011. 90

[144] Xavier Serra-Picamal, Vito Conte, Romaric Vincent, Ester Anon, Dhananjay T. Tambe, Elsa Bazellieres, James P. Butler, Jeffrey J. Fredberg, and Xavier Trepat. **Mechanical waves during tissue expansion**. *Nature Physics*, **8**(7), July 2012. 90

[145] Michael H. Köpf and Len M. Pismen. **A continuum model of epithelial spreading**. *Soft Matter*, **9**(14):3727, 2013. 90

[146] D Stamenović and M F Coughlin. **A quantitative model of cellular elasticity based on tensegrity.** *Journal of Biomechanical Engineering*, **122**(1):39–43, February 2000. 91

[147] Mark F Coughlin and Dimitrije Stamenović. **A prestressed cable network model of the adherent cell cytoskeleton.** *Biophysical Journal*, **84**(2 Pt 1):1328–36, February 2003. 91

[148] Raja Paul, Patrick Heil, Joachim P Spatz, and Ulrich S Schwarz. **Propagation of mechanical stress through the actin cytoskeleton toward focal adhesions: model and experiment.** *Biophysical Journal*, **94**(4):1470–82, February 2008. 91

[149] Vikram S Deshpande, Robert M McMeeking, and Anthony G Evans. **A bio-chemo-mechanical model for cell contractility.** *Proceedings of the National Academy of Sciences of the United States of America*, **103**(38):14015–20, September 2006. 91, 108

[150] Vikram S. Deshpande, Robert M. McMeeking, and Anthony G. Evans. **A model for the contractility of the cytoskeleton including the effects of stress-fibre formation and dissociation**. *Proceedings of the Royal Society A: Mathematical, Physical and Engineering Sciences*, **463**(2079):787–815, March 2007. 91

[151] WR Legant, Amit Pathak, and MT Yang. **Microfabricated tissue gauges to measure and manipulate forces from 3D microtissues**. *Proceedings of the National Academy of Sciences of the United States of America*, **106**(25):10097–102, June 2009. 91

[152] Amit Pathak, Vikram S Deshpande, Robert M McMeeking, and Anthony G Evans. **The simulation of stress fibre and focal adhesion development in cells on patterned substrates.** *Journal of the Royal Society, Interface / the Royal Society*, **5**(22):507–24, May 2008. 91

[153] William Ronan, Vikram S Deshpande, Robert M McMeeking, and J Patrick McGarry. **Numerical investigation of the active role of the actin cytoskeleton in the compression resistance of cells.** *Journal of the Mechanical Behavior of Biomedical Materials*, **14**:143–57, October 2012. 91

[154] Franck J Vernerey and Mehdi Farsad. **A constrained mixture approach to mechano-sensing and force generation in contractile cells.** *Journal of the Mechanical Behavior of Biomedical Materials*, **4**(8):1683–99, November 2011. 92

[155] Franck J Vernerey and Mehdi Farsad. **An Eulerian/XFEM formulation for the large deformation of cortical cell membrane.** *Computer Methods in Biomechanics and Biomedical Engineering*, **14**(5):433–45, May 2011. 92

[156] Mehdi Farsad and FJ Vernerey. **An XFEM-based numerical strategy to model mechanical interactions between biological cells and a deformable substrate**. *International Journal for Numerical Methods in Engineering*, (June):238–267, 2012. 92, 108

[157] Olivia du Roure, Alexandre Saez, Axel Buguin, Robert H Austin, Philippe Chavrier, Pascal Silberzan, Pascal Siberzan, and Benoit Ladoux. **Force mapping in epithelial cell migration.** *Proceedings of the National Academy of Sciences of the United States of America*, **102**(7):2390–5, February 2005. 92

[158] Roy Bar-Ziv, Tsvi Tlusty, Elisha Moses, Samuel Safran, and Alexander Bershadsky. **Pearling in cells: a clue to understanding cell shape.** *Proceedings of the National Academy of Sciences of the United States of America*, **96**(18):10140–5, August 1999. 92

[159] Shiladitya Banerjee and Luca Giomi. **Polymorphism and bistability in adherent cells**. *Soft Matter*, **9**(21):5251, 2013. 92

[160] Jérôme RD Soiné. *Dynamics of cell shape on micropatterned substrates.* Diploma thesis, Facultiy of Chemistry and Biosciences, Karlsruhe Institute of Technology, 2010. 92

[161] Celeste M Nelson, Ronald P Jean, John L Tan, Wendy F Liu, Nathan J Sniadecki, Alexander a Spector, and Christopher S Chen. **Emergent patterns of growth controlled by multicellular form and mechanics.** *Proceedings of the National Academy of Sciences of the United States of America*, **102**(33):11594–9, August 2005. 93

[162] Shiladitya Banerjee and Cristina M Marchetti. **Contractile Stresses in Cohesive Cell Layers on Finite-Thickness Substrates**. *Physical Review Letters*, **109**(10):108101, September 2012. 93

[163] Aaron Mertz, Yonglu Che, Shiladitya Banerjee, Jill M Goldstein, Kathryn Rosowski, Stephen Revilla, Carien Niessen, Christina M Marchetti, Eric R Dufresne, and Valerie Horsley. **Cadherin-based intercellular adhesions organize epithelial cellmatrix traction forces**. *Proceedings of the National Academy of Sciences of the United States of America*, **110**(3):842–847, 2013. 93

[164] Sebastian Rausch, Tamal Das, Jérôme Rd Soiné, Tobias W Hofmann, Christian Hj Boehm, Ulrich S Schwarz, Heike Boehm, and Joachim P Spatz. **Polarizing cytoskeletal tension to induce leader cell formation during collective cell migration**. *Biointerphases*, **8**(1):32, 2013. 94, 95, 107

[165] Yvonne Aratyn-Schaus, Patrick W Oakes, Jonathan Stricker, Stephen P Winter, and Margaret L Gardel. **Preparation of complaint matrices for quantifying cellular contraction.** *Journal of Visualized Experiments : JoVE*, (46):1–6, January 2010. 94

[166] Andrew R Harris and G T Charras. **Experimental validation of atomic force microscopy-based cell elasticity measurements.** *Nanotechnology*, **22**(34):345102, August 2011. 98

[167] Naama Gal and Daphne Weihs. **Intracellular mechanics and activity of breast cancer cells correlate with metastatic potential.** *Cell Biochemistry and Biophysics*, **63**(3):199–209, July 2012. 99, 103

[168] Jochen Guck, Stefan Schinkinger, Bryan Lincoln, Falk Wottawah, Susanne Ebert, Maren Romeyke, Dominik Lenz, Harold M Erickson, Revathi Ananthakrishnan, Daniel Mitchell, Josef Käs, Sydney Ulvick, and Curt Bilby. **Optical deformability as an inherent cell marker for testing malignant transformation and metastatic competence.** *Biophysical Journal*, **88**(5):3689–98, May 2005. 103

[169] Sarah E Cross, Yu-Sheng Jin, Jianyu Rao, and James K Gimzewski. **Nanomechanical analysis of cells from cancer patients.** *Nature Nanotechnology*, **2**(12):780–3, December 2007. 103

[170] Julien Colombelli, Achim Besser, Holger Kress, Emmanuel G Reynaud, Philippe Girard, Emmanuel Caussinus, Uta Haselmann, John V Small, Ulrich S Schwarz, and Ernst H K Stelzer. **Mechanosensing in actin stress fibers revealed by a close correlation between force and protein localization.** *Journal of Cell Science*, **122**:1665–79, May 2009. 105

[171] Nicole Endlich and Karlhans Endlich. % bf The Change and Response of Podocytes to Glomerular Hypertension. *Seminars in Nephroloy*, **32**(4):327–341, 2012. 108

[172] Cécile M Bidan, Krishna P Kommareddy, Monika Rumpler, Philip Kollmannsberger, Yves J M Bréchet, Peter Fratzl, and John W C Dunlop. **How linear tension converts to curvature: geometric control of bone tissue growth.** *PloS One*, **7**(5):e36336, January 2012. 108

Acknowledgements

First of all I want to thank Prof. Dr. Ulrich Schwarz for supervising my thesis and for the opportunity to work in his group. I am thankful for having learned a lot about biophysics from him and for the possibility to participate in many interesting conferences.

My special gratitude goes to numerous collaboration partners. Their experimental expertise and creativity were cornerstones for this thesis. Therefore, I want to thank Georg Dreissen, Nils Hersch, Nico Hampe from Jülich, the Endlich group from Greifswald, the Gardel group from Chicago, and Sebastian Rausch and Dr. Heike Böhm from Heidelberg.

I would also like to thank Prof. Dr. Horner for kindly reviewing this thesis.

I further want to thank all members of the Schwarz group for a harmonic and humorous group atmosphere. In particular, I want to thank Christoph Brand for working with me and for proofreading. I also would like to thank Max Hoffman for sharing the office with me.

My special thanks go to my girl friend Annina Eberhardt, for here love and support. I also want to thank her parents Birgitt and Axel Eberhardt. Finally I am deeply grateful to my parents Marianne and Jérôme Soiné, my grand parents Renate and Heinz Geiger, and my uncle Richard Soiné, for funded my studies and supporting me.